

May 2019

Optimizing Advanced Ligo's Scientific Output with Fast, Accurate, Clean Calibration

Aaron Daniel Viets

University of Wisconsin-Milwaukee

Follow this and additional works at: <https://dc.uwm.edu/etd>



Part of the [Physics Commons](#)

Recommended Citation

Viets, Aaron Daniel, "Optimizing Advanced Ligo's Scientific Output with Fast, Accurate, Clean Calibration" (2019). *Theses and Dissertations*. 2135.

<https://dc.uwm.edu/etd/2135>

This Dissertation is brought to you for free and open access by UWM Digital Commons. It has been accepted for inclusion in Theses and Dissertations by an authorized administrator of UWM Digital Commons. For more information, please contact open-access@uwm.edu.

OPTIMIZING ADVANCED LIGO'S SCIENTIFIC OUTPUT
WITH FAST, ACCURATE, CLEAN CALIBRATION

by

Aaron D. Viets

A DISSERTATION SUBMITTED IN
PARTIAL FULFILLMENT OF THE
REQUIREMENTS FOR THE DEGREE OF

DOCTOR OF PHILOSOPHY
IN PHYSICS

at

The University of Wisconsin–Milwaukee

May 2019

ABSTRACT

OPTIMIZING ADVANCED LIGO'S SCIENTIFIC OUTPUT WITH FAST,
ACCURATE, CLEAN CALIBRATION

by
Aaron D. Viets

The University of Wisconsin–Milwaukee, May 2019
Under the Supervision of Professor Jolien Creighton

Since 2015, the direct observation of gravitational waves has opened a new window to observe the universe and made strong-field tests of Einstein's general theory of relativity possible for the first time. During the first two observing runs of the Advanced gravitational-wave detector network, the Laser Interferometer Gravitational-wave Observatory (LIGO) and the Virgo detector have made 10 detections of binary black hole mergers and one detection of a binary neutron star merger with a coincident gamma-ray burst [1]. This dissertation discusses methods used in low and high latency to produce Advanced LIGO's calibrated strain data, highlighting improvements to accuracy, latency, and noise reduction that have been made since the beginning of the second observing run (O2). Systematic errors in the calibration during O2 varied by frequency, but were generally no greater than 5% in amplitude and 3° in phase from 20 Hz to 1 kHz [2]. Due in part to this work, it is now possible to achieve calibration accuracy at the level of ~1% in amplitude and ~1° in phase, offering improvements to downstream astrophysical analyses. Since the beginning of O2, latency intrinsic to the calibration procedure has decreased from ~12 s to ~3 s. As latency in data distribution and the sending of automated alerts to astronomers is minimized, reduction in calibration latency will become important for follow-up of events like the binary neutron star merger GW170817. A method of removing spectral lines and broadband noise in the calibration procedure has been developed since O2, offering increases in total detectable volume during future observing runs. High-latency subtraction of lines and broadband noise had a large impact on astrophysical analyses during O2 [3]. A similar data product can now be made available in low latency for the first time.

I dedicate this dissertation to my dear wife, Mary.

TABLE OF CONTENTS

1	Introduction	1
1.1	Newtonian gravity	1
1.2	Special relativity and Einstein's problem with Newton's gravity	2
1.3	A brief description of general relativity	7
1.3.1	Differential geometry	8
1.3.2	The Einstein field equations	11
1.3.3	Linearized gravity and the wave solution	12
1.3.4	The transverse traceless gauge	14
1.4	The Advanced LIGO detectors	16
1.4.1	DARM response to gravitational waves	18
1.4.2	The detectors' optical response to DARM motion	21
1.4.3	Sensitivity of the detectors to DARM motion	26
2	Advanced LIGO calibration overview	29
2.1	Black box models of the detector's response to gravitational waves	30
2.2	Time-domain calibration	32
2.3	Sensing function	33
2.4	Actuation function	34
2.5	Measurements	35
2.6	Temporal variations in the response of the detectors	37
2.7	Calibration pipelines	37
3	The <code>gstlal</code> calibration pipeline	40
3.1	Use of <code>GStreamer</code> and <code>gstlal</code> in calibration	40
3.2	Operation procedures in the <code>gstlal</code> calibration pipeline	41
3.2.1	Filling in missing raw data	41
3.2.2	Computing the time-dependent correction factors	42

3.2.3	Applying FIR filters to compute $h(t)$	43
3.2.4	The calibration state vector	43
3.3	The low-latency <code>gstlal</code> calibration pipeline	45
3.4	The high-latency <code>gstlal</code> calibration pipeline	47
4	Designing digital filters for calibration	49
4.1	Principles of making FIR filters	49
4.1.1	The ideal low- and high-pass filters	49
4.1.2	Applying time-domain window functions to filters	50
4.1.3	Resampling of time-series data	51
4.2	Designing FIR filters to model the inverse sensing and actuation functions	52
4.2.1	Attenuating low-frequency noise with minimal latency	54
4.2.2	Accuracy of the filters' representation of the response function . .	58
5	Temporal variations in calibration-model parameters	60
5.1	Calibration lines	61
5.2	Computing time-dependent correction factors	63
5.2.1	Measuring the calibration lines	63
5.2.2	Computing the time-dependence of the actuation function	65
5.2.3	Computing the optical gain and coupled cavity pole frequency . .	66
5.2.4	Computing the detuning of the signal recycling cavity	67
5.2.5	Drawbacks of approximations in the calculation of the TDCFs . .	69
5.2.6	Computing the TDCFs using an exact solution	70
5.2.7	Attenuating noise in the computed TDCFs	78
5.3	Compensating for time dependence in the calibration models	80
5.3.1	Applying scalar corrections to the components of ΔL_{free}	80
5.3.2	Compensating for frequency-dependent temporal variations	81
5.3.3	Impact of compensating for time dependence on calibration accuracy	84

6	Subtraction of excess noise from the calibrated signal	87
6.1	Subtraction of calibration lines	89
6.2	Subtraction of additional spectral lines	92
6.3	Subtraction of broadband noise in the <code>gstlal</code> calibration pipeline	95
6.3.1	Computing transfer functions	96
6.3.2	Producing and updating FIR filters for witness channels	97
6.3.3	Low-latency and high-latency noise subtraction	99
6.3.4	Stability over time	101
6.3.5	Impact on calibration accuracy and uncertainty	102
6.3.6	Impact on calibration latency	104
7	Impact of calibration accuracy and noise subtraction on astrophysical analyses	105
7.1	Methods of the study	105
7.2	Time dependence and parameter estimation	106
7.2.1	GW170814	106
7.2.2	GW170817	108
7.3	Noise subtraction and parameter estimation	113
8	Conclusion	115
	Bibliography	118
	Curriculum Vitae	121

LIST OF FIGURES

1	Thought experiment for time dilation and length contraction	3
2	The effect of gravitational waves on a ring of free particles	15
3	Diagram of an Advanced LIGO detector	17
4	Antenna pattern of an Advanced LIGO detector	20
5	Advanced LIGO's DARM feedback control loop	30
6	Bode plot of the sensing function model	33
7	Bode plot of the actuation function model	35
8	Block diagram of the low-latency <code>gstlal</code> calibration pipeline	46
9	Block diagram of the high-latency <code>gstlal</code> calibration pipeline	47
10	Comparison of window functions used in calibration filters	54
11	Time series of calibration latencies	55
12	Additional high-pass filter in the inverse sensing path	56
13	Amplitude spectral densities showing improvements in high-pass filtering	57
14	Response function of the calibration filters	58
15	Detuning of the signal recycling cavity	68
16	Time series of the ratio $\widetilde{\Delta L}_{\text{free}}(f)/\tilde{x}_{\text{pc}}(f)$ at the Pcal line frequencies . . .	84
17	Transfer function $\widetilde{\Delta L}_{\text{free}}(f)/\tilde{x}_{\text{pc}}(f)$ during a Pcal broadband injection . .	85
18	Amplitude spectral density with noise subtraction	88
19	Binary neutron star inspiral range with noise subtraction	88
20	Calibration line subtraction stability over time	91
21	Temporal drifts in the power mains frequency	94
22	Power mains line subtraction stability over time	95
23	Block diagram of noise subtraction in the <code>gstlal</code> calibration pipeline . .	98
24	Transfer function between uncleaned strain data and cleaned strain data	101
25	Time series of $\widetilde{\Delta L}(f)/\tilde{x}_{\text{pc}}(f)$ at Pcal lines for $h(t)$ with noise subtraction	102
26	Time series of calibration latency with and without noise subtraction . .	103

27	Skymaps for GW170814 with varying calibration accuracy	107
28	Calibration accuracy and luminosity distance for GW170814	108
29	Calibration accuracy and chirp mass for GW170814	109
30	Calibration accuracy and symmetric mass ratio for GW170814	109
31	Probability distributions of m_1 and m_2 for GW170814	110
32	Calibration accuracy and luminosity distance for GW170817	111
33	Calibration accuracy and chirp mass for GW170817	111
34	Calibration accuracy and symmetric mass ratio for GW170817	112
35	Probability distributions of m_1 and m_2 for GW170817	113
36	Skymaps for GW170814 with and without noise subtraction	114

LIST OF TABLES

1	Calibration state vector bits	44
2	O3 calibration lines	63
3	Calibration time dependence simulation	69
4	Calibration accuracy and parameter estimation for GW170814	110
5	Calibration accuracy and parameter estimation for GW170817	113

CONVENTIONS

- Greek letters ($\alpha, \beta, \gamma, \dots$) indicate spacetime indices 0, 1, 2, 3, and Latin letters (a, b, c, \dots) indicate spatial indices 1, 2, 3.
- In the context of differential geometry (i.e., in Chapter 1), the Einstein summation convention is used, where there is an implied sum over repeated indices. For example, $\eta_{\mu\nu} dx^\mu dx^\nu = \sum_{\mu=0}^3 \sum_{\nu=0}^3 \eta_{\mu\nu} dx^\mu dx^\nu$.
- Fourier transforms are indicated using tildes above functions, e.g. $\tilde{A}(f)$.
- The Fourier transform and inverse Fourier transform conventions used are

$$\begin{aligned}\tilde{x}(f) &= \int_{-\infty}^{\infty} x(t) e^{-2\pi i f t} dt \\ x(t) &= \int_{-\infty}^{\infty} \tilde{x}(f) e^{2\pi i f t} df .\end{aligned}$$

- Variables in bold font indicate vectors or matrices, such as \mathbf{M} .

ACRONYMS

BS	Beamsplitter
CARM	Common Arm
DARM	Differential Arm
DC	Direct Current
DCS	Data and Computing Systems
DMT	Data Monitoring Tool
ETMX	End Test Mass X
ETMY	End Test Mass Y
FIR	Finite Impulse Response
GDS	Global Diagnostic System
GLib	GNU Library
GNU	GNU's Not UNIX!
GstLAL	GStreamer LIGO Algorithm Library
GW	Gravitational Wave
H1	LIGO detector at Hanford, WA
IIR	Infinite Impulse Response
ITM	Input Test Mass
ITMX	Input Test Mass X
ITMY	Input Test Mass Y
L1	LIGO detector at Livingston, LA
LAL	LIGO Algorithm Library
Laser	Light Amplification by Stimulated Emission of Radiation
LIGO	Laser Interferometer Gravitational-wave Observatory
O1	First Observing Run
O2	Second Observing Run
O3	Third Observing Run

P	Penultimate
Pcal	Photon calibrator
PD	Photo Detector
PRM	Power Recycling Mirror
SI	International System of Units
SNR	Signal-to-Noise Ratio
SRC	Signal Recycling Cavity
SRM	Signal Recycling Mirror
T	Test
TDCFs	Time-dependent Correction Factors
TT	Transverse Traceless
U	Upper Intermediate

ACKNOWLEDGMENTS

Through my years in graduate school, many friends and family members have provided help and support in numerous ways, and it would not have been possible to complete this work without the help of others. First, I would like to thank my dear wife, Mary. She has provided me with the support and encouragement I need in many ways, and she has been there for me through all my many challenges. Mary has been my source of motivation through all the hard work of the last several years. I would also like to express my gratitude for the gift of our newborn son, David, who has brought so much joy into my life. I am grateful to my parents, Alan and Amy Viets, for supporting and encouraging me throughout my life, and for fostering my fascination with science from a young age. I would like to thank my sister Mary and my brother Toby for their constant support, encouragement, and friendship.

I have received the gift of an excellent advisor, Jolien Creighton, who has patiently directed me and helped me to become a creative research scientist. I would like to thank him for his constant support and his willingness to help me with problems on a moment's notice. I would also like to thank Xavi Siemens for helping to provide me with excellent research opportunities in LIGO calibration, and for many useful discussions.

I am especially grateful for my research collaborator and friend Maddie Wade, who has helped to train me as an expert in LIGO calibration and has always been able to offer useful advice about graduate school, teaching, and research.

I would like to thank my fellow graduate students at UWM, especially Casey McGrath, Adil Amin, and Deep Chatterjee, for making graduate school more enjoyable. I would like to thank Xiaoshu Liu for working with me on a collaborative project, and for his important contribution to this work. I would like to thank Caitlin Rose for her many helpful contributions to the testing of calibration software.

I am blessed to have many wonderful colleagues and research collaborators to work with, especially Alex Urban, who has worked closely with me on numerous occasions and always offered helpful advice and assistance. I would also like to thank Patrick Brockill, Jeff Kissel, Joe Betzwieser, Shivaraj Kandhasamy, Evan Goetz, Alan Weinstein, Rick

Savage, Sudarshan Karki, Darkhan Tuyenbayev, Les Wade, John Zweizig, Kipp Cannon, Chad Hanna, Paul Strycker, and Andrew Ashenden for many useful discussions and contributions.

I would like to thank my dissertation committee, Jolien Crieghton, Xavi Siemens, Patrick Brady, Alan Wiseman, and Maddie Wade, for their thoughtful insights and encouragement, and for helping me to develop as a physicist and a researcher.

The work discussed in this dissertation was supported by National Science Foundation grants PHY-1607585, PHY-1506360, and PHY-1841480.

Chapter 1

Introduction

1.1 Newtonian gravity

Models describing the behavior of gravity have existed since ancient times. Aristotle believed that all terrestrial matter sought to be in what he called its “natural place.” The heavier elements earth and water found their natural place at the center of the universe, causing the Earth to form a sphere with a concentric shell of water surrounding it. Celestial bodies, he believed, were embedded in concentric crystal spheres rotating eternally at fixed rates and made of a weightless substance called “aether.” Centuries later, after the formulation of Copernicus’ heliocentric model of the solar system and Kepler’s laws of planetary motion, Sir Isaac Newton had the profound insight that the motions of terrestrial and celestial bodies were influenced by the very same gravitational force. Newton’s universal law of gravitation was induced empirically to model planetary motion, and is described in his *Principia* [4] as an attractive force between two bodies with a magnitude that is directly proportional to the product of their masses and inversely proportional to the distance between their centers. In mathematical form,

$$F = G \frac{m_1 m_2}{r^2}, \quad (1.1.1)$$

where m_1 and m_2 are the masses of the bodies, r is the distance between their centers, and $G = 6.67 \times 10^{-11} \text{ m}^3/(\text{kg} \cdot \text{s}^2)$ is the gravitational constant. This was not only the first mathematical description of gravity, it also for the first time provided a unified

description of celestial and terrestrial motion, previously viewed as two distinct types of motion. Newton's theory of gravity provides very accurate predictions in the limit of small masses and large separation distances but implies the notion of instantaneous *action at a distance*, which made Newton himself uncomfortable.

1.2 Special relativity and Einstein's problem with Newton's gravity

In 1905, Albert Einstein published his theory of special relativity [5], which would again drastically change the way we think about gravity. Interestingly, Einstein's development of special relativity was motivated by the mathematical descriptions of electric and magnetic fields in Maxwell's equations. Special relativity is summarized by just two postulates:

1. The laws of physics are the same in every inertial frame of reference.
2. The speed of light in a vacuum is the same for all observers (as measured relative to themselves), regardless of both the motion of the observer and the motion of the light source.

The first of these postulates is called the *principle of relativity*. These simple postulates have profound consequences for the way we think about space and time. To see this, consider an experiment done in a spaceship traveling at speed v in the x -direction. Inside the ship, a laser pulse is sent through a beamsplitter down two perpendicular paths of equal length L , as measured inside the spaceship (see Fig. 1). One path is parallel to the motion of the ship, and the other is perpendicular. The beamsplitter records the time from when the light pulse enters the arms (the first *event*) to when it exits (the second event). In the reference frame of the spaceship, this round trip takes a time $\Delta t = 2L/c$, where $c = 299792458$ m/s is the speed of light in a vacuum. Let us now consider the trip inside the vertical arm from an external reference frame, in which the spaceship moves horizontally with speed v . A nonrelativistic approach might lead us to believe

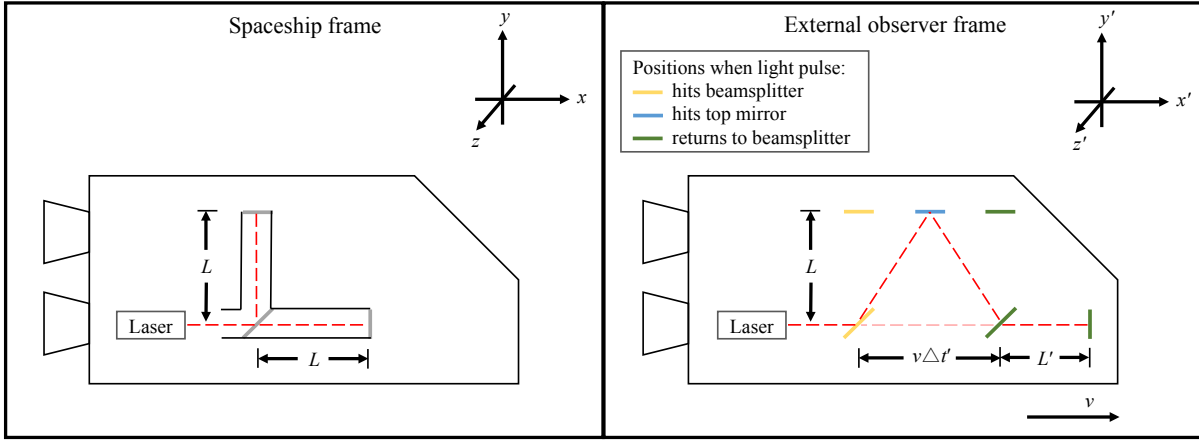


Figure 1 : A spaceship traveling with speed v in the x -direction, as viewed in the reference frame of the ship (t, x, y, z) and from an external reference frame (t', x', y', z') . Inside the ship, a laser sends pulses of light through a beamsplitter into two perpendicular arms with mirrors at the ends. The time of flight is measured at the beamsplitter.

that the velocity of the light and the velocity of ship add to produce a total pulse speed of $\sqrt{c^2 + v^2}$. However, this is inconsistent with special relativity, which holds that the speed of light as measured from the external reference frame must remain equal to c . This seeming paradox is resolved by allowing the spacial and temporal separation of two events to be dependent on one's reference frame. Let us therefore find the time of flight $\Delta t'$ as measured from the external reference frame, assuming a pulse speed c , by solving

$$\Delta t' = \frac{2\sqrt{L^2 + (v\Delta t'/2)^2}}{c}. \quad (1.2.1)$$

We find that the times between the two events as measured in the two reference frames are related by

$$\Delta t' = \gamma \Delta t, \quad (1.2.2)$$

where the Lorentz factor γ is

$$\gamma = \frac{1}{\sqrt{1 - v^2/c^2}}. \quad (1.2.3)$$

This result, called time dilation, means that, as viewed from the external reference frame, clocks inside the ship are running more slowly than stationary clocks. The time recorded in the ship is called the *proper time* τ , distinguished by the fact that the two events occur at the same location in space. It is important to note that this does not imply that time in the ship is "slower" than time in the external reference frame. From the ship's reference

frame, clocks in the external reference frame, moving in the negative x -direction at speed v , also appear to be running at a slower rate than the “stationary” clocks inside the ship. Since the two events occur in the same location in the ship’s frame ($\Delta x = 0$), the spacial separation of the events in the external reference frame depends only on the ship’s speed v and the time $\Delta t'$:

$$\Delta x' = v\Delta t' = \gamma v\Delta t. \quad (1.2.4)$$

We have just considered a special case of a transformation between two reference frames where the two events considered were not spacially separated in one of the frames. In order to generalize this, let us first consider the trip inside the horizontal arm from the external reference frame. Since the light recombines at the same location and the same time in the ship’s reference frame, the same is true in the external reference frame. We therefore know that the time of flight is $\Delta t'$ in the external reference frame, and the speed is still c . From the external reference frame, the light appears to be moving at a speed $c - v$ relative to the arm on the way to the mirror, and at a speed $c + v$ on the way back. We therefore argue that

$$\Delta t' = \frac{L'}{c - v} + \frac{L'}{c + v} \quad (1.2.5)$$

Again, our nonrelativistic intuition that the length of the arm is independent of reference frame will fail us. The only way for the speed of light to be independent of reference frame is to allow the length of the arm to depend on reference frame. The solution for L' in terms of L is

$$L' = L/\gamma. \quad (1.2.6)$$

This effect is called length contraction. The length as measured in the ship, where the object being measured is stationary, is called the *proper length* L_0 . Now we are ready to find how spacial separations between events in the ship’s frame transform into the external reference frame. Let us consider two events on the horizontal arm that, in the ship’s frame, occur at the same time but in different locations. In the ship’s frame, imagine that the beamsplitter at $x = 0$ and the mirror at $x = L$ simultaneously collide with particles moving at speed v in the negative x -direction (i.e., they are at rest in

the external reference frame). Note that the separation between the particles must be contracted in the ship's frame relative to their separation in the external frame. In the external frame, the separation between the particles is γL , while the separation between the beamsplitter and the mirror is L/γ . This means that, in the external reference frame, the two events (the collisions) are not simultaneous! Instead, the collision with the mirror occurs later, and the temporal separation between the events is

$$\Delta t' = \frac{\gamma L - L/\gamma}{v} = \gamma \frac{v \Delta x}{c^2}, \quad (1.2.7)$$

where $\Delta x = L$ is the spacial separation of the events in the ship's frame. The spacial separation between these events in the external reference frame, due to the aforementioned length contraction, is

$$\Delta x' = \gamma L = \gamma \Delta x. \quad (1.2.8)$$

A general coordinate transformation from a reference frame with coordinates (t, x, y, z) to one with coordinates (t', x', y', z') moving in the x -direction with speed v relative to the first reference frame can be found by combining Eq. 1.2.2 with Eq. 1.2.7 and Eq. 1.2.4 with Eq. 1.2.8. The result is a set of transformations known as the Lorentz transformations, given in differential form by

$$dt' = \gamma \left(dt - \frac{v dx}{c^2} \right) \quad (1.2.9a)$$

$$dx' = \gamma (dx - v dt) \quad (1.2.9b)$$

$$dy' = dy \quad (1.2.9c)$$

$$dz' = dz \quad (1.2.9d)$$

The “mixing” of spacial and temporal coordinates implies that distances between points in space and time intervals cannot be considered separately, as they depend on one's frame of reference. Instead, as previously implied, we must consider events, i.e., locations in *spacetime* specified by both a time and a location in space. Similar to the notion that the distance between two points in a 3-dimensional space $(\Delta s)^2 = (\Delta x)^2 + (\Delta y)^2 + (\Delta z)^2$ is the same regardless of the orientation of the coordinate system used, we define an

invariant interval between two events in spacetime that has no dependence on one's choice of coordinates:

$$(\Delta s)^2 = -c^2(\Delta t)^2 + (\Delta x)^2 + (\Delta y)^2 + (\Delta z)^2 . \quad (1.2.10)$$

This can be demonstrated by again considering the path of the light pulse in the vertical direction in the spaceship experiment. In both reference frames, the invariant interval is $(\Delta s)^2 = (2L)^2$. The invariant interval can be rewritten as

$$ds^2 = \eta_{\mu\nu} dx^\mu dx^\nu , \quad (1.2.11)$$

where the greek indices can take the values $\{0, 1, 2, 3\}$, $x^0 = t$, $x^1 = x$, $x^2 = y$, $x^3 = z$, and the *Minkowski metric* η is defined by

$$\eta = \begin{bmatrix} -c^2 & 0 & 0 & 0 \\ 0 & 1 & 0 & 0 \\ 0 & 0 & 1 & 0 \\ 0 & 0 & 0 & 1 \end{bmatrix} . \quad (1.2.12)$$

Repeated indices indicate an implied summation over the values those indices can take.

Special relativity gained widespread acceptance, partly due the the results of the Michelson-Morley experiment, an attempt in 1887 to measure the relative velocity of the luminiferous aether, a postulated medium through which electromagnetic waves (i.e., light) propagated. Laser light was sent through a beamsplitter down two perpendicular arms with several mirrors at the ends so that the light took several trips down the arms before being sent to a telescope to produce a fringe pattern. The instrument described here, similar to what was used in the thought experiment above (Fig. 1), is called a *Michelson interferometer*. The goal of the experiment was to measure differences in the speed of light in perpendicular directions in order to infer the relative velocity of the aether. The interferometer was rotated in a pool of mercury to observe the effect of changing its orientation relative to the aether's velocity. If Earth was moving relative to the aether, the fringe pattern was predicted to undergo two cycles of periodic change per rotation of the interferometer. This was done at different times of day and year to ensure

that the experiment was not always stationary relative to the aether. The experiment, however, produced a null result, as the measured velocity of the aether was consistent with zero, and clearly inconsistent with the aether theories at the time. Although perplexing at the time, this result was seen to be consistent with special relativity almost two decades later. Ironically, similar experiments today using Michelson interferometers to detect gravitational waves are again confirming the predictions of relativity, this time by yielding the opposite result, namely, changes in the the output of the interferometers.

The far-reaching implications of special relativity included a complete rethinking of the description of gravity. The concept of action at a distance in Newton's universal law of gravitation is incompatible with special relativity since it describes a force between two distant masses that depends on their relative positions in space at each instant in time. According to special relativity, the relative positions of the masses depends on frame of reference, leading to inconsistent results for the Newtonian gravitational force between them. Einstein therefore faced the problem of generalizing his theory to include non-inertial (i.e. accelerating) reference frames and gravitational fields.

1.3 A brief description of general relativity

Einstein's theory of general relativity, published in 1915 [6], describes gravity not as a force, but as the result of the curvature of spacetime. In the development of general relativity, Einstein was guided by the *equivalence principle*, which flows from the indistinguishability of gravitational and inertial mass. The equivalence principle states that in a sufficiently small region of spacetime, any experiment done by a freely falling observer in a gravitational field will produce results identical to those of an experiment done in an inertial (that is, non-accelerating) reference frame in the absence of a gravitational field. In other words, the perceived "force" of gravity is locally indistinguishable from a pseudo force felt by an observer in an accelerated reference frame such as a rocket at takeoff. Additionally, Einstein extended the principle of relativity to a new principle called the *principle of general covariance*, which states that the laws of physics must have the same

form in any coordinate system, including non-inertial frames of reference. This required the introduction of a general spacetime metric tensor $g_{\mu\nu}$, which can deviate from the flat-spacetime Minkowski metric of special relativity $\eta_{\mu\nu}$ to describe curved spacetimes.

The discussion in the following four sections relies heavily on the discussion in Chapter 2 of [7]. More comprehensive texts on general relativity can be found in [8] and [9].

1.3.1 Differential geometry

Distances

Spacetime in general relativity is described as a four-dimensional manifold whose structure can be quite complicated in principle. The distance between two points separated by an infinitesimal coordinate distance dx^α is found using

$$ds^2 = g_{\mu\nu}(x^\alpha) dx^\mu dx^\nu . \quad (1.3.1)$$

where the spacetime metric tensor $g_{\mu\nu}(x^\alpha)$ is a function of the spacetime coordinates x^α .

Under a coordinate transformation $x^\mu \rightarrow x'^\alpha$, the metric transforms according to

$$g'_{\alpha\beta} = g_{\mu\nu} \frac{\partial x^\mu}{\partial x'^\alpha} \frac{\partial x^\nu}{\partial x'^\beta} . \quad (1.3.2)$$

Vectors

In general manifolds, vectors are not properly thought of as stretching from one point in spacetime to another, but are instead described as directional derivatives. Consider a parameterized curve in spacetime described by the coordinates $x^\alpha(t)$, where t is the curve parameter. Letting $F(x^\alpha)$ be a function of the spacetime coordinates, we define the function $f(t) = F(x^\alpha(t))$, a function of the curve parameter. Then

$$\frac{df}{dt} = \frac{dx^\mu}{dt} \frac{\partial F}{\partial x^\mu} = u^\mu \frac{\partial F}{\partial x^\mu} , \quad (1.3.3)$$

where u^μ are the components of the tangent vector to the curve, $\mathbf{u} = d/dt$. An inner product between two vectors can be defined using the metric:

$$\mathbf{u} \cdot \mathbf{v} \equiv g_{\mu\nu} u^\mu v^\nu = u_\nu v^\nu , \quad (1.3.4)$$

where we have used the metric to lower an index: $g_{\mu\nu}u^\mu = u_\nu$. The norm of a vector is therefore $\|\mathbf{u}\| = g_{\mu\nu}u^\mu u^\nu = u_\nu u^\nu$.

Covariant derivatives

Using our definition of vectors, let us now define a derivative operator ∇_μ such that the operation $u^\mu \nabla_\mu v^\alpha$ along a vector \mathbf{u} on an arbitrary vector field \mathbf{v} produces a result that is invariant under general coordinate transformations. This is a *covariant derivative*, so called because it transforms covariantly under general coordinate transformations. The covariant derivative is not always equal to the ordinary derivative operator $\partial/\partial x^\alpha$, though it is always possible to find coordinates in which, locally, it is. Let x^α be an arbitrary set of coordinates and x'^μ be a set of coordinates in which the covariant derivative is equal to the ordinary derivative. Then, the covariant derivative is related to the ordinary derivative by

$$\nabla_\alpha v^\gamma = \frac{\partial v^\gamma}{\partial x^\alpha} + \Gamma_{\alpha\beta}^\gamma v^\beta, \quad (1.3.5)$$

where

$$\Gamma_{\alpha\beta}^\gamma \equiv \frac{\partial x^\gamma}{\partial x'^\mu} \frac{\partial^2 x'^\mu}{\partial x^\alpha \partial x^\beta} \quad (1.3.6)$$

are called the *connection coefficients*.

At this point, let us consider the shifting of a vector from one location to another by means of a process called *parallel transport*. In flat spacetime, this simply means that the direction of the vector is unchanged at each point as it is moved from the starting point to the ending point. In curved spacetime, this process can be described by requiring that the vector is unchanged during each infinitesimal displacement. For a vector \mathbf{v} being transported along a curve parameterized by the parameter t with tangent vector $\mathbf{u} = d/dt$, the requirement enforced by parallel transport is

$$0 = \frac{dv^\alpha}{dt} = u^\mu \nabla_\mu v^\alpha. \quad (1.3.7)$$

Due to curvature, a vector arrived at by parallel transport over a distance that is not infinitesimal depends on the path taken. To see this, imagine parallel transporting a vector that points north from the equator to the north pole through the 2-dimensional

curved space defined by Earth's surface. Consider the direction of the vector once it arrives at the north pole if it is taken straight north, by the shortest route possible. Then imagine its final direction if it is first transported along the equator a distance equal to $1/4$ of the Earth's circumference. Its final orientation would differ by 90° , due to the curvature of the Earth's surface.

Geodesics

According to Newton's first law of motion [4], "Every body perseveres in its state of rest, or of uniform motion in a straight line, unless it is compelled to change that state by forces impressed on it." In an inertial frame of reference, the straight-line or stationary path of such a body through spacetime describes what is called a *geodesic*. According to the equivalence principle, a freely falling particle with no external force acting must also follow a geodesic. In curved spacetime, a curve is a geodesic if and only if the tangent vector to that curve is parallel transported along itself. That is, a curve $x^\alpha(t)$ with tangent vector $\mathbf{u} = d/dt$ is a geodesic if

$$u^\mu \nabla_\mu u^\alpha = 0. \quad (1.3.8)$$

Using the definition $u^\alpha = dx^\alpha/dt$, we can rewrite this to show that a geodesic satisfies

$$\frac{d^2 x^\alpha}{dt^2} = -\Gamma_{\mu\nu}^\alpha \frac{dx^\mu}{dt} \frac{dx^\nu}{dt}. \quad (1.3.9)$$

A geodesic describes the straightest possible curve in curved spacetime, and the geodesic equation (Eq. 1.3.8) describes the path of a free particle through spacetime.

Curvature

To describe the curvature of spacetime, we will consider the effect of parallel transporting vectors from one point to another along different paths. Consider two *commuting* vector fields $\mathbf{u} = d/dt$ and $\mathbf{v} = d/ds$ used to construct a quadrilateral \mathcal{PQRS} . Two vector fields are said to commute if the point reached by traveling a path of fixed distance along each vector field is independent of the order in which those paths are traveled, that is,

$$u^\mu \nabla_\mu v^\alpha = v^\mu \nabla_\mu u^\alpha. \quad (1.3.10)$$

Point \mathcal{Q} is reached by traveling a distance Δt from point \mathcal{P} along the integral curve of \mathbf{u} . Point \mathcal{S} is reached by traveling a distance Δs from point \mathcal{P} along the integral curve of \mathbf{v} . Point \mathcal{R} can be reached by traveling a distance Δs from point \mathcal{Q} along the integral curve of \mathbf{v} or by traveling distance Δt from point \mathcal{S} along the integral curve of \mathbf{u} . Consider a smooth vector field \mathbf{w} whose value at point \mathcal{P} is $\mathbf{w}(\mathcal{P}) = \mathbf{w}_{\mathcal{P}}$. We will measure curvature by parallel transporting $\mathbf{w}_{\mathcal{P}}$ from point \mathcal{P} to point \mathcal{R} along two different paths, one via point \mathcal{Q} and one via point \mathcal{S} , and determine the difference in the resulting vectors. We begin by finding the difference between the vector $\mathbf{w}(\mathcal{R})$ and the vector $\mathbf{w}_{\mathcal{P} \rightarrow \mathcal{Q} \rightarrow \mathcal{R}}$, resulting from the parallel transport of vector $\mathbf{w}_{\mathcal{P}}$ to point \mathcal{R} via point \mathcal{Q} :

$$(\delta w^\delta)_{\mathcal{P} \rightarrow \mathcal{Q} \rightarrow \mathcal{R}} = w^\delta(\mathcal{R}) - w_{\mathcal{P} \rightarrow \mathcal{Q} \rightarrow \mathcal{R}}^\delta = (\Delta s \Delta t) v^\beta \nabla_\beta (u^\alpha \nabla_\alpha w^\delta). \quad (1.3.11)$$

Via point \mathcal{S} , the difference is

$$(\delta w^\delta)_{\mathcal{P} \rightarrow \mathcal{S} \rightarrow \mathcal{R}} = w^\delta(\mathcal{R}) - w_{\mathcal{P} \rightarrow \mathcal{S} \rightarrow \mathcal{R}}^\delta = (\Delta s \Delta t) u^\alpha \nabla_\alpha (v^\beta \nabla_\beta w^\delta). \quad (1.3.12)$$

Then the difference in the two parallel transported vectors is

$$\begin{aligned} w_{\mathcal{P} \rightarrow \mathcal{S} \rightarrow \mathcal{R}}^\delta - w_{\mathcal{P} \rightarrow \mathcal{Q} \rightarrow \mathcal{R}}^\delta &= (\delta w^\delta)_{\mathcal{P} \rightarrow \mathcal{Q} \rightarrow \mathcal{R}} - (\delta w^\delta)_{\mathcal{P} \rightarrow \mathcal{S} \rightarrow \mathcal{R}} \\ &= (\Delta s \Delta t) [v^\beta \nabla_\beta (u^\alpha \nabla_\alpha w^\delta) - u^\alpha \nabla_\alpha (v^\beta \nabla_\beta w^\delta)] \\ &= (\Delta s \Delta t) [(v^\beta \nabla_\beta u^\alpha) \nabla_\alpha w^\delta - (u^\alpha \nabla_\alpha v^\beta) \nabla_\beta w^\delta + u^\alpha v^\beta (\nabla_\beta \nabla_\alpha - \nabla_\alpha \nabla_\beta) w^\delta] \\ &= -(\Delta s \Delta t) u^\alpha v^\beta (\nabla_\alpha \nabla_\beta - \nabla_\beta \nabla_\alpha) w^\delta \\ &= (\Delta s \Delta t) R_{\alpha\beta\gamma}{}^\delta u^\alpha v^\beta w^\gamma, \end{aligned} \quad (1.3.13)$$

where $R_{\alpha\beta\gamma}{}^\delta$ is the *Riemann curvature tensor*, defined by

$$R_{\alpha\beta\gamma}{}^\delta w^\gamma \equiv -(\nabla_\alpha \nabla_\beta - \nabla_\beta \nabla_\alpha) w^\delta. \quad (1.3.14)$$

The Riemann curvature tensor provides a measure of the intrinsic curvature at each point in a manifold by measuring the failure of a vector parallel transported around a loop to point in its original direction.

1.3.2 The Einstein field equations

We have already seen how the motion of free particles following geodesics is dictated by the curvature of spacetime. We now wish to use tools from differential geometry to

describe how matter and energy affect the curvature of spacetime. First, we must define a few useful tensors that can be constructed from the Riemann curvature tensor. The *Ricci tensor* is found by contracting two indices of the Riemann curvature tensor:

$$R_{\alpha\beta} \equiv R_{\alpha\mu\beta}{}^{\mu}. \quad (1.3.15)$$

The *Ricci scalar* is defined by contracting two more indices using the metric:

$$R \equiv g^{\mu\nu} R_{\mu\nu}. \quad (1.3.16)$$

The divergenceless *Einstein tensor* is defined by

$$G_{\alpha\beta} \equiv R_{\alpha\beta} - \frac{1}{2}g_{\alpha\beta}R. \quad (1.3.17)$$

The *Einstein field equations*, which describe the generation of gravitational fields due to matter and energy, are

$$G_{\alpha\beta} = \frac{8\pi G}{c^4} T_{\alpha\beta}, \quad (1.3.18)$$

where $T_{\alpha\beta}$ are the components of the *stress-energy tensor*, defined by

$$\mathbf{T} \equiv \left[\begin{array}{c|c} \left(\begin{array}{c} \text{mass density} \\ \rho \end{array} \right) & \left(\begin{array}{c} \text{momentum density} \\ \mathbf{j} \end{array} \right) \\ \hline \left(\begin{array}{c} \text{momentum density} \\ \mathbf{j} \end{array} \right) & \left(\begin{array}{c} \text{stress tensor} \\ \mathbf{S} \end{array} \right) \end{array} \right]. \quad (1.3.19)$$

The component $T_{00} = \rho$ is mass density as a function over spacetime, the most familiar source of gravitational fields. The 6 components T_{0i} and T_{i0} are the momentum density \mathbf{j} . The remaining 9 components T_{ij} are the components of the classical stress tensor \mathbf{S} .

1.3.3 Linearized gravity and the wave solution

Now let us consider the Einstein field equations in the limit of weak gravitational fields. We write the metric tensor as the sum of the Minkowski metric of flat spacetime and a small perturbation: $g_{\alpha\beta} = \eta_{\alpha\beta} + h_{\alpha\beta}$. In this limit, we will use the Minkowski metric $\eta_{\alpha\beta}$ to raise and lower indices, except for those of the metric itself:

$$g^{\alpha\beta} = (g_{\alpha\beta})^{-1} = \eta^{\alpha\beta} - h^{\alpha\beta} + O(h^2). \quad (1.3.20)$$

Under this approximation, called the *linearized gravity* approximation, the Riemann tensor takes the form

$$R_{\alpha\beta\gamma\delta} = \frac{1}{2} \left(-\frac{\partial^2 h_{\beta\delta}}{\partial x^\alpha \partial x^\gamma} + \frac{\partial^2 h_{\beta\gamma}}{\partial x^\alpha \partial x^\delta} + \frac{\partial^2 h_{\alpha\delta}}{\partial x^\beta \partial x^\gamma} - \frac{\partial^2 h_{\alpha\gamma}}{\partial x^\beta \partial x^\delta} \right) + O(h^2). \quad (1.3.21)$$

The linearized Ricci tensor therefore takes the form

$$R_{\alpha\beta} = R_{\alpha\mu\beta}{}^\mu = \frac{1}{2} \left(-\frac{\partial^2 h}{\partial x^\alpha \partial x^\beta} + \frac{\partial^2 h^\mu{}_\beta}{\partial x^\alpha \partial x^\mu} + \frac{\partial^2 h_{\alpha\mu}}{\partial x^\mu \partial x^\beta} - \eta^{\mu\nu} \frac{\partial^2 h_{\alpha\beta}}{\partial x^\mu \partial x^\nu} \right) + O(h^2), \quad (1.3.22)$$

where $h = h_\mu{}^\mu$ is the trace of $h_\mu{}^\nu$, and the linearized Ricci scalar is

$$R = \eta^{\alpha\beta} R_{\alpha\beta} + O(h^2) = \frac{\partial^2 h^{\mu\nu}}{\partial x^\mu \partial x^\nu} - \eta^{\mu\nu} \frac{\partial^2 h}{\partial x^\mu \partial x^\nu} + O(h^2). \quad (1.3.23)$$

The form of the Einstein tensor in the Einstein field equations can be simplified by writing it in terms of the *trace-reversed metric perturbation* $\bar{h}_{\alpha\beta}$, given by

$$\bar{h}_{\alpha\beta} \equiv h_{\alpha\beta} - \frac{1}{2} \eta_{\alpha\beta} h. \quad (1.3.24)$$

Then, the linearized field equations can be expressed as

$$-\eta^{\mu\nu} \frac{\partial^2 \bar{h}_{\alpha\beta}}{\partial x^\mu \partial x^\nu} - \eta_{\alpha\beta} \frac{\partial^2 \bar{h}^{\mu\nu}}{\partial x^\mu \partial x^\nu} + \frac{\partial^2 \bar{h}^\mu{}_\beta}{\partial x^\alpha \partial x^\mu} + \frac{\partial^2 \bar{h}^\mu{}_\alpha}{\partial x^\mu \partial x^\beta} + O(h^2) = \frac{16\pi G}{c^4} T_{\alpha\beta}. \quad (1.3.25)$$

The first term on the left is $-\square \bar{h}_{\alpha\beta}$, where \square is the d'Alembertian operator, that is, the wave operator in flat spacetime. The remaining terms are all computed from the divergence of the trace-reversed metric perturbation $\bar{h}_{\alpha\beta}$. It turns out that it is possible, in general, to find coordinates in which $\bar{h}^{\alpha\beta}$ is divergenceless, that is, $\partial h^{\mu\alpha} / \partial x^\mu = 0$. This choice of coordinates is called the *Lorenz gauge*. In the Lorenz gauge, the linearized Einstein field equations take the form of an inhomogeneous wave equation with wave speed c and the stress-energy tensor acting as a source:

$$-\square \bar{h}_{\alpha\beta} = \frac{16\pi G}{c^4} T_{\alpha\beta}. \quad (1.3.26)$$

The wave solution of the linearized field equations led Einstein to predict the existence of gravitational waves (GWs) in 1916 [10], a prediction that was confirmed by the direct detection of GWs almost a century later [11]. It is worth noting that there is gauge freedom remaining in the Lorenz gauge, meaning that there still exist redundant degrees

of freedom in our coordinates, allowing further coordinate choices to be made without affecting anything physical. In particular, a solution of the homogeneous wave equation $\square\xi_\beta = 0$ can always be added.

1.3.4 The transverse traceless gauge

Let us now consider a particular solution of the Einstein field equations in the Lorenz gauge, in the absence of matter—that of a purely spatial plane wave traveling in the $z = x^3$ direction. This solution must satisfy the vacuum Einstein field equations in the Lorenz gauge

$$\square\bar{h}_{\alpha\beta} = 0 \quad (1.3.27)$$

as well as the Lorenz gauge condition

$$\frac{\partial\bar{h}^{\mu\alpha}}{\partial x^\mu} = 0. \quad (1.3.28)$$

The choice of a plane-wave solution in the z -direction adds the simplifying requirement that all components of the metric perturbation are functions of only the retarded time $t - z/c$. Given this choice, the Lorenz gauge condition requires that $\partial\bar{h}^{0\alpha}/\partial t = 0$ and $\partial\bar{h}^{3\alpha}/\partial z = 0$. The condition $\bar{h}^{0\alpha} = 0$ is also necessary, a gauge choice which makes the wave purely spatial. $\bar{h}^{3\alpha}$ is also a constant which we choose to set to zero. The only non-vanishing components of the trace-reversed metric perturbation are therefore $\bar{h}_{11}(t - z/c)$, $\bar{h}_{22}(t - z/c)$, and $\bar{h}_{12}(t - z/c) = \bar{h}_{21}(t - z/c)$, where the equality of \bar{h}_{12} and \bar{h}_{21} follows from the symmetry of the metric tensor. The non-vanishing components of the metric perturbation $h_{\alpha\beta} = \bar{h}_{\alpha\beta} - \frac{1}{2}\eta_{\alpha\beta}\bar{h}$ are therefore

$$h_{00} = -c^2 h_{33} = \frac{1}{2}c^2 (\bar{h}_{11} + \bar{h}_{22}) \quad (1.3.29a)$$

$$h_{11} = -h_{22} = \frac{1}{2} (\bar{h}_{11} - \bar{h}_{22}) \quad (1.3.29b)$$

$$h_{12} = h_{21} = \bar{h}_{12}. \quad (1.3.29c)$$

Let us now use any remaining gauge freedom to simplify this result and determine which, if any, of the above terms are physical, and which, if any, are artifacts of our current gauge choice. The linearized Riemann tensor of Eq. 1.3.21 is gauge invariant,

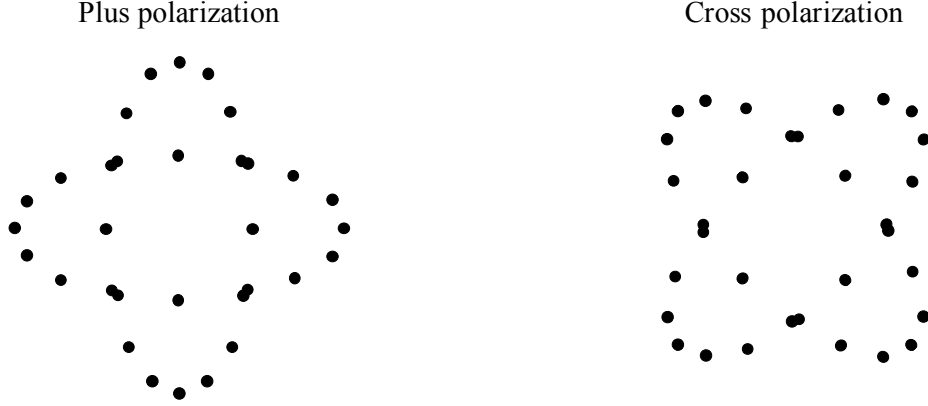


Figure 2 : The effect of gravitational waves traveling in a direction perpendicular to the page on a ring of free particles. In the transverse traceless gauge, each particle undergoes oscillatory motion of equal amplitude in a different direction as it follows a geodesic through spacetime. The “plus” and “cross” polarizations are shown. Any polarization allowed by general relativity can be produced as a linear combination of these two polarizations.

meaning that its non-vanishing components as computed from the metric perturbation $h_{\alpha\beta}$ correspond to real physical effects. Since the components $h_{\alpha\beta}$ are functions of only the retarded time $t - z/c$, it is necessary to consider only derivatives with respect to t to find the independent non-vanishing components of $R_{\alpha\beta\gamma\delta}$. The only two independent non-vanishing components are

$$R_{0101} = -\frac{1}{2} \frac{\partial^2}{\partial t^2} h_{11} \quad (1.3.30a)$$

$$R_{0102} = -\frac{1}{2} \frac{\partial^2}{\partial t^2} h_{12} \quad (1.3.30b)$$

We can therefore conclude that the metric perturbation components h_{11} , h_{22} , h_{12} , and h_{21} correspond to true physical effects, and that GWs are physical as well. Metric perturbations caused by GWs therefore have two independent degrees of freedom called h_+ (“h-plus”) and h_\times (“h-cross”), where $h_+ = h_{11} = -h_{22}$ and $h_\times = h_{12} = h_{21}$. The physical effect of GWs on a ring of free particles is shown in Fig. 2 for the two independent polarizations h_+ and h_\times . The components h_{00} and h_{33} are non-physical and can be removed by making an additional gauge choice. Doing so makes the perturbation purely spatial, and since $h_{11} = -h_{22}$, it also makes the metric perturbation traceless. This gauge is therefore called the *transverse traceless gauge*, or the TT gauge. GWs are transverse not only in the TT gauge, but in any Lorenz gauge. To see this, consider a monochromatic plane

wave given in terms of the trace-reversed metric perturbation by

$$\bar{h}_{\alpha\beta} = A_{\alpha\beta} \cos(k_\mu x^\mu), \quad (1.3.31)$$

where $A_{\alpha\beta}$ is a constant symmetric tensor and k_α is a constant wave vector. The Lorenz gauge condition requires that

$$0 = \frac{\partial \bar{h}^{\mu\alpha}}{\partial x^\mu} = -k_\mu A^{\mu\alpha} \sin(k_\nu x^\nu). \quad (1.3.32)$$

This is satisfied only if the wave is transverse, that is, if $k_\mu A^{\mu\alpha} = 0$. From any Lorenz gauge, it is possible to compute the TT-gauge metric perturbation using

$$h_{\alpha\beta}^{\text{TT}} = \bar{h}_{\alpha\beta} - \frac{\partial \xi_\beta}{\partial x^\alpha} - \frac{\partial \xi_\alpha}{\partial x^\beta} + \eta_{\alpha\beta} \eta^{\mu\nu} \frac{\partial \xi_\mu}{\partial x^\nu}, \quad (1.3.33)$$

where ξ_α is an appropriate solution of $\square \xi_\alpha = 0$ that makes $h_{\alpha\beta}^{\text{TT}}$ traceless.

1.4 The Advanced LIGO detectors

Decades before the direct detection of GWs in 2015, a study of the Hulse-Taylor binary provided compelling evidence of their existence [12]. The Hulse-Taylor binary is a neutron star binary system, in which one of the neutron stars is a known pulsar. The measured orbital decay of the Hulse-Taylor binary was shown to be consistent with that predicted due to the loss of energy and angular momentum due to gravitational radiation predicted by general relativity. In its first two observing runs (O1 and O2), the US-based Laser Interferometer Gravitational-wave Observatory (LIGO), along with the Virgo detector in Italy, has directly detected GW signals emitted by the inspirals and mergers of 10 binary black hole systems and one binary neutron star system [1], ushering in a new era of GW astronomy. The third observing run, O3, is now beginning, and due to significant increases in sensitivity, a significant increase in the rate of detections is expected. There are two LIGO detectors, one in Hanford, WA (H1), and one in Livingston, LA (L1).

The Advanced LIGO detectors are dual-recycled Michelson interferometers with two orthogonal arms that are approximately 4 km in length. A simplified diagram of an Advanced LIGO detector is shown in Fig. 3. Near-infrared (1064-nm) laser light is passed

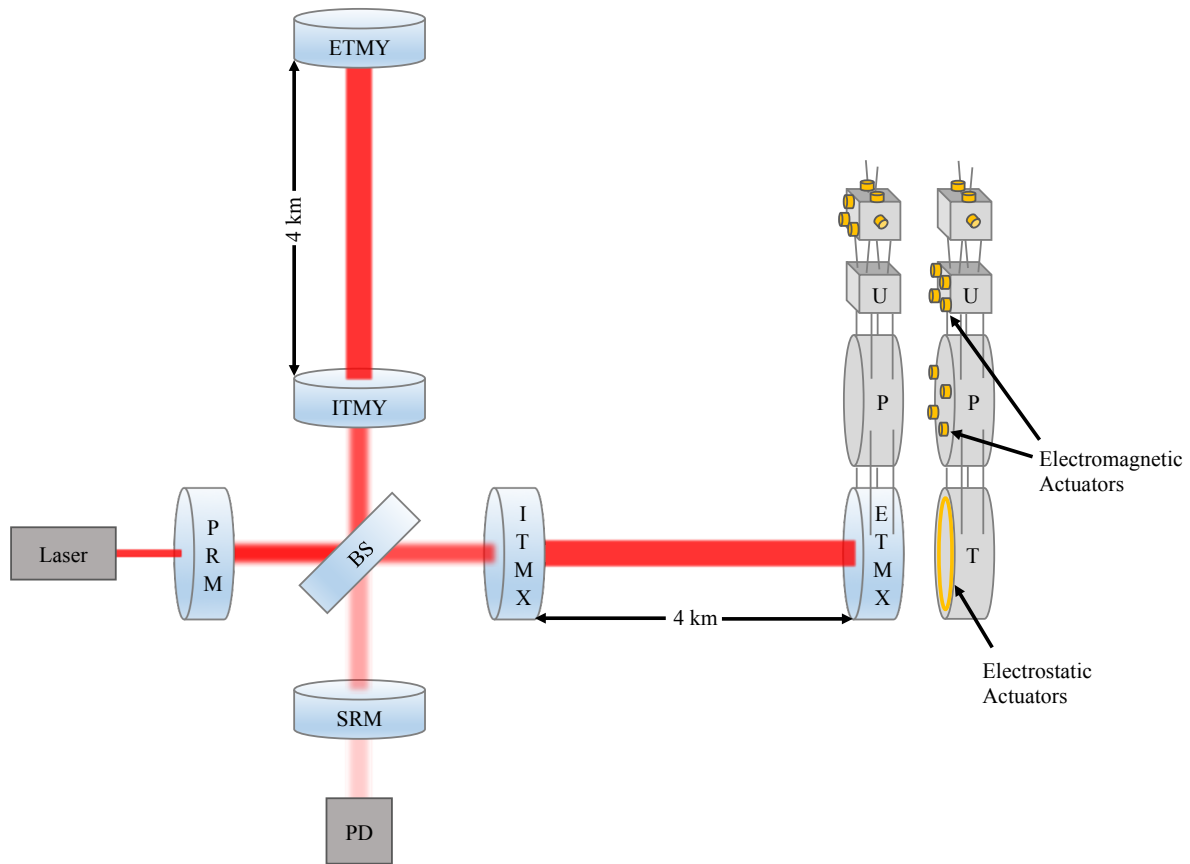


Figure 3 : A simplified diagram of an Advanced LIGO detector. Laser light enters from the left, passes through a power recycling mirror (PRM), and is sent down two orthogonal arms by a beamsplitter (BS). It then passes through the input test masses ITMX and ITMY to enter a pair of resonant Fabry-Perot cavities. Light reflects off of the end test masses ETMX and ETMY and the input test masses numerous times to increase the laser power stored in the 4-km arms by a factor of a few hundred. As light exits the Fabry-Perot cavities, most of it continues left toward the PRM to be reflected back into the detector. A faint signal is sent toward the signal recycling mirror (SRM), a portion of which escapes the detector to be measured by a photodetector (PD). A four-stage suspension system used to prevent excessive test mass motion is also shown, with an actuation system that actively suppresses low-frequency noise. The lowest three stages of the actuation system are used to control differential arm motion: the test mass (T) stage, the penultimate (P) stage, and the upper intermediate (U) stage.

through a beamsplitter into a pair of resonant Fabry-Perot cavities in each arm, before being reflected back to the beamsplitter by mirrors on the end test masses. In an unperturbed state, the length of each arm is held such that almost-completely destructive interference allows only a dim light to exit the detector at the GW readout port, where a photodiode measures the output light. Changes to the differential arm (DARM) degree

of freedom in the motion of the four test masses due to both GWs and noise cause fluctuations in the light exiting the detector at the GW readout port. Active seismic isolation is used to reduce motion in the four test masses caused by environmental noise sources. Additionally, each test mass is suspended as the bottom stage of a quadrupole suspension system, also shown in Fig. 3. Despite these efforts to reduce unwanted test-mass motion, achieving a stable low-noise configuration requires additional mitigation of low-frequency (below ~ 100 Hz) noise. This is accomplished by feedback control, using the detector's digital error signal, produced using the dim light recorded at the GW readout port, to inform an actuation system. The actuation systems operate using additional quadrupole suspension systems hung parallel to those of the test masses. At the test-mass stage, an electrostatic actuator is used to control motion in the test masses. At the penultimate and upper intermediate stages just above the test mass, electromagnetic actuators are used. An important distinguishing feature of the actuation, as compared to other methods of attenuating noise, is that the actuation also removes GW signals from the DARM readout. It is therefore necessary when reconstructing the strain signal to include the portion that was removed by the actuation.

The following sections describe the causal relationship between GWs incident on the detectors and the optical output of the detectors, as well as Advanced LIGO's sensitivity to DARM motion.

1.4.1 DARM response to gravitational waves

The strain signal in the detectors, h , is related to DARM motion by

$$h = \frac{\Delta L_x - \Delta L_y}{L}, \quad (1.4.1)$$

where ΔL_x and ΔL_y are changes in the length of the X-arm and Y-arm, respectively, and L is the average arm length. The strain signal h is therefore not the entire spacial metric perturbation h_{ij} , but a projection of h_{ij} onto the detectors. The response of DARM motion to incident GWs therefore depends on the sky location of the source and the polarization of the GWs. In general, GWs are elliptically polarized. Two special cases

are linear polarization and circular polarization. To see when these occur, consider a compact binary system with negligible eccentricity and spins. Linearly polarized GWs are emitted by such a system in all directions in the orbital plane, and circularly polarized GWs are emitted in the directions normal to the orbital plane. In the general case, it is always possible to write the spacial metric perturbation as a linear combination of the plus and cross polarizations:

$$\mathbf{h} = h_+ \hat{\mathbf{e}}^+ + h_\times \hat{\mathbf{e}}^\times, \quad (1.4.2)$$

where $\hat{\mathbf{e}}^+$ and $\hat{\mathbf{e}}^\times$ are orthogonal unit tensors in the transverse plane. As given in Appendix A of [7], the general form of the antenna response pattern for a LIGO detector, defined by $h = D^{ij} h_{ij}$, is

$$\mathbf{D}(\hat{\mathbf{n}}, f) = \frac{1}{2} (\hat{\mathbf{p}} \otimes \hat{\mathbf{p}}) D(\hat{\mathbf{p}} \cdot \hat{\mathbf{n}}, fL/c) - \frac{1}{2} (\hat{\mathbf{q}} \otimes \hat{\mathbf{q}}) D(\hat{\mathbf{q}} \cdot \hat{\mathbf{n}}, fL/c), \quad (1.4.3)$$

where $\hat{\mathbf{n}}$ is a unit vector in the direction of propagation of the GW, $\hat{\mathbf{p}}$ and $\hat{\mathbf{q}}$ are unit vectors in the directions of the X-arm and Y-arm, respectively, L is the average arm length, and f is the GW frequency. The function D is defined by

$$D(\mu, x) = \frac{1}{2} e^{2\pi i x} [e^{i\pi x(1-\mu)} \text{sinc}[x(1+\mu)] + e^{-i\pi x(1+\mu)} \text{sinc}[x(1-\mu)]] , \quad (1.4.4)$$

where $\text{sinc}(x) = \sin(\pi x)/(\pi x)$. In the long wavelength limit $fL/c \ll 1$, which is a good approximation throughout LIGO's most sensitive frequency band of 20 Hz to 1 kHz, $D \rightarrow 1$ and the antenna response pattern simplifies to

$$\mathbf{D}(\hat{\mathbf{n}}, f) = \frac{1}{2} (\hat{\mathbf{p}} \otimes \hat{\mathbf{p}} - \hat{\mathbf{q}} \otimes \hat{\mathbf{q}}) . \quad (1.4.5)$$

The strain signal in the detectors can also be written in terms of the polarization components h_+ and h_\times as

$$h = G_+ h_+ + G_\times h_\times, \quad (1.4.6)$$

where

$$G_+ \equiv D^{ij} \hat{e}_{ij}^+ \quad (1.4.7a)$$

$$G_\times \equiv D^{ij} \hat{e}_{ij}^\times. \quad (1.4.7b)$$

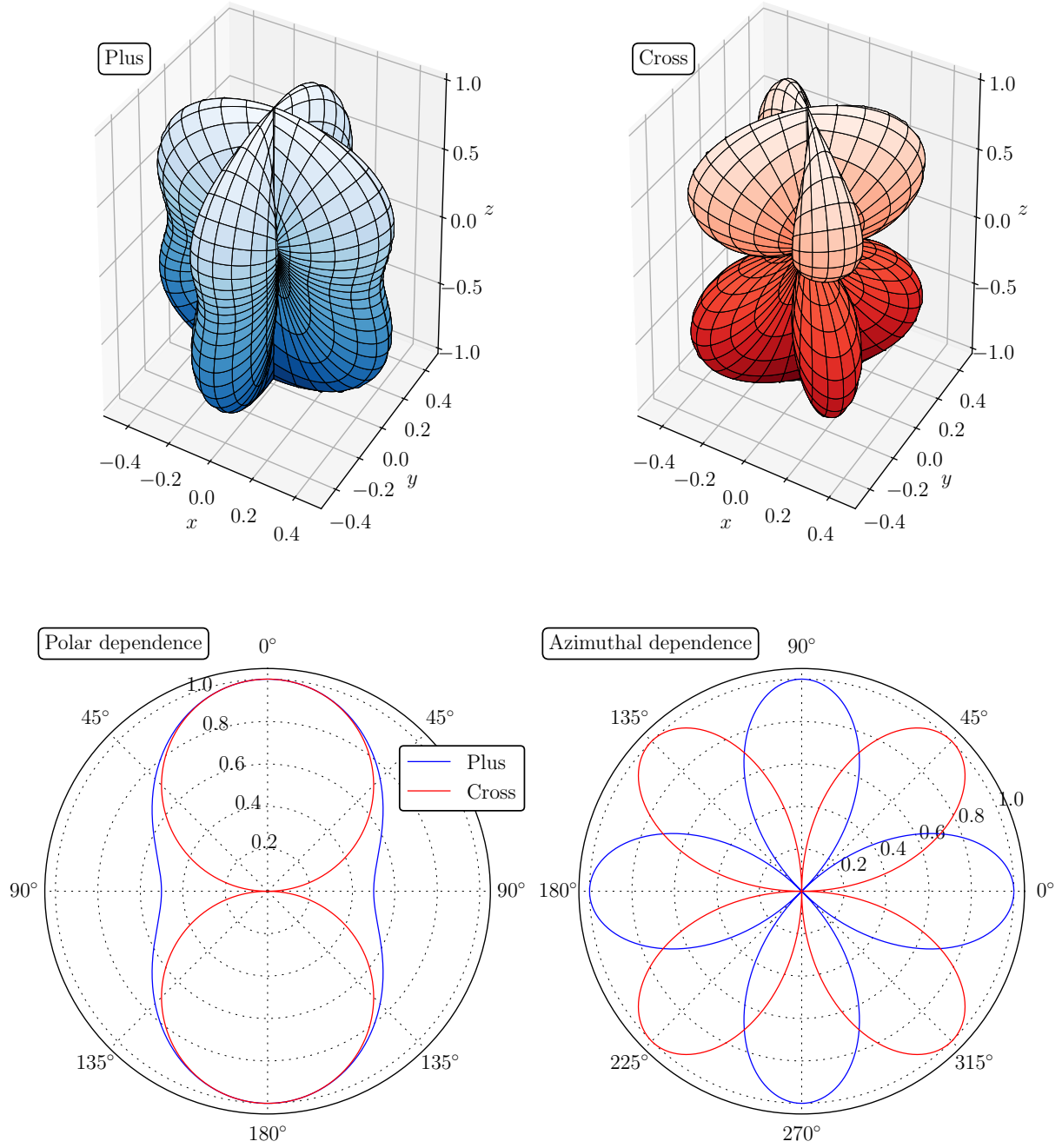


Figure 4 : Magnitude of the antenna response pattern of a LIGO detector, \mathbf{D} , defined by $h = D^{ij}h_{ij}$, as a function of the direction of travel of incident GWs, in the low-frequency limit. The components G_+ and G_\times , defined by $h = G_+h_+ + G_\times h_\times$, are shown separately. The z -axis here points vertically upward from the location of the detector, and the x and y axes point along the X-arm and Y-arm, respectively. θ is the polar angle, and ϕ is the azimuthal angle. For simplicity, we define the polarization unit tensors relative to the detector as well: $\hat{\mathbf{e}}^+ = \hat{\mathbf{e}}^\theta \otimes \hat{\mathbf{e}}^\theta - \hat{\mathbf{e}}^\phi \otimes \hat{\mathbf{e}}^\phi$, and $\hat{\mathbf{e}}^\times = \hat{\mathbf{e}}^\theta \otimes \hat{\mathbf{e}}^\phi + \hat{\mathbf{e}}^\phi \otimes \hat{\mathbf{e}}^\theta$. The radial distance represents the sensitivity. The dependence on θ and ϕ for each polarization are shown separately in the lower plots. The product of these two at each value of θ and ϕ produces the upper plots.

To show the dependence of G_+ and G_\times on sky position, let us choose a coordinate system defined relative to the detector, with the z -axis pointing vertically upward from the detector, and the x and y axes pointing along the X-arm and Y-arm of the detector, respectively. Then, for simplicity, we define the unit tensors $\hat{\mathbf{e}}_+$ and $\hat{\mathbf{e}}_\times$ relative to the detector as well:

$$\hat{\mathbf{e}}^+ = \hat{\mathbf{e}}^\theta \otimes \hat{\mathbf{e}}^\theta - \hat{\mathbf{e}}^\phi \otimes \hat{\mathbf{e}}^\phi \quad (1.4.8a)$$

$$\hat{\mathbf{e}}^\times = \hat{\mathbf{e}}^\theta \otimes \hat{\mathbf{e}}^\phi + \hat{\mathbf{e}}^\phi \otimes \hat{\mathbf{e}}^\theta, \quad (1.4.8b)$$

where $\hat{\mathbf{e}}^\theta$ is the unit vector corresponding to the polar angle θ , and $\hat{\mathbf{e}}^\phi$ is the unit vector corresponding to the azimuthal angle ϕ . Then, in the long-wavelength limit, the antenna response patterns of the detectors take the simple form

$$G_+(\theta, \phi) = [1 + \cos^2(\theta)] \cos(2\phi) \quad (1.4.9a)$$

$$G_\times(\theta, \phi) = \cos(\theta) \sin(2\phi). \quad (1.4.9b)$$

These antenna response patterns are shown in Fig. 4.

More general descriptions of detector antenna patterns can be found in [7] and [13].

1.4.2 The detectors' optical response to DARM motion

Having seen how the spacial metric perturbation due to GWs incident on the detector is related to changes in DARM, let us now consider how LIGO's primary observable, the light incident on the photodiode at the GW readout port, is related to physical DARM motion. In a low-noise configuration, this relationship is linear to a very good approximation, due to the positions at which the test masses are held and the small amplitude of their motion. Additionally, the optical response of the detectors is well modeled in the frequency domain by a *single pole approximation*. Let us now show that this is the case for a Fabry-Perot Michelson interferometer. To begin, first consider the optical response of a single Fabry-Perot cavity in the X-arm with a time-dependent length $L_x(t)$. We represent light incident on the X-end input test mass (ITM) outside the cavity by the constant electric field amplitude E_{IX} , and $E_{\text{FP}\triangleright}$ and $E_{\text{FP}\triangleleft}$ are the time-dependent

electric field amplitudes inside the cavity leaving and returning to the ITM, respectively. Then

$$E_{\text{FP}\triangleright}(t) = t_{\text{ITM}}E_{\text{IX}} - r_{\text{ITM}}E_{\text{FP}\triangleleft}(t) = t_{\text{ITM}}E_{\text{IX}} - r_{\text{ITM}}e^{-2ikL_x}E_{\text{FP}\triangleright}(t - 2L_x/c), \quad (1.4.10)$$

where r_{ITM} and t_{ITM} are the reflectivity and transmissivity of the ITM, respectively, and $k = \omega/c$ is the wavenumber of the light. Letting

$$E_{\text{FP}\triangleright}(t - 2L_x/c) = E_{\text{FP}\triangleright}(t) - \frac{2L_x}{c} \frac{dE_{\text{FP}\triangleright}}{dt} \quad (1.4.11)$$

and solving for $dE_{\text{FP}\triangleright}/dt$, we find that

$$\frac{dE_{\text{FP}\triangleright}}{dt} = \frac{c}{2L_x} \left[\left(1 + \frac{e^{2ikL_x}}{r_{\text{ITM}}} \right) E_{\text{FP}\triangleright}(t) - \frac{t_{\text{ITM}}}{r_{\text{ITM}}} e^{2ikL_x} E_{\text{I}} \right]. \quad (1.4.12)$$

Defining the equilibrium field

$$E_{\text{FP}\triangleright,\text{eq}} = \frac{t_{\text{ITM}}}{1 + r_{\text{ITM}}e^{-2ikL_x}} E_{\text{IX}}, \quad (1.4.13)$$

this can be rewritten as

$$\frac{dE_{\text{FP}\triangleright}}{dt} = \frac{1}{\tau} (E_{\text{FP}\triangleright,\text{eq}} - E_{\text{FP}\triangleright}(t)), \quad (1.4.14)$$

where the time constant τ is defined by

$$\frac{1}{\tau} = -\frac{c}{2L_x} \left(1 + \frac{e^{2ikL_x}}{r_{\text{ITM}}} \right). \quad (1.4.15)$$

When the Fabry-Perot cavity is at resonance, $L_x = L_{\text{res}}$ where $e^{-2ikL_{\text{res}}} = -1$, we see that $\tau > 0$, indicating that this is a stable equilibrium. The reflected field exiting the cavity at the X-end ITM is

$$E_{\text{RX}}(t) = r_{\text{ITM}}E_{\text{IX}} + t_{\text{ITM}}e^{-2ikL_x}E_{\text{FP}\triangleright}(t), \quad (1.4.16)$$

and therefore

$$\frac{dE_{\text{RX}}}{dt} = \frac{1}{\tau} (E_{\text{RX},\text{eq}} - E_{\text{RX}}(t)), \quad (1.4.17)$$

where the equilibrium field $E_{\text{RX},\text{eq}}$ is

$$E_{\text{RX},\text{eq}} = \left(\frac{r_{\text{ITM}} + e^{-2ikL_x}}{1 + r_{\text{ITM}}e^{-2ikL_x}} \right) E_{\text{IX}}. \quad (1.4.18)$$

When the cavity is at resonance, this simplifies to $E_{\text{RX,eq}} = -E_{\text{IX}}$. For small deviations from resonance,

$$E_{\text{RX,eq}} \approx -\exp\left(-2ik \frac{1+r_{\text{ITM}}}{1-r_{\text{ITM}}} \Delta L_x\right) E_{\text{IX}}. \quad (1.4.19)$$

Let us now consider the optical response of a Fabry-Perot Michelson interferometer, with the input test masses ITMX and ITMY located at distances ℓ_x and ℓ_y from the beam-splitter, respectively. In terms of the mean arm length $\bar{\ell} = (\ell_x + \ell_y)/2$ and the difference in arm lengths $\delta = \ell_x - \ell_y$,

$$E_{\text{GW}}(t) = e^{-ik\bar{\ell}} [E_{\text{RY}}(t)e^{ik\delta/2} - E_{\text{RX}}(t)e^{-ik\delta/2}], \quad (1.4.20)$$

where E_{GW} is the electric field amplitude exiting the detector at the GW readout port, and the behavior of the fields E_{RX} and E_{RY} near resonance is described by Eqs. 1.4.19 and 1.4.17. The fields incident on the input test masses are related to the field incident on the beamsplitter from the input laser E_{IN} by $E_{\text{IX}} = E_{\text{IN}}e^{-ik(\bar{\ell}+\delta/2)}$ and $E_{\text{IY}} = E_{\text{IN}}e^{-ik(\bar{\ell}-\delta/2)}$. The lengths ℓ_x and ℓ_y are set so that $e^{ik\bar{\ell}} = 1$ and $e^{ik\delta} = 1$. Therefore, using Eq. 1.4.17, we find that

$$\frac{dE_{\text{GW}}}{dt} = \frac{1}{\tau} (E_{\text{GW,eq}} - E_{\text{GW}}(t)), \quad (1.4.21)$$

where

$$\begin{aligned} E_{\text{GW,eq}} &= E_{\text{RY,eq}} - E_{\text{RX,eq}} \\ &\approx \left[\exp\left(-2ik \frac{1+r_{\text{ITM}}}{1-r_{\text{ITM}}} \Delta L_x\right) - \exp\left(-2ik \frac{1+r_{\text{ITM}}}{1-r_{\text{ITM}}} \Delta L_y\right) \right] E_{\text{IN}}. \end{aligned} \quad (1.4.22)$$

Expressing this in terms of DARM motion $\Delta L = \Delta L_x - \Delta L_y$ and common arm (CARM) motion $\Delta L_{\text{CARM}} = \Delta L_x + \Delta L_y$, we find

$$E_{\text{GW,eq}} \approx -2i \exp\left(-ik \frac{1+r_{\text{ITM}}}{1-r_{\text{ITM}}} \Delta L_{\text{CARM}}\right) \sin\left(k \frac{1+r_{\text{ITM}}}{1-r_{\text{ITM}}} \Delta L\right) E_{\text{IN}}. \quad (1.4.23)$$

Note that, for small deviations from resonance, only changes in DARM affect the amplitude of the result. The current generated in the photodiode is proportional to the intensity of the light at the GW readout port, so what we wish to measure is

$$|E_{\text{GW,eq}}|^2 \approx 4 \sin^2\left(k \frac{1+r_{\text{ITM}}}{1-r_{\text{ITM}}} \Delta L\right) |E_{\text{IN}}|^2. \quad (1.4.24)$$

When the detector is exactly at resonance, the change in photocurrent is quadratic in small changes in ΔL , resulting in a nonlinear detector response. This is problematic for several reasons, most notably the fact that the sign of ΔL cannot be inferred from such a photocurrent. Additionally, feedback control of the detector, as well as calibration models, assume linear transfer functions for the detector's response. To enforce linearity in the detector's response to small changes in DARM, a small offset ΔL_0 , called the DARM offset, is added so that the detector is near, but not exactly at, resonance. Making the replacement $\Delta L \rightarrow \Delta L_0 + \Delta L$ in Eq. 1.4.24, we can approximate that Eq. 1.4.24 is linear in small changes in ΔL . We therefore argue that, for small displacements,

$$I_{\text{GW,eq}}(t) \approx H_C \Delta L(t) + I_0, \quad (1.4.25)$$

where $I \propto |E|^2$ is intensity, H_C is the DC gain of the system, and I_0 is a constant offset related to the DARM offset. From Eq. 1.4.21, we find that

$$\frac{d}{dt} |E_{\text{GW}}|^2 = 2\Re \left[\frac{1}{\tau} (E_{\text{GW,eq}} E_{\text{GW}}^* - |E_{\text{GW}}|^2) \right]. \quad (1.4.26)$$

For small departures from equilibrium $E_{\text{GW}} = E_{\text{GW,eq}} + \epsilon$, this can be simplified to

$$\frac{d}{dt} I_{\text{GW}} \approx \frac{1}{\tau} (I_{\text{GW,eq}}(t) - I_{\text{GW}}(t)). \quad (1.4.27)$$

Let us now use Eqs. 1.4.27 and 1.4.25 to find I_{GW} as a function of ΔL and t . Rearranging, we have

$$\frac{dI_{\text{GW}}}{dt} + \frac{I_{\text{GW}}}{\tau} = \frac{1}{\tau} [H_C \Delta L(t) + I_0]. \quad (1.4.28)$$

After multiplying by the integrating factor $e^{t/\tau}$, this can be rewritten as

$$\frac{d}{dt} [I_{\text{GW}} e^{t/\tau}] = \frac{1}{\tau} [H_C \Delta L(t) + I_0] e^{t/\tau}. \quad (1.4.29)$$

The general solution is

$$I_{\text{GW}}(t) = I_0 + \frac{H_C}{\tau} e^{-t/\tau} \int_{-\infty}^t \Delta L(t') e^{t'/\tau} dt'. \quad (1.4.30)$$

It is instructive to consider the form of this solution for a sinusoidal input such as $\Delta L(t) = \cos(\omega t)$. Then Eq. 1.4.30 becomes

$$I_{\text{GW}}(t) = I_0 + \frac{H_C}{\tau} e^{-t/\tau} \int_{-\infty}^t \cos(\omega t') e^{t'/\tau} dt'. \quad (1.4.31)$$

An integration by parts leads to the result

$$I_{\text{GW}}(t) = I_0 + H_C \frac{\cos \omega t + \tau \omega \sin \omega t}{1 + \tau^2 \omega^2}. \quad (1.4.32)$$

This result shows the frequency dependence of the response of the system, and is consistent with the result we shall derive next. Now, let us take the Fourier transform of Eq. 1.4.30 to represent it in the frequency domain. Since the constant offset is trivial (it just adds a constant DC component to the result), it is omitted.

$$\widetilde{I}_{\text{GW}}(\omega) = \frac{H_C}{\tau} \int_{-\infty}^{\infty} e^{-t/\tau} e^{-i\omega t} \left(\int_{-\infty}^t \Delta L(t') e^{t'/\tau} dt' \right) dt. \quad (1.4.33)$$

Integration by parts leads to the result

$$\begin{aligned} \widetilde{I}_{\text{GW}}(\omega) &= \frac{H_C}{\tau} \left[\int_{-\infty}^t \Delta L(t') e^{t'/\tau} dt' \left(\frac{-e^{-t/\tau} e^{-i\omega t}}{1/\tau + i\omega} \right) \right] \Bigg|_{t=-\infty}^{t=\infty} \\ &\quad + \frac{H_C}{\tau} \left(\frac{1}{1/\tau + i\omega} \right) \int_{-\infty}^{\infty} e^{-t/\tau} e^{-i\omega t} \Delta L(t) e^{t/\tau} dt. \end{aligned} \quad (1.4.34)$$

The first term can be shown to vanish by L'Hospital's rule, and the second term leads to the simple result

$$\widetilde{I}_{\text{GW}}(\omega) = \frac{H_C}{1 + i\omega\tau} \widetilde{\Delta L}(\omega). \quad (1.4.35)$$

Writing this in terms of frequency $f = \omega/(2\pi)$ and defining the pole frequency $f_c = 1/(2\pi\tau)$, we can rewrite this as

$$\widetilde{I}_{\text{GW}}(f) = \frac{H_C}{1 + if/f_c} \widetilde{\Delta L}(f). \quad (1.4.36)$$

The parameter f_c in the sensing function of the detectors is called the *cavity pole* frequency, and it is discussed in detail in the following chapters. The addition of the power recycling mirror couples the Fabry-Perot cavities, but the single-pole behavior persists. We will not prove this here for the sake of brevity.

Note that the optical response derived here is not the full model of the sensing function, which additionally includes the response of various electronics, a time delay, and dependence at low frequencies on the response of the signal recycling cavity (the cavity between the beamsplitter and the signal recycling mirror, shown in Fig. 3). By design, the

signal recycling cavity has no frequency-dependent effect on the optical response; its purpose is to increase the detector's broadband sensitivity. In practice, the signal recycling cavity can be slightly detuned, leading to the frequency-dependent response described in Section 2.3. A thorough analysis of the response of the signal recycling cavity can be found in [14].

1.4.3 Sensitivity of the detectors to DARM motion

The goal of the Advanced LIGO detectors is to detect GW signals in the frequency band from 10 Hz to 5 kHz. Thus far, Advanced LIGO has detected GW signals from the coalescence of compact binaries. Besides compact binary coalescences, other promising sources of GW signals in Advanced LIGO's detection band include rotating neutron stars emitting continuous waves, nearby supernovae, and the stochastic background of more distant GW events that are not individually resolvable. In order to make detections probable over the timescale of an observing run, Advanced LIGO needs a sensitivity and duty cycle sufficient to observe a volume of spacetime large enough to make GW events probable. Roughly speaking, this requires a sensitivity sufficient to measure strain signals with amplitude of the order $|h| \sim 10^{-21}$ or smaller. To see how this level of sensitivity is achieved, consider first the case of a simple Michelson interferometer without Fabry-Perot cavities or power or signal recycling mirrors. Let the length of both arms be $L \sim 1$ km and the wavelength of the input laser light be $\lambda_{\text{laser}} \sim 10^{-6}$ m. Let the detector's arms be held so that, in an unperturbed state, no light exits at the GW readout port. Changing the total path length of the laser beam in one arm by half of a wavelength requires changing the length of that arm by 1/4 of a wavelength, and will result in constructive interference:

$$|h| \sim \frac{\lambda_{\text{laser}}}{L} \sim \frac{10^{-6} \text{ m}}{10^3 \text{ m}} = 10^{-9}. \quad (1.4.37)$$

This is not even close to the sensitivity needed to make detections. However, several significant improvements can be made. First, the addition of the input test masses to create resonant Fabry-Perot cavities in each arm can increase the effective arm length by causing the laser light to circulate in the arms. The associated benefit is maximized

when the effective length is comparable to the wavelength of the GW signals we wish to detect, since further increase of light storage time means that the metric perturbation will change significantly during the time the light is in the cavities. The wavelength of GWs in Advanced LIGO's most sensitive band is $\lambda_{\text{GW}} \sim c/300 \text{ Hz} = 10^6 \text{ m}$. With this improvement, sensitivity improves to

$$|h| \sim \frac{\lambda_{\text{laser}}}{\ell_{\text{eff}}} \sim \frac{10^{-6} \text{ m}}{10^6 \text{ m}} = 10^{-12}. \quad (1.4.38)$$

The next significant improvement is in the measurement of the optical fringes. It is not necessary to move from a dark fringe to a bright fringe to make a measurement; much smaller changes in intensity can be measured. In fact, the dominant source of noise in the measurement of intensity of light at the GW readout port is photon shot noise, the quantum fluctuation in the number of photons arriving in a sampling period. The arrival of photons at the GW readout port is a Poisson process, meaning that, for an average value of N photons arriving in the time interval τ , the uncertainty in the number of photons is \sqrt{N} . Therefore, the minimum detectable change in optical path is of order

$$\Delta\ell \sim \frac{\sqrt{N}}{N} \lambda_{\text{laser}}. \quad (1.4.39)$$

Photons are collected over a time of the order of the period of the GW $\tau \sim 1/f_{\text{GW}}$. The number of photons collected also depends on the power of the laser P_{laser} and the energy per photon $hc/\lambda_{\text{laser}}$:

$$N = \frac{P_{\text{laser}}}{hc/\lambda_{\text{laser}}} \tau \sim \frac{P_{\text{laser}}}{hc/\lambda_{\text{laser}}} \frac{1}{f_{\text{GW}}}. \quad (1.4.40)$$

The laser power currently used is $\sim 40 \text{ W}$, so for a GW of frequency $f_{\text{GW}} \sim 300 \text{ Hz}$ and a laser wavelength of $\lambda_{\text{laser}} \sim 10^{-6} \text{ m}$, the number of photons is $N \sim 10^{18}$ photons. Then we find

$$|h| = \frac{\Delta\ell}{\ell_{\text{eff}}} \sim \frac{N^{-1/2} \lambda_{\text{laser}}}{\lambda_{\text{GW}}} \sim \frac{10^{-9} \times 10^{-6} \text{ m}}{10^6 \text{ m}} = 10^{-21}. \quad (1.4.41)$$

An additional improvement is achieved by increasing the laser power stored in the detector using a power recycling mirror at the symmetric output, as shown in Fig. 3. This increases power by a couple orders of magnitude, leading to about one order of magnitude of improvement in sensitivity. As laser power stored in the detector's arms increases, radiation pressure noise can become a competing source of noise at low frequency. Heavier

test masses can be used to reduce this effect. Advanced LIGO's test masses are 40 kg. A signal recycling mirror placed before the GW readout port further improves sensitivity in particular frequency bands. Lastly, quantum squeezing of input laser light is used to reduce shot noise and radiation pressure noise.

At the beginning of O3, as shown in Fig. 13, the sensitivity of the Advanced LIGO detectors in the most sensitive frequency band is a bit below $10^{-23} \text{ Hz}^{-1/2}$.

Chapter 2

Advanced LIGO calibration overview

The goal of Advanced LIGO's detectors is to measure GW signals and record them as a time series. However, the raw output of the detectors is not the GW strain; it is a digitized double-precision error signal called d_{err} sampled at 16384 Hz, in arbitrary units called counts, that represents the intensity of the laser light at the GW readout port as measured by a photodiode. Moreover, the relationship of the error signal to the GW strain is nontrivial, with dependence on both frequency and time.

Calibration of Advanced LIGO data entails reconstructing the strain signal in the detectors. GWs induce changes in the differential arm (DARM) length of the detectors:

$$\Delta L_{\text{free}}(t) = \Delta L_x(t) - \Delta L_y(t), \quad (2.0.1)$$

where ΔL_x and ΔL_y are changes in the length of the X-arm and the Y-arm, respectively. Despite the use of active seismic isolation and a quadrupole pendulum system to suppress low-frequency seismic noise, the detectors require additional mitigation of noise to achieve a stable low-noise state. This is achieved using feedback control through an actuation system which removes a controlled DARM length ΔL_{ctrl} from ΔL_{free} , to produce a residual DARM length:

$$\Delta L_{\text{res}} = \Delta L_{\text{free}} - \Delta L_{\text{ctrl}}. \quad (2.0.2)$$

The final calibration product is the dimensionless strain signal, defined as

$$h(t) = \frac{\Delta L_{\text{free}}(t)}{L}, \quad (2.0.3)$$

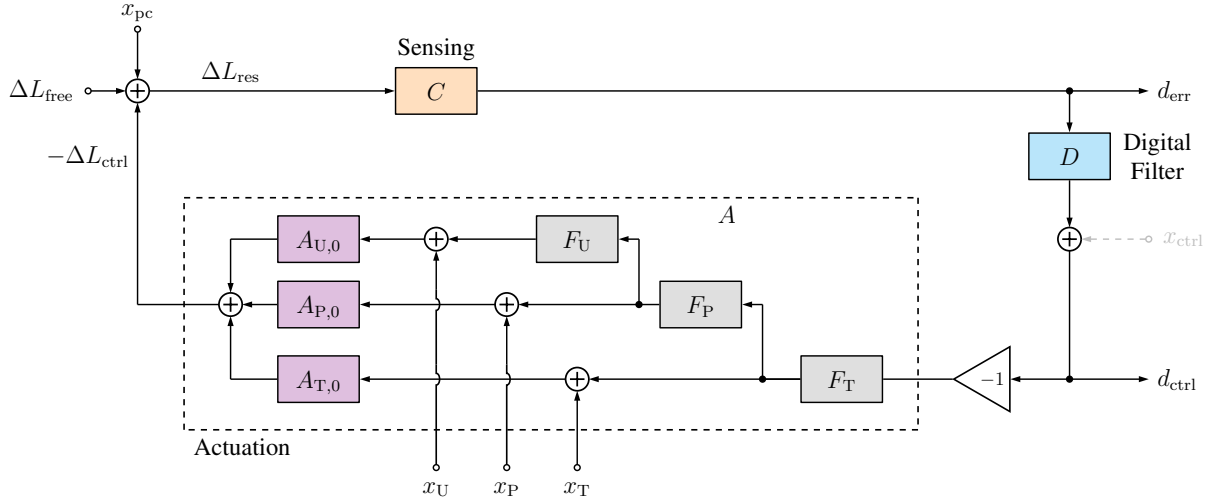


Figure 5 : A block diagram of the Advanced LIGO differential arm (DARM) feedback control loop. Noise and GW signals enter at the upper left as ΔL_{free} . The sensing function C represents the conversion from meters of residual DARM displacement ΔL_{res} to counts in the error signal d_{err} . The digital filter D is used to produce the control signal d_{ctrl} , which is sent to the actuation function A . The actuation function converts the control signal to a controlled DARM displacement ΔL_{ctrl} , which is removed from ΔL_{free} to produce ΔL_{res} . The actuation function is split into three stages A_j ($j \in \{T, P, U\}$), corresponding to the three stages of the suspensions system used to control DARM motion. The filter functions F_j include all filters (e.g., lock filters) that occur before injections in each stage, and the functions $A_{i,0}$ are the remaining portions of the A_j . The injections x_{pc} , made using the photon calibrator (Pcal), and x_i , made in each stage of the actuation, are used to measure the calibration at select frequencies. The injection x_{ctrl} was used during O2 instead of x_P and x_U .

where $L = (L_x + L_y)/2$ is the average length of the arms.

2.1 Black box models of the detector's response to gravitational waves

Changes in DARM cause fluctuations in the intensity of the laser light measured by the photodiode at the GW readout port, which is converted to the digital error signal d_{err} . The transfer function relating the error signal to residual DARM length changes is called the sensing function C and is defined by

$$\tilde{d}_{\text{err}}(f) = \tilde{C}(f)\tilde{\Delta L}_{\text{res}}(f), \quad (2.1.1)$$

where the tilde denotes a Fourier transform. The error signal is digitally filtered to produce a control signal d_{ctrl} :

$$\tilde{d}_{\text{ctrl}}(f) = \tilde{D}(f)\tilde{d}_{\text{err}}(f), \quad (2.1.2)$$

where the digital filter \tilde{D} acts primarily as a low-pass filter, but may also contain notches to remove resonant frequencies of the actuation such as violin modes. The control signal is then sent to the actuation system to remove excess low-frequency noise:

$$\widetilde{\Delta L}_{\text{ctrl}}(f) = \tilde{A}(f)\tilde{d}_{\text{ctrl}}(f). \quad (2.1.3)$$

This describes a feedback control loop called the DARM loop that is used to mitigate low-frequency noise, depicted in Fig. 5. The DARM loop can be used to solve for ΔL_{free} in terms of the error signal, the result being

$$\widetilde{\Delta L}_{\text{free}}(f) = \tilde{R}(f)\tilde{d}_{\text{err}}(f), \quad (2.1.4)$$

where R is the response function¹ given by

$$\tilde{R}(f) = \frac{1 + \tilde{A}(f)\tilde{D}(f)\tilde{C}(f)}{\tilde{C}(f)}. \quad (2.1.5)$$

However, this is not the method used by Advanced LIGO's calibration pipelines to compute $h(t)$. The solution used to compute $h(t)$ uses both the error and control signals:

$$\widetilde{\Delta L}_{\text{free}}(f) = \tilde{C}^{-1}(f)\tilde{d}_{\text{err}}(f) + \tilde{A}(f)\tilde{d}_{\text{ctrl}}(f). \quad (2.1.6)$$

The motivation behind using this method is to avoid using a calibration model that depends on the digital filter D , due to the fact that D can be changed for detector commissioning purposes and is not continuously measured in the calibration process. The methods discussed later in Chapter 5 to continuously track temporal variations in the calibration models do, however, have dependence on D , nullifying the benefit. This is an area of current development.

¹Note that R is not the response function of the detector, but the inverse, that is, the intended response function of the calibration.

Note that the sensing function C is a linear transfer function, and can therefore accurately model the relationship between ΔL_{res} and d_{err} only if that relationship is in fact linear. However, that relationship cannot be linear if the unperturbed state of the detector allows no light to exit at the GW readout port. Moreover, if this were the case, one could not determine the sign of ΔL_{res} . In order to ensure linearity, a small offset is digitally added into the DARM loop, so that in an unperturbed state, a small amount of light escapes to the GW readout port.

2.2 Time-domain calibration

Although calibration models are best represented analytically in the frequency domain, calibration of Advanced LIGO data is done in the time domain. This has been the case since Initial LIGO's second science run, and the development of the original time-domain calibration is described in [15]. An update of the methods used for time-domain calibration in Advanced LIGO is given in [16]. The primary benefit of applying the calibration model in the time domain, as opposed the frequency domain, is that the filtering of time-domain data can be done with very low latency, whereas taking Fourier transforms of consecutive segments of input data to apply a frequency-domain model adds latency.

Time-domain calibration requires the construction of digital filters using the frequency-domain models for \tilde{A} and \tilde{C}^{-1} . Finite impulse response (FIR) filters representing the models are then convolved with input data to apply the models:

$$h(t) = C^{-1} * d_{\text{err}}(t) + A * d_{\text{ctrl}}(t). \quad (2.2.1)$$

The operation

$$F * g(t) = \int_{-\infty}^{\infty} F(\tau)g(t - \tau)d\tau \quad (2.2.2)$$

denotes convolution of the filter F with the signal $g(t)$, equivalent to a point-by-point multiplication in the frequency domain.

2.3 Sensing function

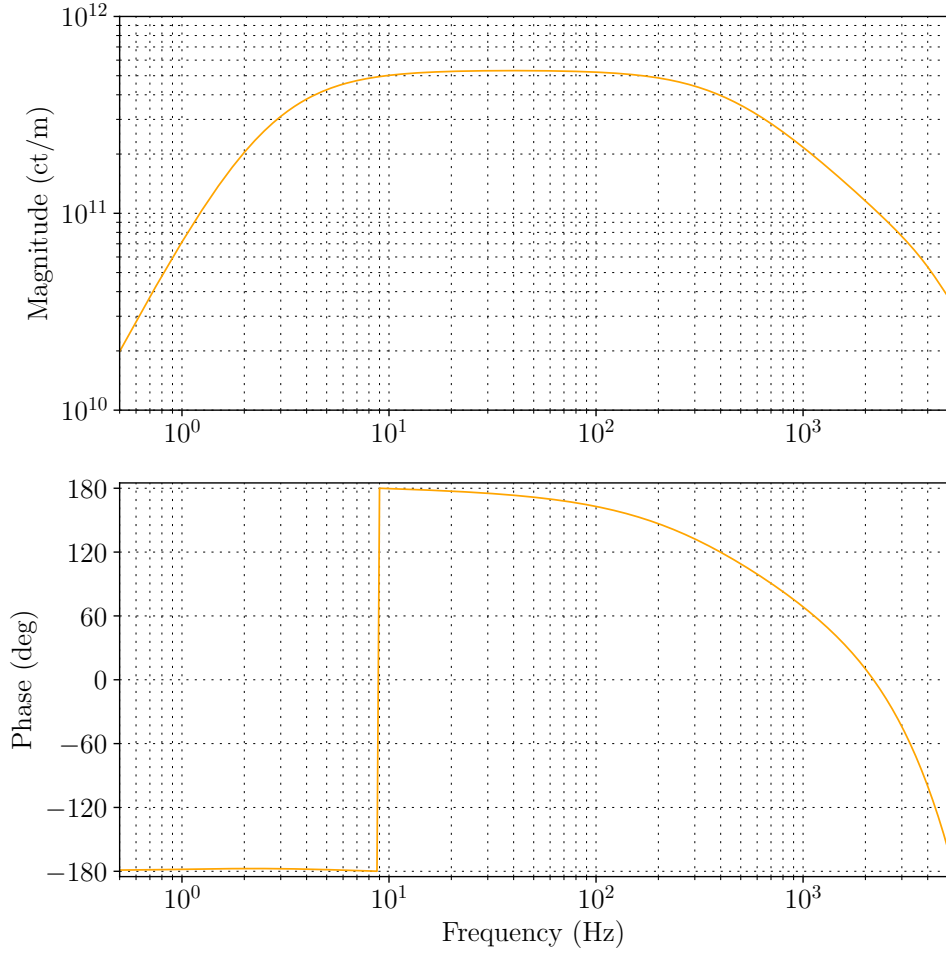


Figure 6 : A Bode plot of the sensing function model for the L1 detector before O3. Measurements used to produce this model were taken on 2019-01-17.

The full sensing function model used by the calibration pipelines is given by

$$\tilde{C}(f; t) = \kappa_C(t) \left(\frac{H_C}{1 + if/f_{cc}(t)} \right) \left(\frac{f^2}{f^2 + f_s^2(t) - if f_s(t)/Q(t)} \right) C_R(f) \exp[-2\pi if\tau_C]. \quad (2.3.1)$$

The gain H_C represents the conversion from meters of DARM displacement to counts. The dimensionless scalar $\kappa_C(t)$ encodes the time-dependence of the gain H_C , observed to fluctuate by $\sim 10\%$. The coupled cavity pole frequency $f_{cc}(t)$ is the characteristic frequency at which the detector response is significantly attenuated due to finite average photon storage time in the Fabry P erot cavities. During O3, the coupled cavity pole frequency is expected to have a value of ~ 400 Hz. τ_C is a constant time delay due to

light-travel time across the length of each arm and an additional time delay in acquiring the digital signal. The factor $C_R(f)$ encodes the remaining frequency dependence above ~ 1 kHz due to photodiode electronics and signal-processing filters. The second term in parenthesis represents the impact of the signal recycling cavity (SRC) on the detector response. $f_s(t)$ and $Q(t)$ are the resonant frequency and quality factor of the optical anti-spring of the SRC, respectively. An optical spring (or anti-spring) exists in an optomechanical cavity if there is a linear relationship between the length of the cavity and the photon pressure on the mirrors. The value of f_s is generally expected to remain below ~ 10 Hz.

A Bode plot showing the sensing function model for the L1 detector before O3 is shown in Fig. 6. The same model is used in Fig. 14, showing how well the calibration filters implement the application of the response function R to the raw data.

2.4 Actuation function

As depicted in Fig. 3, the actuation system utilizes a quadrupole pendulum systems hung parallel to the test-mass suspension system. The lowest three stages are used to control DARM motion in one of the arms (typically the X-arm). At the lowest stage, called the test mass (T) stage, an electrostatic actuator is used to control DARM motion. At the penultimate (P) and upper intermediate (U) stages, electromagnetic actuators are used. Digital filters are applied in each stage of the actuation to direct the low-frequency content to the higher stages and the high-frequency content to the lower stages. The full actuation model is given by

$$\begin{aligned} \tilde{A}(f; t) = & [\kappa_U(t)e^{2\pi i f \tau_U(t)} \tilde{F}_T(f) \tilde{F}_P(f) \tilde{F}_U(f) \tilde{A}_{U,0}(f) \\ & + \kappa_P(t)e^{2\pi i f \tau_P(t)} \tilde{F}_T(f) \tilde{F}_P(f) \tilde{A}_{P,0}(f) \\ & + \kappa_T(t)e^{2\pi i f \tau_T(t)} \tilde{F}_T(f) \tilde{A}_{T,0}(f)] \exp[-2\pi i f \tau_A], \end{aligned} \quad (2.4.1)$$

where $\tilde{A}_{j,0}(f)$ represents the frequency response of the j -stage actuator for $j \in \{T, P, U\}$. $\kappa_j(t)$ encodes the time-dependence of the strength of the j -stage actuator, and $\tau_j(t)$ represents the variable computational time advance associated with the j -stage actuator,

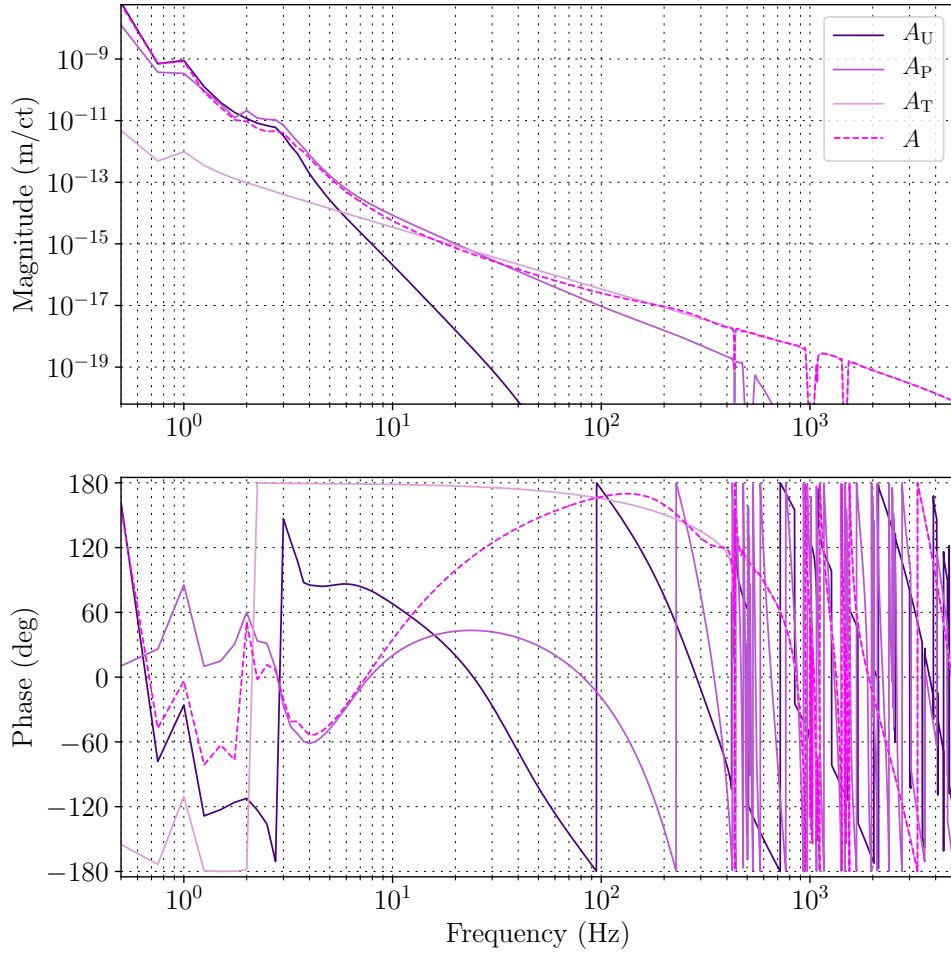


Figure 7 : A Bode plot of the actuation function model for the L1 detector before O3. Measurements used to produce this model were taken on 2019-01-17.

generally expected to be close to zero [17]. The digital filter functions $F_j(f)$ are used before each actuator to distribute the frequency content of d_{ctrl} to each stage. τ_A is a constant computational time delay. Fig. 7 shows a Bode plot of the actuation function for the L1 detector shortly before O3, with each stage of actuation shown individually. The same model is used in Fig. 14.

2.5 Measurements

Calibration of Advanced LIGO data requires a fundamental reference for absolute displacement calibration in order to take measurements of the detectors. This is provided

by a radiation pressure actuator located at each end station known as a photon calibrator (Pcal). The Pcal is an auxiliary laser system that induces fiducial test mass displacements via radiation pressure with force coefficients derived from laser power measurements traceable to SI units. The powers of these laser beams that reflect from the test mass surfaces are measured using calibrated sensors, thus providing continuous absolute calibration when the interferometers are operating in their nominal configurations. The overall $1\text{-}\sigma$ uncertainty in the displacements induced by photon calibrators was 0.75% during O2 [18] with the long-term stability of the calibrated length variations verified during year-long observing runs [19]. Further reduction of the $1\text{-}\sigma$ uncertainty in the displacements induced by the Pcal is possible and expected to occur during O3. The Pcal signals are injected at the same location in the DARM feedback loop as free DARM motion ΔL_{free} , as shown in Fig. 5.

Full measurements of the sensing and actuation functions are achieved using swept sine injections made using the Pcal and each stage of the actuation system [20]. The parameters of the analytical models for A and C are then fit to these measurements to inform a static reference model, denoted by A^{model} and C^{model} . All time-dependent parameters are set to their nominal values in the static reference model, i.e., $\kappa_C \rightarrow 1$, $f_{\text{cc}} \rightarrow f_{\text{cc}}^{\text{model}}$, $f_s \rightarrow f_s^{\text{model}}$, $Q \rightarrow Q^{\text{model}}$, $\kappa_T \rightarrow 1$, $\tau_T \rightarrow 0$, $\kappa_P \rightarrow 1$, $\tau_P \rightarrow 0$, $\kappa_U \rightarrow 1$, $\tau_U \rightarrow 0$, reducing the models for C and A to

$$\tilde{C}^{\text{model}}(f) = \left(\frac{H_C}{1 + if/f_{\text{cc}}^{\text{model}}} \right) \left(\frac{f^2}{f^2 + (f_s^{\text{model}})^2 - if f_s^{\text{model}}/Q^{\text{model}}} \right) C_R(f) \exp[-2\pi if\tau_C] \quad (2.5.1)$$

$$\begin{aligned} \tilde{A}^{\text{model}}(f) = & [\tilde{F}_T(f)\tilde{F}_P(f)\tilde{F}_U(f)\tilde{A}_{U,0}(f) + \tilde{F}_T(f)\tilde{F}_P(f)\tilde{A}_{P,0}(f) \\ & + \tilde{F}_T(f)\tilde{A}_{T,0}(f)] \exp[-2\pi if\tau_A]. \end{aligned} \quad (2.5.2)$$

Full measurements are made prior to observing runs and periodically throughout observing runs in order to produce filters for calibration purposes and inform a calibration uncertainty budget, described in [2].

2.6 Temporal variations in the response of the detectors

As implied by Eqs. 2.3.1 and 2.4.1, the calibration models for A and C are known to show small temporal variations [21], captured in the model by the time-dependent correction factors (TDCFs) κ_T , τ_T , κ_P , τ_P , κ_U , τ_U , κ_C , f_{cc} , f_s , and Q . In order to track and compensate for these temporal variations, sinusoidal excitations are continuously injected using a Pcal and each stage of the actuation system. These injections add loud spectral lines to the $h(t)$ spectrum, called calibration lines. The Pcal thus also provide stable references for continuously monitoring temporal variations in the responses of the interferometers. If not compensated for, temporal variations can lead to systematic errors in the calibrated strain data as large as $\sim 20\%$ at some frequencies. The largest variations are observed in the optical gain and the strength of the electrostatic actuator at the test mass stage of the actuation, tracked by the parameters κ_C and κ_T , respectively. Changes in the optical gain can be caused by drifts in the alignment of the mirrors or intentional changes to the input laser power, and can occur on timescales of several minutes. The strength of the electrostatic actuator gradually increases during normal detector operation on timescales of days to weeks due to the slow accumulation of charge on the test mass. The methods used to track and compensate for slow changes in the TDCFs are described in detail in Chapter 5.

2.7 Calibration pipelines

Low-latency calibration of Advanced LIGO data is done in two stages. The first, called the front-end calibration pipeline, is performed on the same computers that operate the detector's feedback control system. The front-end calibration pipeline uses infinite impulse response (IIR) filters and is run using real-time code in the front-end system where all operations are done on $61 \mu\text{s}$ digital sampling intervals. An advantage of the front-end calibration pipeline is being directly hooked into all of the other front-end computer systems, allowing seamless access to all of the appropriate detector models and parameters. This enables the calibration model to remain up-to-date and in-sync

with the detector. For this reason, it is a long-term goal to perform the low-latency calibration procedure entirely in the front end. However, several limitations to calibration accuracy in the current front-end calibration pipeline necessitate the second stage of the low-latency calibration procedure. First, due to the real-time nature of the front-end computing system, a phase advance cannot be applied to the output, leading to several cycles of delay in the output. Second, it is difficult using IIR filters to model arbitrary transfer functions, as is needed to apply the models of A and C^{-1} to the raw data. This is especially true at high frequencies, due to poles in the calibration models above the Nyquist frequency used to model the response of analog electronics. Finally, although it is now possible to compensate for time dependence in the front-end calibration pipeline, the TDCF's computed in the front end are subject to large noisy fluctuations. Compensation for time dependence is expected to improve front-end calibration accuracy during O3, but due to these large fluctuations, the second stage of the low-latency calibration procedure performs its own calculation of the TDCF's to compensate for time dependence.

Due to the systematic errors currently present in the front-end calibration, its calibrated output is sent to another pipeline called the `gstlal` calibration pipeline. The low-latency `gstlal` calibration pipeline receives as inputs the front-end outputs ΔL_{res} , ΔL_{T} , ΔL_{P} , and ΔL_{U} and applies finite impulse response (FIR) filters to correct the known systematic errors present due to the limitations of the front end's IIR filters. It is much easier using FIR filters to model an arbitrary transfer function, making the task of applying corrections to the front-end models for A and C^{-1} almost trivial. Additionally, the FIR filters of the `gstlal` calibration pipeline are used to high-pass filter the $h(t)$ data for the benefit of downstream analysis. The TDCF's computed in the `gstlal` calibration pipeline are accepted or rejected based on the coherence of the calibration lines and passed through a running median to avoid the large noisy fluctuations seen in the front end's values. Although a similar method has recently been implemented in the front end, not all of these noisy fluctuations have been removed.

In high latency, the entire calibration procedure is done using the `gstlal` calibration pipeline, using as inputs d_{err} and d_{ctrl} . A high latency calibration is generally necessary

due to mistakes made in the low latency calibration, and errors in or improvements to the calibration models and input data discovered after the low-latency calibration is produced.

The methods and improvements to the calibration procedure discussed in the following chapters were developed in the `gst1a1` calibration pipeline.

Chapter 3

The `gstlal` calibration pipeline

The `gstlal` calibration pipeline forms the second stage of the low-latency calibration procedure, correcting known systematic errors remaining in the front-end calibration. It is also used in high latency for the entire calibration procedure. Unlike the front-end calibration pipeline, the `gstlal` calibration pipeline is run on separate machines outside of the front end, and it uses FIR filters instead of IIR filters to apply the calibration model to the input data. The primary advantage of using FIR filters is that an FIR filter can be designed to implement virtually any frequency-domain model. Additionally, FIR filters make it possible to fulfill the requirement that all output must be independent of the start time of the pipeline. The output of an FIR filter depends on a fixed finite number of input samples, while the impact of an input sample to an IIR filter typically decays over time, but does not disappear completely.

3.1 Use of GStreamer and `gstlal` in calibration

Advanced LIGO strain data is processed and stored as double-precision floating-point numbers sampled at 16384 Hz and contains potentially useful information from 10 Hz to 8192 Hz. This range of frequency overlaps significantly with the human hearing range of 20 Hz to 20 kHz. Because of this similarity, it is possible to take advantage of software that is developed for the purpose of processing audio signals. The `gstlal` calibration pipeline uses the open-source audio and video streaming software package

`GStreamer` [22], provided under the GNU license [23]. `GStreamer` is a pipeline-based multimedia framework written in C, and uses a type system based on `GObject` [24] and `GLib` [25]. `GStreamer` provides bindings for Python, allowing pipelines such as the `gstlal` calibration pipeline to be constructed in Python. The `GStreamer` package used for calibration is called `gstlal-calibration` [26], and is a part of the `GstLAL` project [27], which wraps LIGO Algorithm Library (LAL) software [28] with `GStreamer`. The obvious advantages of using `GStreamer` are the many built-in features for low-latency streaming of audio-like data. A disadvantage is that, since `GStreamer` is not primarily designed to process LIGO data, some software package updates cause problems in the `gstlal` calibration pipeline that can require urgent bug fixes. The development of many customized `GStreamer` elements written for the purpose of calibration has improved the `gstlal` calibration pipeline's immunity to such problems.

3.2 Operation procedures in the `gstlal` calibration pipeline

Although significant differences between low-latency and high-latency calibration procedures are noted in Sections 3.3 and 3.4, similarities in the procedures allow for a general description, given below.

3.2.1 Filling in missing raw data

For various reasons, and especially in low latency, raw data is occasionally missing as input to the `gstlal` calibration pipeline. The frequency of raw data dropouts and the amount of missing data varies greatly, but most of the time these dropouts occur at a frequency of a few times per week and last only a few seconds. On rare occasions however, hours of raw data can be dropped. These are generally much less common when the detector is in a nominal low-noise configuration, but occasionally occur then as well. Since downstream data analyses rely on a continuous $h(t)$ data stream, it is essential that the `gstlal` calibration pipeline fills in this missing data. In most channels, these are filled in with zeros. The only exceptions are the channels that report uncertainty

in the calibration lines described in Section 5.2.7, which are filled in with ones.¹ The impact of these dropouts on calibration latency can be seen in Fig. 11, where a ~ 20 -minute stretch of low-noise data is impacted by frequent short dropouts. It is a priority to address this latency during O3, especially since, after a long stretch of missing raw data, it can take the `gstlal` calibration pipeline a considerable time to “catch up” to normal latency levels as it furiously calibrates worthless fake data. One possible method to prevent these occasional large increases in latency would be to track the time since raw data has arrived in the `gstlal` calibration pipeline. Anytime the pipeline has waited longer than some chosen threshold, it could begin filling in the missing data. This would prevent the pipeline from falling behind, providing a more consistent $h(t)$ time series for downstream analysis and saving the time currently needed to catch up after a long data dropout.

3.2.2 Computing the time-dependent correction factors

Despite the fact that the front-end calibration pipeline computes the TDCFs, the `gstlal` calibration pipeline computes and utilizes the TDCFs independently. This is due in part to the fact that the noise attenuation process described in Section 5.2.7 has not yet been fully developed and tested in the front-end calibration pipeline, and to the fact that the `gstlal` calibration pipeline also needs to compute the TDCFs in high latency. It additionally allows results to be compared between the front end and the `gstlal` calibration pipeline. The calculation of the TDCFs in the `gstlal` calibration pipeline begins with measurement of the calibration lines, accomplished using demodulation as described in Section 5.2.1. The data is downsampled to 16 Hz in this process before the TDCFs are computed, preventing unmanageable computational cost. The subsequent calculation of the TDCFs is described in detail in Section 5.2.

¹These channels are used to determine when to gate the calculation of the TDCFs, and a value of zero during a data dropout would falsely indicate that the calculation of the TDCFs is reliable.

3.2.3 Applying FIR filters to compute $h(t)$

The `gst1a1` calibration pipeline applies time-domain FIR filters modeling the actuation function \tilde{A} at each stage, described by Eq. 2.4.1, and the inverse sensing function \tilde{C}^{-1} , described by Eq. 2.3.1, to the actuation and inverse sensing paths separately, before adding the components to produce $\Delta L_{\text{free}}(t)$. During O2, the scalar correction factors κ_T and κ_C , as well as the factor κ_{PU} (estimate of the combined impact of κ_P and κ_U) were applied as multiplicative factors to the components of ΔL_{free} after the static model filters were applied:

$$h(t) = \frac{1}{L} \left(\frac{1}{\kappa_C(t)} C^{-1, \text{model}} * d_{\text{err}}(t) + \kappa_T(t) A_T^{\text{model}} * d_{\text{ctrl}}(t) + \kappa_{\text{PU}}(t) A_{\text{PU}}^{\text{model}} * d_{\text{ctrl}}(t) \right). \quad (3.2.1)$$

During O3, it will be possible to use adaptive filtering techniques to apply time-dependent filters accounting for all parameterized time dependence in the `gst1a1` calibration pipeline, as described in detail in Section 5.3.2, the result being

$$h(t) = \frac{1}{L} (C^{-1}(t) * d_{\text{err}}(t) + A_T(t) * d_{\text{ctrl}}(t) + A_P(t) * d_{\text{ctrl}}(t) + A_U(t) * d_{\text{ctrl}}(t)). \quad (3.2.2)$$

3.2.4 The calibration state vector

The `gst1a1` calibration pipeline computes a bitwise state vector using 32-bit unsigned integers sampled at 16 Hz. The calibration state vector contains information about the integrity of the $h(t)$ data product at each moment of time, as well as additional information about the state of the calibration. Definitions of each bit in the O3 calibration state vector are shown in Table 1. Bit 0 indicates that the $h(t)$ data currently produced is accurate and suitable for analysis. It is computed as the logical AND of bits 2, 3, and 4, plus any of bits 9 through 15 corresponding to a time-dependent correction that is being compensated for in $h(t)$. Bits 1 and 2 are read in from the Guardian, a front-end platform consisting of distributed, independent, state machine automation nodes organized hierarchically for full detector control [29]. Bit 1 tells whether the operator in the control room has determined that there are no ongoing commissioning activities and

Table 1 : A summary of the meaning of each bit in the calibration state vector during O3.

bit	Short descriptor	Long descriptor
0	HOFT_OK	$h(t)$ was successfully computed
1	OBS_INTENT	interferometer is in “observation intent” mode
2	OBS_READY	interferometer is in “observation ready” mode
3	FILTERS_OK	calibration filters settled in
4	NO_GAP	Input data is present and no underflows or overflows
5	NO_STOCH_HW_INJ	No stochastic hardware injections present
6	NO_CBC_HW_INJ	No compact binary coalescence hardware injections present
7	NO_BURST_HW_INJ	No burst hardware injections present
8	NO_DETCHAR_HW_INJ	No detector characterization hardware injections present
9	KAPPA_T_SMOOTH_OK	κ_T output is in expected range
10	KAPPA_P_SMOOTH_OK	κ_P output is in expected range
11	KAPPA_U_SMOOTH_OK	κ_U output is in expected range
12	KAPPA_C_SMOOTH_OK	κ_C output is in expected range
13	F_CC_SMOOTH_OK	f_{cc} output is in expected range
14	F_S_SMOOTH_OK	f_s output is in expected range
15	Q_INV_SMOOTH_OK	Q^{-1} of SRC output is in expected range
16	SUS_LINE3_COH_OK	Coherence of test actuator line is acceptable
17	SUS_LINE2_COH_OK	Coherence of penultimate actuator line is acceptable
18	SUS_LINE1_COH_OK	Coherence of upper intermediate actuator line is acceptable
19	PCALY_LINE1_COH_OK	Coherence for first Pcal line is acceptable
20	PCALY_LINE2_COH_OK	Coherence for second Pcal line is acceptable
21	PCALY_LINE4_COH_OK	Coherence for lowest Pcal line is acceptable
22	D_EPICS_MATCH	TDCF reference factors for digital filter D agree
23	A_EPICS_MATCH	TDCF reference factors for actuation function A agree
24	C_EPICS_MATCH	TDCF reference factors for sensing function C agree
25	MISC_EPICS_MATCH	Miscellaneous TDCF reference factors match
26	LINE_SUBTRACTION_OK	Subtraction of calibration lines is working
27	NOISE_SUBTRACTION_OK	Subtraction of broadband noise is working
28	NOISE_SUBTRACTION_GATE	Transfer function calculation is not being gated

the data being produced is science-quality. Bit 2 indicates that the detector is in a nominal low-noise configuration. Bit 3 indicates that the calibration filters have settled, that is,

all of the input data filtered to produce the current output samples is low-noise data that does not include any data dropouts. Bit 4 indicates that there are no raw data dropouts or arithmetic underflow or overflow inputs to the pipeline. Bits 5 through 8 indicate that there are no hardware injections present in the current $h(t)$ data. Bits 9 through 15 indicate that the computed TDCF's are within an expected range. Bits 16 through 21 indicate that the coherence of the calibration lines between the injection channels and the error signal are acceptable based on a predetermined threshold, as described in Section 5.2.7. Bits 22 through 25 indicate that the two sets of reference model values used to compute the TDCF's agree, one in the front end and the other in the filters file read in by the `gstlal` calibration pipeline. The front-end reference model values are used in low latency, while the values stored in the filters file are used in high latency. Bits 26 and 27 indicate that subtraction of spectral lines and noise is successfully reducing the RMS of the strain signal in the frequency bands where the impact is expected to be significant. Bit 28 indicates that the calculation of transfer functions used for broadband noise subtraction is running, and not being halted due to increased levels of detector noise. The spectral line and noise subtraction is described in detail in Chapter 6.

3.3 The low-latency `gstlal` calibration pipeline

The low-latency `gstlal` calibration pipeline, also called the GDS (global diagnostic system) calibration pipeline, is run on a machine at the detector sites called a data monitoring tool (DMT). The DMTs receive raw data in very low latency from a frame broadcaster. The raw data is written to a shared memory partition where it is read in by the `gstlal` calibration pipeline. Calibrated GW frames are then written to another shared memory partition to be sent to downstream processes and distributed.

The primary purpose of the low-latency `gstlal` calibration pipeline is to correct systematic errors remaining after the IIR filtering done in the front end. This is especially impactful at high frequencies, due to the presence of poles above the Nyquist rate that are difficult to model using IIR filters, and the current inability to apply a phase advance in

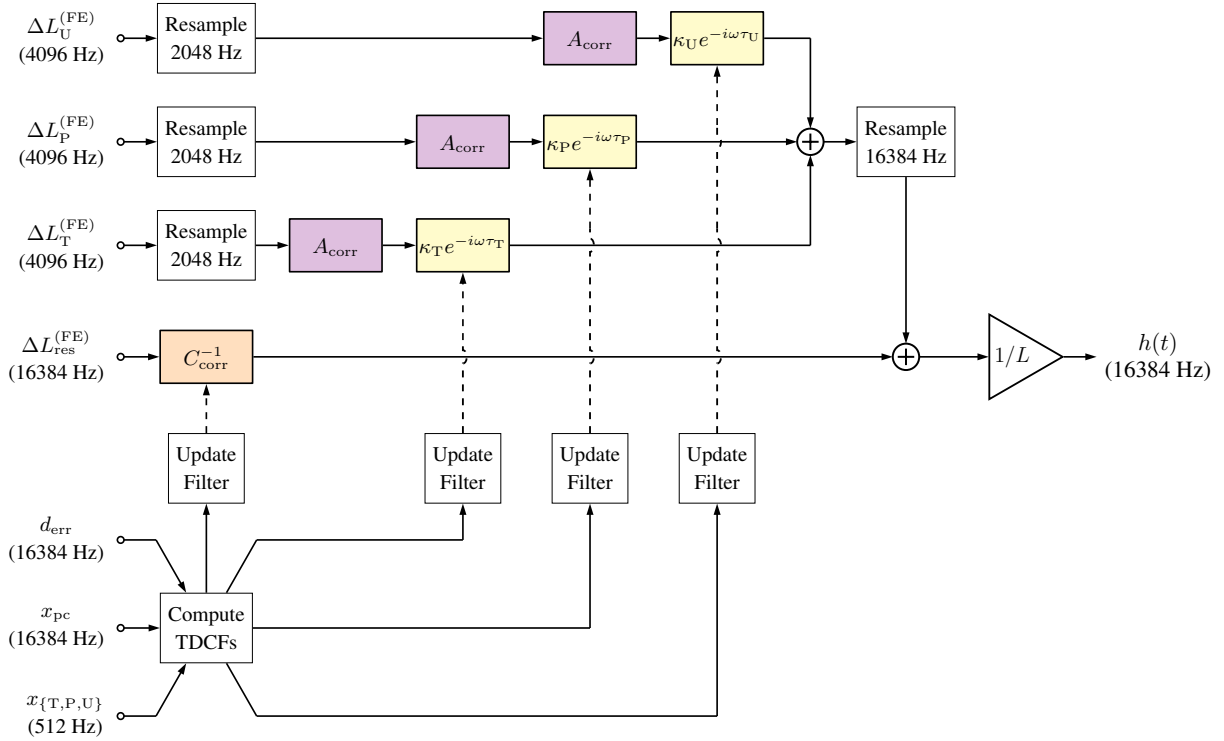


Figure 8 : A simplified block diagram showing the workflow of the low-latency `gst1a1` calibration pipeline. It receives as inputs the calibrated components of ΔL_{free} computed by the front-end calibration pipeline and applies the FIR filters A_{corr} and C_{corr}^{-1} to correct known systematic errors. Solid lines represent the continuous flow of digital time-series data, while the dashed lines represent the periodic passing of new FIR filters from elements that compute them to elements that use them to filter input data. Details of the calculation of the TDCF's and the calibration state vector are not shown. Fig. 23 shows the broadband noise subtraction in the `gst1a1` calibration pipeline.

the real-time code of the front-end computing system. Additionally, the `gst1a1` calibration pipeline computes and compensates for the TDCF's, improving calibration accuracy by up to 20% in the detection band. The front-end calibration pipeline is also capable of tracking and compensating for the TDCF's, but the `gst1a1` calibration pipeline does not currently read in the TDCF-compensated channels from the front end, mainly due to the fact that more development and testing is needed in the attenuation of noise in the front-end TDCF's. Fig. 8 is a block diagram showing the workflow of the low-latency `gst1a1` calibration pipeline.

Due to the front-end calibration pipeline's easy access to detector state information and the ability to make changes to calibration parameters quickly, it is a long-term goal to move more of the low-latency calibration procedure into the front end. However, as of

the beginning of O3, there is still much to be done in the `gstlal` calibration pipeline in low latency.

3.4 The high-latency `gstlal` calibration pipeline

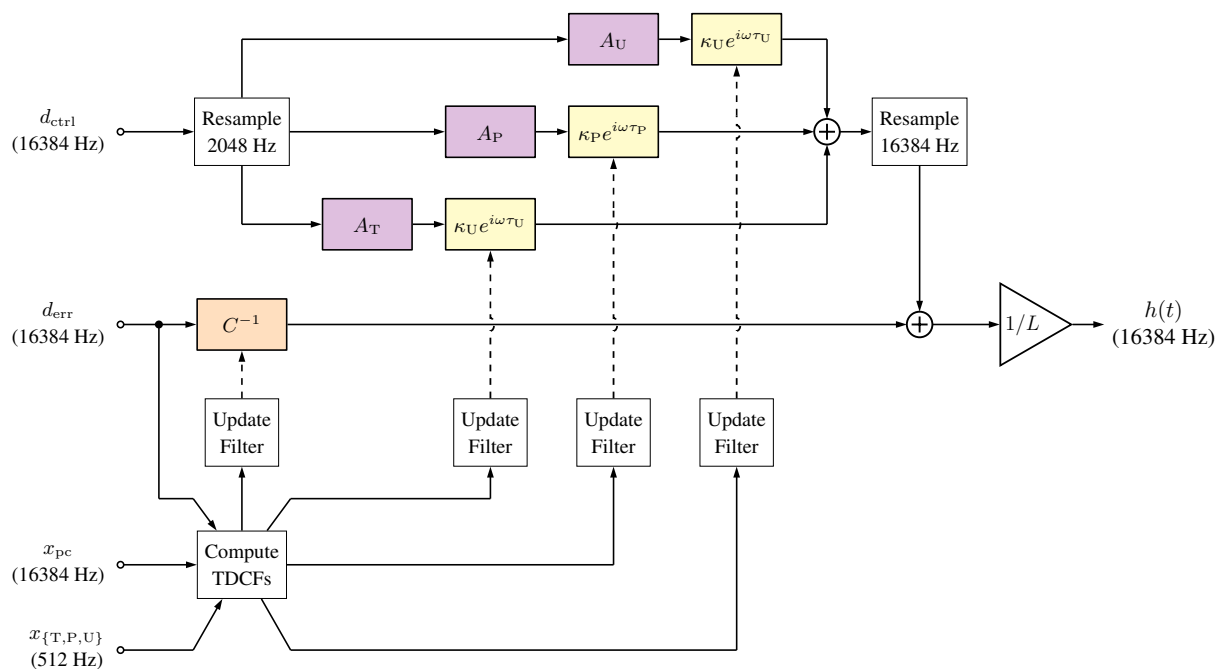


Figure 9 : A simplified block diagram showing the workflow of the high-latency `gstlal` calibration pipeline. It applies FIR filters to the error signal d_{err} and control signal d_{ctrl} to produce calibrated strain data. Solid lines represent the continuous flow of digital time-series data, while the dashed lines represent the periodic passing of new FIR filters from elements that compute them to elements that use them to filter input data. Details of the calculation of the TDCFs and the calibration state vector are not shown. Fig. 23 shows the broadband noise subtraction in the `gstlal` calibration pipeline.

The high-latency calibration pipeline, also called the DCS (data and computing systems) calibration pipeline, is run using many 4096-second jobs in parallel on the LIGO Data Grid computing cluster at the California Institute of Technology [30]. The raw data is read from raw GW frame files, each containing 64 s of raw data, and calibrated data is then written to another set of GW frame files, each with 4096 s of calibrated data. In high latency, the entire calibration procedure is done in the `gstlal` calibration pipeline, using as inputs the error and control signals, d_{err} and d_{ctrl} . The full time-dependent inverse sensing and actuation functions are applied as FIR filters to d_{err} and d_{ctrl} to produce

the calibrated strain product. Fig. 9 is a block diagram showing the workflow of the high-latency `gstlal` calibration pipeline.

Chapter 4

Designing digital filters for calibration

4.1 Principles of making FIR filters

In order to understand the design of the digital FIR filters produced and used to calibrate Advanced LIGO data and the recent improvements that have been made to the design methods, a basic working knowledge of the principles of FIR filters is necessary. A digital FIR filter is an array of numbers, called filter coefficients, that is applied to inputs using convolution, according to Eq. 2.2.2

4.1.1 The ideal low- and high-pass filters

We begin by considering the low-pass filter, a filter designed to remove the content of a signal below a chosen cutoff frequency while leaving the higher-frequency content unchanged. We define the ideal low-pass filter as the solution for $\mathcal{F}_{lp}(f_{cut}; \tau)$ in the equation

$$\int_{-\infty}^{\infty} \mathcal{F}_{lp}(f_{cut}; \tau) \cos [2\pi f(t - \tau) - \phi] d\tau = \begin{cases} \cos(2\pi ft - \phi), & f < f_{cut} \\ \frac{1}{2} \cos(2\pi ft - \phi), & f = f_{cut} \\ 0, & f > f_{cut} \end{cases} \quad (4.1.1)$$

The solution, called a sinc function, is

$$\mathcal{F}_{\text{lp}}(f_{\text{cut}}; \tau) = f_{\text{cut}} \text{sinc}(f_{\text{cut}} \tau) \quad (4.1.2)$$

where

$$\text{sinc}(x) = \begin{cases} \frac{\sin(\pi x)}{\pi x}, & x \neq 0 \\ 1, & x = 0 \end{cases} \quad (4.1.3)$$

The filter $\mathcal{F}_{\text{lp}}(f_{\text{cut}}; \tau)$ is a perfect low-pass filter of infinite length with cutoff frequency f_{cut} , defined for continuous input data. In order to use this solution as a digital FIR filter, the length must be made finite using a point-by-point multiplication with some chosen window function. Then, a new normalization must be applied to the filter by dividing the filter coefficients by the digital sample rate of the input data.

A low-pass filter can be used to produce a high-pass filter whose quality depends on the quality of the original low-pass filter, using a technique called spectral inversion. To see this, imagine that we wish to simulate the effect of a high-pass filter by applying a low-pass filter to a data set, and then subtracting the low-pass filtered data from the original data set. This would remove only low frequencies, leaving frequencies above the cutoff frequency of the low-pass filter unperturbed. The same can be accomplished by negating each coefficient of a low-pass filter and adding one to the “central” filter coefficient (i.e., the coefficient which multiplies input samples that have timestamps equal to the current output sample).

Construction of band-pass or band-stop filters can also be accomplished through convolution of any desired combination of low-pass and high-pass filters. The length of the resulting filter in taps is the sum of the lengths of the original filters minus the number of convolutions.

4.1.2 Applying time-domain window functions to filters

A pivotal choice that must often be made in the construction of a digital FIR filter is how to window the filter in the time domain. It is tempting to assume that a window function should alter the shape of the FIR filter as little as possible while avoiding edge

effects. However, choices made under this assumption often lead to spectral leakage and an ineffective attenuation beyond cutoff frequencies. Since we wish to control the frequency response of the filter, it is useful to consider the effect of window functions in the frequency domain. Applying a window to a filter in the time domain entails a point-by-point multiplication, which is a convolution when represented in the frequency domain. The goal then is to determine what type of function should be convolved with the filter in the frequency domain. Before the application of the window, the filter can be thought of as infinite in length and ideal in its frequency response. Ideally, we would like to choose a window with a Fourier transform that looks like a Dirac delta function. However, windows are finite in length and so cannot exactly replicate a Dirac delta function. Appropriate choices must therefore be made based on the input data and the priorities for the frequency response of the filter being designed.

4.1.3 Resampling of time-series data

As shown in Figs. 8, 9, and 23, time series data is frequently resampled in the `gstlal` calibration pipeline. This is a necessity for the actuation path, since the FIR filters applied there are longer and need more aggressive high-pass filtering, and filtering at the full $h(t)$ sample rate of 16384 Hz would lead to unmanageable computational cost. Resampling is also important when demodulating the error signal and the injection channels needed to compute the TDCFs. In order to accomplish these tasks with manageable computational cost, acceptable calibration accuracy, and minimal noise in the TDCFs, a very efficient resampling algorithm with effective anti-aliasing and anti-imaging is crucial.

The resampling algorithm in the `gstlal` calibration pipeline has a quality setting that can be adjusted based on the unique needs of each process. For the simplest cases, data is downsampled by choosing every n^{th} sample or upsampled by copying each sample n times, where n is the ratio of sample rates. For processes that need slightly higher quality, data can be downsampled by averaging n samples or upsampled using linear extrapolation or a cubic spline. For processes that demand high quality, a windowed sinc table is used to filter inputs. When downsampling, the sinc table acts as an anti-aliasing

filter that needs to be applied only once for every n inputs, and is shifted by n inputs after the production of each consecutive output sample. When upsampling, the same sinc table acts as an anti-imaging filter sampled at the output sample rate. When applied to inputs to produce an output sample, only every n^{th} tap is used on an input sample. To compute the next sample, the sinc table is shifted relative to the inputs by one tap. This combination of anti-aliasing and anti-imaging with the resampling process is essential to achieve the desired quality of calibrated data with manageable computational cost.

The anti-aliasing filter used in the downsampling to 16 Hz done during demodulation of the calibration lines is ~ 12 s in length. Prior to the development of the current resampling algorithm, this contributed 6 s of calibration latency. Additionally, the TDCFs were upsampled to 16384 Hz using an anti-imaging filter that was also ~ 12 s in length. For this reason, the intrinsic latency of the `gst1a1` calibration pipeline was ~ 12 s during the early portion of O2. Since temporal variations in the TDCFs are slow compared to this timescale, this latency was removed by the addition of an option in the resampling algorithm that allows the timestamps of output samples to be shifted so as to achieve a zero-latency filter. This shift in timestamps is small compared to the shift in timestamps associated with the causal 20-second low-pass demodulation filter, the 128-second running median, and the 10-second running mean applied to the TDCFs. With this latency removed, the highest latency process in the `gst1a1` calibration pipeline is the application of the actuation filter. The resulting improvement in latency is shown in Fig. 11.

4.2 Designing FIR filters to model the inverse sensing and actuation functions

The calibration models for A and C^{-1} that the FIR filters are designed to implement are constructed in the frequency domain as described in Sections 2.3 and 2.4. The steps currently used to produce FIR filters based on the models of A and C^{-1} are similar to those described in [16], but are detailed here due to recent minor modifications and for completeness:

1. *High-pass filter.* Seismic noise in the raw data channels is too high at low frequencies to measure any GW signals, and the digital system has finite dynamic range. Low frequencies are therefore rolled off by multiplying the frequency components from 4.5 Hz to 9 Hz by half of a Hann window raised to the fourth power.
2. *Low-pass filter in the sensing path.* Since the inverse sensing function tends toward infinity at high frequencies, a low-pass filter is applied to the inverse sensing function to roll off high frequencies ($f \gtrsim 6$ kHz) smoothly, in addition to the the anti-aliasing in the front end. This is done by multiplying the high frequency components by half of a Hann window.
3. *Artificial delay.* An artificial delay is added to the FIR filter that is equal to half of the length of the filter. This delay is undone within the `gstlal` calibration pipeline by advancing the filter output by the same number of samples. The reason for the delay is to center the FIR filter in time, avoiding edge effects while filtering and making the filter non-causal, with output depending on both past and future inputs. The non-causal nature of the filters is necessary for physical reasons as well. The response of the detector to GWs is causal since the detector is a physical system. Therefore, when this response is inverted in the calibration to compute the GW signal from data in the error signal, the resulting filter is necessarily non-causal.
4. *Inverse Fourier transform.* The inverse Fourier transform is computed to obtain the time-domain FIR filter.
5. *Time-domain window function.* A window function is applied to the resulting time-domain FIR filter to ensure that the model and high-pass filter are well-represented by the filter. Small systematic errors can be induced by the application of the window. If necessary, these can be corrected by measuring the deviation of the filter's response from the frequency-domain model and compensating for this in the frequency-domain model before the above steps. During O3, this is being done in the actuation filters in the high-latency calibration to correct $\sim 1\%$ systematic errors below ~ 20 Hz, which are likely caused by the steep increase in the magnitude of the

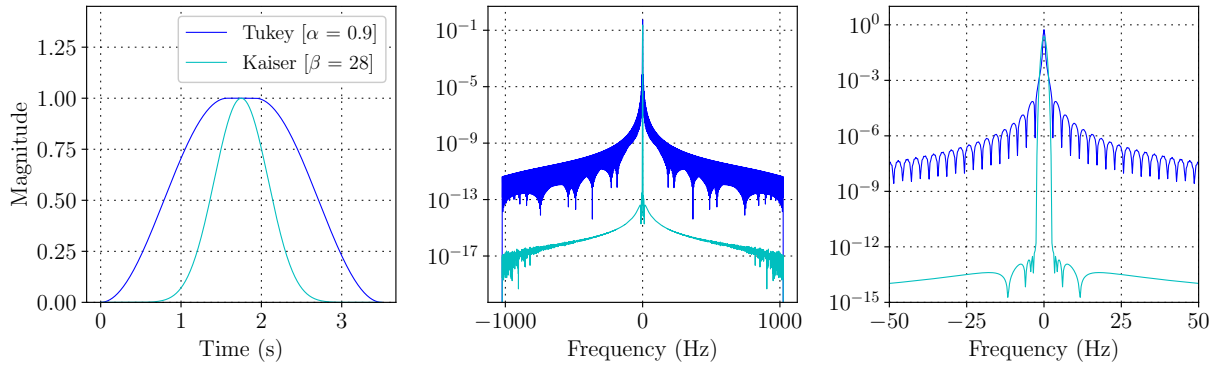


Figure 10 : A comparison of a 3.5-s Tukey window with $\alpha = 0.9$ to a 3.5-s Kaiser window with $\beta = 28$. The plot on the left shows the windows in the time domain, while the center plot shows the Fourier transform. The plot on the right is a zoomed-in view, showing the difference in the Fourier transform. The much steeper drop in the Kaiser window from the main lobe leads to a dramatic improvement in the high-pass filtering in the calibration filters.

actuation function at low frequencies and the width of the main lobe in the Fourier transform of the Kaiser window that is used (see Fig. 10).

4.2.1 Attenuating low-frequency noise with minimal latency

A frequent request from downstream data analysts during O2 was to improve the quality of the high-pass filtering done in the `gstlal` calibration pipeline. Increasing the length of the FIR filters is one way to improve the attenuation of low frequency noise, but it also adds unwanted latency to the low-latency $h(t)$ data and increases the computational cost of running the pipeline. Moreover, a high-priority goal of O3 calibration is to reduce the calibration latency, which originates primarily from length of the actuation filters. It is a challenging task to improve the high-pass filtering without increasing latency, or to reduce the latency without degrading the quality of the high-pass filtering. One recent improvement in both high-pass filtering and calibration latency was accomplished with a more careful choice of window function to apply to the time-domain FIR filters. During O2, a Tukey window was used with $\alpha = 0.9$ for the last step in the procedure above for

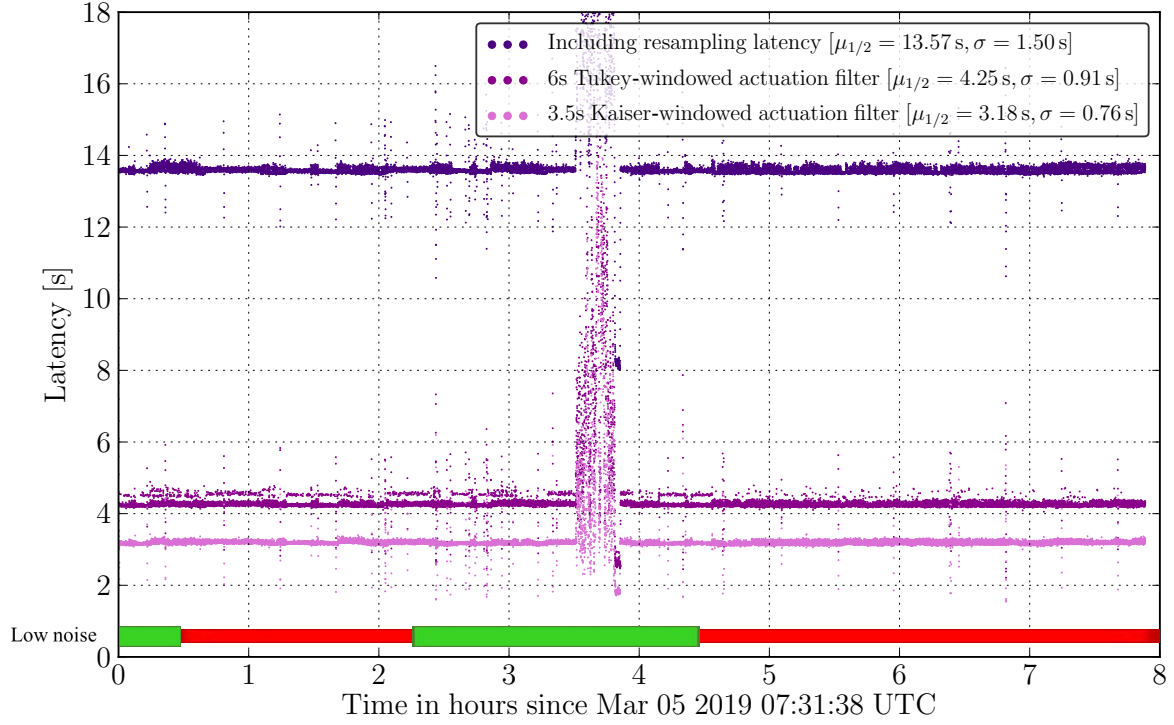


Figure 11 : Time series of calibration latencies at L1, showing two significant improvements made since the beginning of O2. Each point was computed by measuring the difference in the times when output data files exit the `gstlal` calibration pipeline and when input data files with the same timestamp enter the pipeline. The time shown includes times when the detector is in low-noise state (green) and times when it is not (red), as indicated by the bar at the bottom. The median latencies $\mu_{1/2}$ and standard deviations σ are shown for each data set.

making filters. For a window with N samples, this is defined by

$$W_{\text{Tukey}}(n) = \begin{cases} \sin^2\left(\frac{\pi n}{\alpha(N-1)}\right), & 0 \leq n < \alpha \frac{N-1}{2} \\ 1, & \alpha \frac{N-1}{2} \leq n \leq (2-\alpha) \frac{N-1}{2} \\ \cos^2\left(\frac{\pi n}{\alpha(N-1)} - \frac{\pi}{\alpha} + \frac{\pi}{2}\right), & (2-\alpha) \frac{N-1}{2} < n \leq N-1 \end{cases} \quad (4.2.1)$$

This window has recently been replaced with a Kaiser window, which approximates a window function that maximizes the energy concentration in the main lobe of the Fourier transform. The Kaiser window is defined by

$$W_{\text{Kaiser}}(n) = \frac{I_0\left(\beta \sqrt{1 - \left(\frac{2n}{N-1} - 1\right)^2}\right)}{I_0(\beta)}, \quad (4.2.2)$$

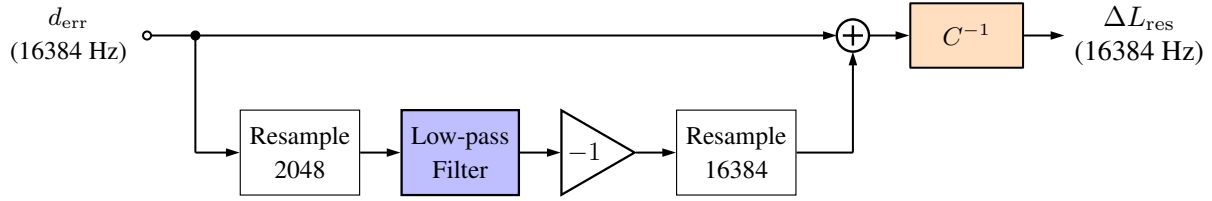


Figure 12 : A block diagram showing a method by which to high-pass filter the inverse sensing path below the full $h(t)$ sample rate without losing any high-frequency information.

where I_0 is the zeroth order modified Bessel function of the first kind. Use of the Kaiser window has dramatically improved the high-pass filtering due to the fact that the magnitude of the Fourier transform quickly drops many orders of magnitude as one moves away from the main lobe. The roll-off of the digital calibration filters below 9 Hz is therefore much steeper using a Kaiser window. The actuation filter has been reduced in length from 6 s to 3.5 s, using $\beta = 28$. The 1-second inverse sensing filter is also windowed with a Kaiser window with $\beta = 10$. Time- and frequency-domain comparisons of the Tukey window to the Kaiser window are shown in Fig. 10. The O2-style filters and the new O3 filters were used to calibrate 8 hours of L1 data prior to O3. The resulting improvement in intrinsic calibration pipeline latency is shown in Fig. 11. This plot was generated using the L1 computing cluster rather than the DMT. The improvement in calibration latency due to the shorter actuation filters is slightly less significant than expected (latency is expected to be less than 3 s), possibly due in part to the fact that numerous other jobs were running at the time of this test. The dramatic increase in latency just before 4 hours is due to raw data drop-outs described in 3.2.1. This is unrelated to the latency caused by the lengths of the filters, but it needs to be addressed. Another plot of calibration latency for H1 data using similar configurations can be seen in Fig. 26.

Although the low-frequency noise in the actuation path is louder than that in the sensing path, attenuating this noise in the sensing path has the additional challenge that the data is filtered at the full $h(t)$ sample rate of 16384 Hz. This is necessary because the error signal d_{err} contains significant signal content up to the Nyquist frequency. The challenge of attenuating this noise therefore arises not due to the need to reduce latency, but due to the computational cost of filtering a 16384-Hz time series with a long FIR

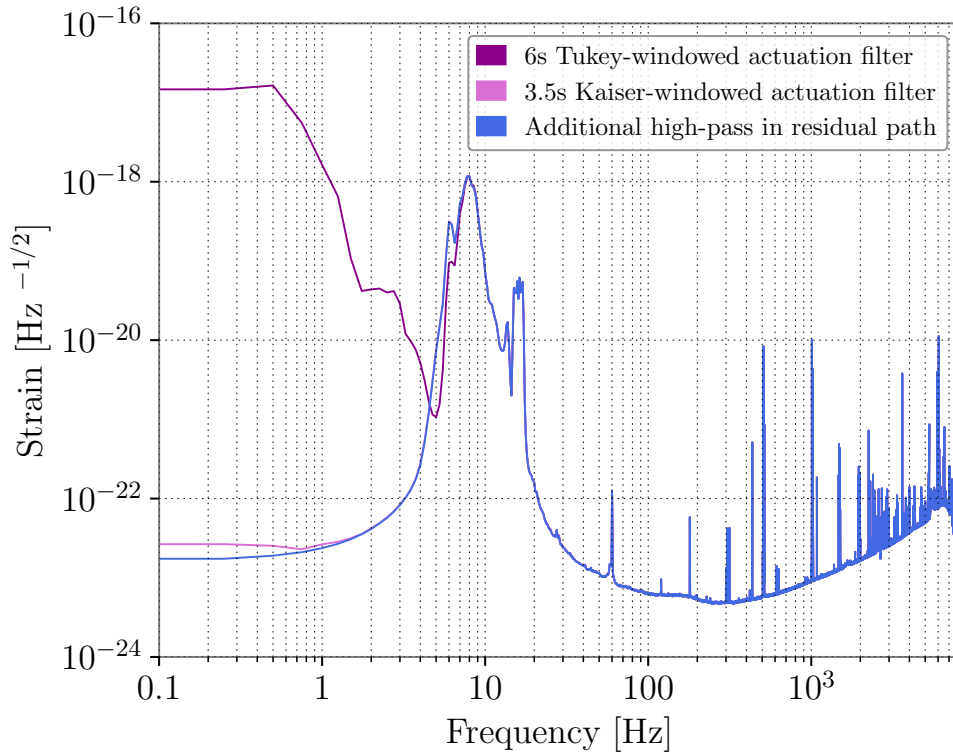


Figure 13 : A comparison of 3 amplitude spectral densities, showing improvements in the high-pass filters used in the `gst1al` calibration pipeline. The improvements are due to the use of a Kaiser window instead of a Tukey window in the filters, as well as the use of an additional high-pass filter in the sensing path.

filter. At times, low-frequency noise in the sensing path dominates the final signal content in $h(t)$ below 10 Hz due to the fact that the actuation filter is 3.5 s in length and the inverse sensing filter is only 1.0 s in length. To attenuate this noise without dramatically increasing computational cost, a method is used to apply a separate high-pass filter to the inverse sensing path at a lower sample rate while still preserving the content of the signal up to the Nyquist rate. The method, depicted in Fig. 12, is to tee the sensing path, downsample one copy to apply a low-pass filter, upsample the low-passed data, and subtract it from the original data before applying the inverse sensing filter. The additional high-pass filter currently has a length of 2.5 s so that the total filtering latency of the sensing path is equal to that of the actuation path, and it is windowed using a Kaiser window with $\beta = 20$. The improvements in low-frequency noise attenuation due to the use of a 3.5-second Kaiser window instead of a 6-second Tukey window in the actuation filter, as well as the inclusion of the additional high-pass filter in the sensing path, are

shown in Fig. 13. Amplitude spectral densities computed from 4096 s of low-noise L1 data taken prior to O3 are plotted, showing an improvement in the stop band of about 6 orders of magnitude over the O2-style filters.

4.2.2 Accuracy of the filters' representation of the response function

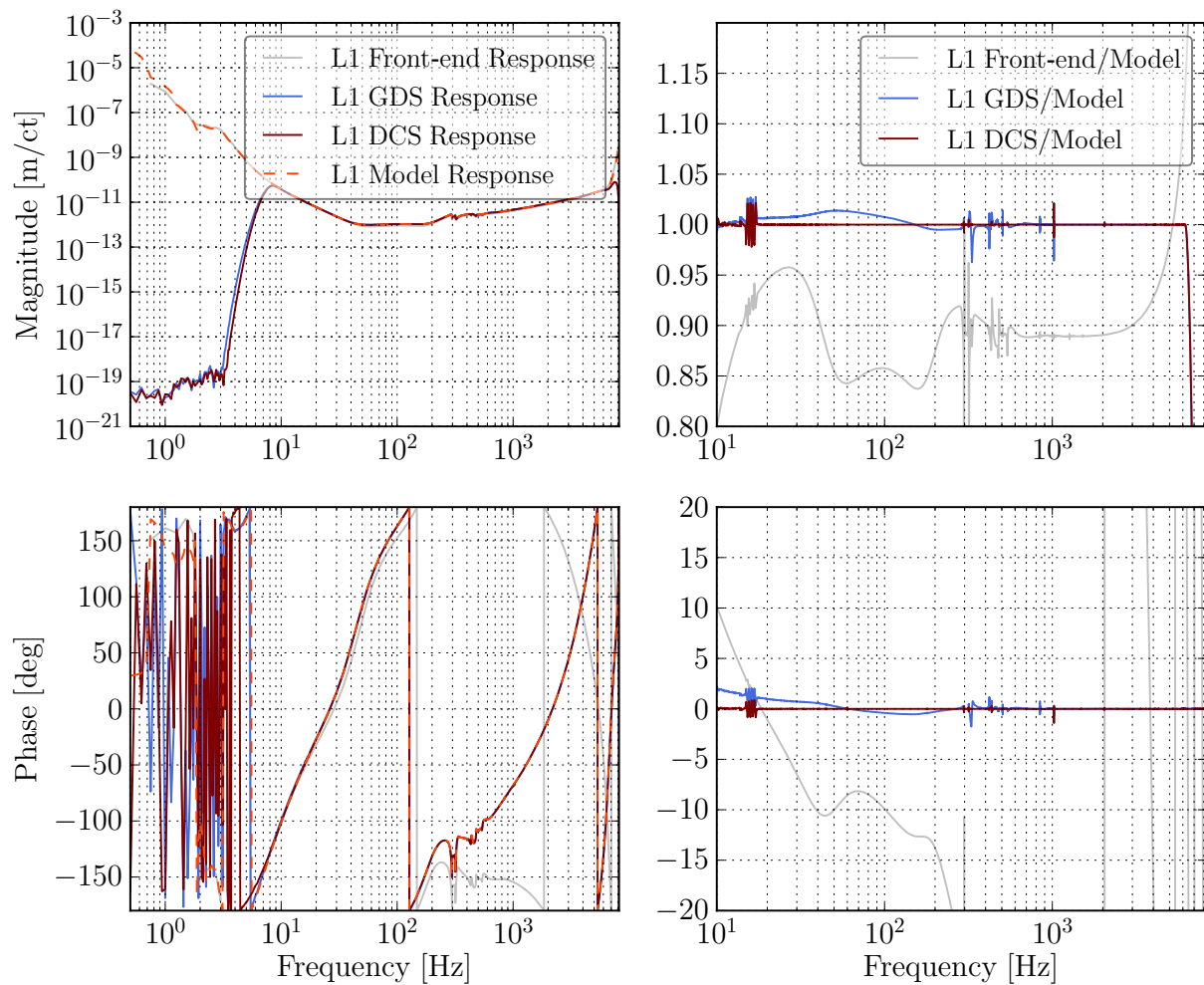


Figure 14 : A comparison of the response of the calibration filters to the frequency-domain modeled response function $\widehat{R}^{\text{model}}(f)$. The transfer function $\widehat{\Delta L}_{\text{free}}(f)/\widehat{d}_{\text{err}}(f)$ was taken using ~ 4500 s of L1 data on March 5, 2019, shortly prior to O3. The front-end calibration filters at this time show more systematic error than is typical. The low-latency `gstlal` calibration data product (GDS) and the high-latency `gstlal` calibration data product (DCS) are shown as well, each showing the expected improvements. The noise in the plots on the right from 15 - 20 Hz is most likely due to the 4 calibration lines in that band.

A useful test to evaluate the accuracy of the filters' application of the time-independent

response function $\tilde{R}^{\text{model}}(f)$ is done by empirically evaluating the transfer function between the error signal $d_{\text{err}}(t)$ and the time series $\Delta L_{\text{free}}(t)$ reconstructed by the calibration pipelines, and comparing this to the frequency-domain model $\tilde{R}^{\text{model}}(f)$. Note that such tests of the accuracy of the filters necessarily do not compensate for any time dependence. Fig. 14 shows such a comparison, using three different calibration products: the front-end calibration data product produced using IIR filters, the low-latency strain data product produced by the combined action of the front end (IIR filters) and the `gst1a1` calibration pipeline (FIR filters), and the high-latency strain data product produced entirely using FIR filters in the `gst1a1` calibration pipeline. The data was taken at L1 from March 5, 2019, prior to O3. Note the $\sim 1\%$ discrepancy below 1 kHz in the low-latency `gst1a1` calibration. This is due to high-frequency poles applied in the actuation in the front-end calibration pipeline but not corrected by the FIR filters in the `gst1a1` calibration pipeline. This discrepancy is not present in high-latency calibrated data. The low-latency $h(t)$ data at H1 also does not show this discrepancy because these poles are not applied in the front-end calibration pipeline at H1. It is a priority to begin correcting this systematic error in the `gst1a1` calibration pipeline during O3.

Chapter 5

Temporal variations in calibration-model parameters

The calibration models for A and C are known to vary slowly in time, having a significant impact on calibration accuracy [21]. While in Initial LIGO the only time-dependent correction applied to the calibration was the gain of the sensing function [15], compensation for temporal variations is more complex in Advanced LIGO. This is due to both the actuation system, which consists of an electrostatic actuator at the test stage and electromagnetic actuators at the next two higher stages, as well as the addition of the SRC. The strength of the electrostatic actuator is of particular interest, as the gradual buildup of charge can cause variations of $\sim 10\%$. During O1 and O2, the strength of the electrostatic actuator was tracked as κ_T , the two upper stages of actuation were tracked with the combined factor κ_{PU} , the gain of the sensing function was tracked with κ_C , and the coupled cavity pole frequency f_{cc} was tracked [16]. During O2, the optical antispring frequency f_s and quality factor Q of the SRC were additionally tracked at H1. It is straightforward to apply corrections for κ_T , κ_{PU} , and κ_C by simply multiplying the appropriate calibrated component of ΔL_{free} . Compensating for the time dependence of the remaining TDCFs requires updating FIR filters while the calibration pipeline is running, due to the fact that each of the remaining TDCFs has a frequency-dependent impact on the components of ΔL_{free} . During the second offline calibration after O2, such a method

was used to compensate for the time dependence of f_{cc} . For O3, infrastructure is in place to track and compensate for all parameterized time dependence in the calibration models in both low and high latency. This includes the ten time-dependent parameters in Eqs. 2.3.1 and 2.4.1: κ_C , f_{cc} , f_s , Q , κ_T , τ_T , κ_P , τ_P , κ_U , and τ_U [17].

Changes in the optical gain of the sensing function κ_C occur due to changes in mirror alignment and input laser power to the detectors. These can account for up to $\sim 15\%$ changes in the optical gain occurring on timescales of several minutes. Changes of $\sim \pm 20$ Hz are observed over similar timescales in the coupled cavity pole frequency f_{cc} , whose nominal value is expected to be ~ 400 Hz during O3. The optical antispring frequency of the SRC (generally $\lesssim 10$ Hz) is seen to fluctuate by ~ 2 Hz. The strength of the electrostatic actuator κ_T sees fluctuations of $\sim 10\%$ on timescales of days to weeks, due to the gradual accumulation of charge on the test masses. κ_P and κ_U can change by up to 5% on timescales of weeks. The variable time delays τ_T , τ_P , and τ_U are generally expected to remain negligibly small; however, occasional changes of multiples of $15 \mu\text{s}$ (64 kHz digital sampling time in the front-end computers) were observed during O2 [17]. Even when deviations of the TDCF's from their nominal values are small, the resulting systematic errors in $h(t)$ can be magnified due to the fact that the components of ΔL_{free} which are added together are out of phase at some frequencies.

The following sections describe the methods used by the calibration group, and in particular, the `gstlal` calibration pipeline, to measure, compute, and compensate for time dependence in the calibration. The impact of compensating for time dependence on calibration accuracy is also assessed. In the following sections, let $j, k \in \{\text{T}, \text{P}, \text{U}\}$ be indices labeling the stages of actuation and the associated calibration line frequencies, $\ell \in \{1, 2\}$ be indices labeling Pcal line frequencies, and $n \in \{\text{T}, \text{P}, \text{U}, 1, 2\}$.

5.1 Calibration lines

Frequently taking full measurements of the detectors during observation is impractical due to the loss of observation time and extra effort required. For this reason, sinusoidal

excitations called calibration lines are continuously injected at select frequencies using the Pcal and the three lowest stages of actuation (see Fig. 5). This allows us to measure the detectors continuously while not hindering their operation or sensitivity. Our ability to use measurements at only a few frequencies to effectively correct the response function $R(f)$ at all frequencies requires the functional form of our models of A and C to be accurate representations of the true calibration. The results shown later in this section (especially Fig. 16 and Fig. 17) suggest that our models are indeed good representations of the true calibration, with systematic errors near 1% and 1°.

The frequencies of calibration lines need to be chosen with care, for several reasons:

- Calibration lines cannot be placed near any resonant frequencies of the suspensions or violin mode frequencies.
- Calibration line frequencies in Hz should not be integers (they are often chosen as prime numbers divided by 10).
- Calibration lines cannot be harmonics of each other, or harmonics of 60 Hz, due to the power mains.
- Calibration lines should avoid the most sensitive band in LIGO's detection band.
- Each interferometer should use a unique set of calibration line frequencies.
- Continuous-wave search groups prefer calibration lines to be at least 1.0 Hz away from known pulsar frequencies, a restriction that has not been feasible below 20 Hz, where an effort is still made to keep lines 0.1 Hz away as much as possible.
- Searches for the GW stochastic background require a minimum separation of calibration lines of 0.5 Hz
- The calibration lines used to estimate κ_T , κ_P , and κ_U (1 Pcal line and 3 actuator lines) need to be placed within ~ 1 Hz of each other, due to the approximation noted in Eq. 5.2.9.

Table 2 shows the calibration lines planned for use in O3, with their frequencies at each site and purpose.

Table 2 : Summary of the purpose of each calibration line during O3

Line	Purpose	Injected with	H1 frequency	L1 frequency
f_4	Compute f_s and Q	Pcal	7.93 Hz	N/A
f_U	Compute κ_U	UIM actuator	15.6 Hz	15.1 Hz
f_P	Compute κ_P	PUM actuator	16.4 Hz	15.7 Hz
f_1	Compute κ_T , κ_P and κ_U	Pcal	17.1 Hz	16.3 Hz
f_T	Compute κ_T	TST actuator	17.6 Hz	16.9 Hz
f_2	Compute κ_C and f_{cc}	Pcal	410.3 Hz	434.9 Hz
f_3	High-frequency check	Pcal	1083.7 Hz	1083.1 Hz

The Pcal line at f_1 , as well as the actuator lines f_j are placed in a range of 10 - 40 Hz, where the impact of time dependence in the actuation is significant, for the purpose of measuring the actuation. A higher Pcal line at $f_2 \sim 400$ Hz is located near the coupled cavity pole frequency in order to measure the optical gain and coupled cavity pole frequency. At H1 only, an additional Pcal line is located at 7.93 Hz, where the impact of SRC detuning is significant, in order to measure f_s and Q . During O2, a calibration line was injected into the control signal d_{ctrl} just after the digital filter D (see Fig. 5) for the purpose of computing the factor κ_{PU} , representing the combined time dependence of the penultimate and upper intermediate stages of actuation.

5.2 Computing time-dependent correction factors

5.2.1 Measuring the calibration lines

In order to measure the calibration at the calibration-line frequencies f_n , we compare the amplitude and phase of the error signal d_{err} and the injection channel at each frequency. If the ratio $d_{err}(f_n)/x_n(f_n)$ deviates from what is predicted by the static reference model, then it is necessary to correct the model. When taking these measurements, it is necessary

to remove signal components at all other frequencies and represent the calibration lines in the frequency domain. In order to do this efficiently, we use demodulation.¹ To demodulate a time series, the `gst1al` calibration pipeline first multiplies each sample by $e^{-i\omega t}$, where ω is the angular frequency of a calibration line. The resulting time series is then downsampled to 16 Hz, using an effective anti-aliasing filter, necessary to prevent excess noise in the computed TDCFs. Then a 20-second Blackman window is used to low-pass filter the time series. For a calibration line with amplitude a and phase ϕ ,

$$\begin{aligned} B * \{e^{-i\omega t} [a \cos(\omega t - \phi) + n(t)]\} &= \\ B * \left\{ \frac{a}{2} [e^{-i\phi} + e^{i(-2\omega t + \phi)}] + n(t)e^{-i\omega t} \right\} &\approx \frac{a}{2} e^{-i\phi}, \end{aligned} \quad (5.2.1)$$

where B is the Blackman window and $n(t)$ is noise, that is, anything other than the sinusoidal injection [16]. The precision of the result is improved by increasing the length of the Blackman window. Since the Pcal is used as the reference for displacement at each calibration line, a conversion factor is applied when demodulating the Pcal injection channel to convert it from counts in to meters of displacement. Then, the sensing function and components of the actuation function can be measured by comparison of the demodulated signals in d_{err} and the actuator injection channels to those of the calibrated Pcal.

Currently, the amplitude and phase of the calibration lines is measured in d_{err} , but not in d_{ctrl} . For this reason, the solution used to compute the TDCFs has necessary dependence on the digital filter D . This nullifies the benefit of the convention used to compute $h(t)$ in Eq. 2.0.1 when time dependence is compensated for. The simple substitution $\tilde{D} = \tilde{d}_{\text{ctrl}}/\tilde{d}_{\text{err}}$ in any of the following derivations can be used to formulate a solution that is independent of D . The only exception is in Eq. 5.2.10, where the response function is evaluated at f_{ctrl} , since x_{ctrl} is injected between the pick-off points for d_{err} and d_{ctrl} . This is an area of current development, with the eventual goal of avoiding dependence on any portion of the DARM feedback control loop that is not tracked in the TDCFs.

¹During O1, the `gst1al` calibration pipeline took 10-second Fourier transforms to measure the calibration lines.

5.2.2 Computing the time-dependence of the actuation function

In the current method used by the `gst1a1` calibration pipeline to compute the TDCFs, the time-dependence of the actuation function is computed first, and the measured values of the κ_j and τ_j are passed to the following stages of computing the time dependence of the sensing function. This method is based on that given in [21] and relies on a few approximations, noted below.

To begin solving for the values of the TDCFs, let us solve the full DARM feedback loop depicted in Fig. 5, including injections, for d_{err} :

$$\tilde{d}_{\text{err}} = \tilde{C}_{\text{res}} \left(\frac{\kappa_{\text{C}}}{1 + i f / f_{\text{cc}}} \right) \left(\frac{f^2}{f^2 + f_{\text{s}}^2 - i f f_{\text{s}} / Q} \right) \left(\widetilde{\Delta L}_{\text{free}} + \tilde{x}_{\text{pc}} - \widetilde{\Delta L}_{\text{ctrl}} \right), \quad (5.2.2)$$

where $\tilde{C}_{\text{res}} = H_{\text{C}} C_{\text{R}} \exp[-2\pi i f \tau_{\text{C}}]$ contains the portion of the sensing function that has no parameterized time dependence. Noting that

$$\begin{aligned} \widetilde{\Delta L}_{\text{ctrl}} = & \kappa_{\text{T}} e^{i\omega\tau_{\text{T}}} \left(\tilde{A}_{\text{T}} \tilde{D} \tilde{d}_{\text{err}} - \tilde{A}_{\text{T},0} \tilde{x}_{\text{T}} \right) + \kappa_{\text{P}} e^{i\omega\tau_{\text{P}}} \left(\tilde{A}_{\text{P}} \tilde{D} \tilde{d}_{\text{err}} - \tilde{A}_{\text{P},0} \tilde{x}_{\text{P}} \right) \\ & + \kappa_{\text{U}} e^{i\omega\tau_{\text{U}}} \left(\tilde{A}_{\text{U}} \tilde{D} \tilde{d}_{\text{err}} - \tilde{A}_{\text{U},0} \tilde{x}_{\text{U}} \right), \end{aligned} \quad (5.2.3)$$

and letting

$$S_{\text{c}} = \frac{\kappa_{\text{C}}}{1 + i f / f_{\text{cc}}}, \quad (5.2.4)$$

$$S_{\text{s}} = \frac{f^2}{f^2 + f_{\text{s}}^2 - i f f_{\text{s}} / Q}, \quad (5.2.5)$$

we see that

$$\tilde{d}_{\text{err}} = \frac{\widetilde{\Delta L}_{\text{free}} + \tilde{x}_{\text{pc}} + \kappa_{\text{T}} e^{i\omega\tau_{\text{T}}} \tilde{A}_{\text{T},0} \tilde{x}_{\text{T}} + \kappa_{\text{P}} e^{i\omega\tau_{\text{P}}} \tilde{A}_{\text{P},0} \tilde{x}_{\text{P}} + \kappa_{\text{U}} e^{i\omega\tau_{\text{U}}} \tilde{A}_{\text{U},0} \tilde{x}_{\text{U}}}{\left(S_{\text{c}} S_{\text{s}} \tilde{C}_{\text{res}} \right)^{-1} + \left(\kappa_{\text{T}} e^{i\omega\tau_{\text{T}}} \tilde{A}_{\text{T}} + \kappa_{\text{P}} e^{i\omega\tau_{\text{P}}} \tilde{A}_{\text{P}} + \kappa_{\text{U}} e^{i\omega\tau_{\text{U}}} \tilde{A}_{\text{U}} \right) \tilde{D}} \quad (5.2.6)$$

$$= \tilde{R}^{-1} \left(\widetilde{\Delta L}_{\text{free}} + \tilde{x}_{\text{pc}} + \kappa_{\text{T}} e^{i\omega\tau_{\text{T}}} \tilde{A}_{\text{T},0} \tilde{x}_{\text{T}} + \kappa_{\text{P}} e^{i\omega\tau_{\text{P}}} \tilde{A}_{\text{P},0} \tilde{x}_{\text{P}} + \kappa_{\text{U}} e^{i\omega\tau_{\text{U}}} \tilde{A}_{\text{U},0} \tilde{x}_{\text{U}} \right),$$

where we have used the time-dependent response function \tilde{R} , defined in Eq. 2.1.5. To measure the time dependence of the actuation, we demodulate d_{err} and the injections x_{pc} and x_j at the frequencies f_1 and f_j , yielding the two equations:

$$\tilde{d}_{\text{err}}(f_j) = \kappa_j e^{i\omega_j \tau_j} \tilde{R}^{-1}(f_j) \tilde{A}_{j,0}(f_j) \tilde{x}_j(f_j), \quad (5.2.7)$$

$$\tilde{d}_{\text{err}}(f_1) = \tilde{R}^{-1}(f_1) \tilde{x}_{\text{pc}}(f_1). \quad (5.2.8)$$

Taking the following ratios results in an estimate of the κ_j :

$$\kappa_j e^{i\omega_j \tau_j} \approx \frac{1}{\tilde{A}_j(f_j)} \cdot \frac{\tilde{d}_{\text{err}}(f_j)}{\tilde{x}_j(f_j)} \left(\frac{\tilde{d}_{\text{err}}(f_1)}{\tilde{x}_{\text{pc}}(f_1)} \right)^{-1} \cdot \frac{\tilde{R}^{\text{model}}(f_j)}{\tilde{R}^{\text{model}}(f_1)}. \quad (5.2.9)$$

Note that the replacement of the time-dependent response function R with the static reference model response function R^{model} represents an approximation that relies on the slope of the response function remaining nearly constant and the calibration lines at f_1 and f_j being close in frequency. An effort is made to keep the separation between these lines close to 1 Hz (see Table 2).

During O2, the factors κ_P and κ_U were tracked as the combined factor κ_{PU} using the injection x_{ctrl} made directly into the control signal d_{ctrl} after the digital filter D (see Fig. 5). κ_{PU} was estimated as

$$\kappa_{\text{PU}} e^{i\omega_{\text{ctrl}} \tau_{\text{PU}}} \approx - \frac{1}{\tilde{A}_{\text{PU}}(f_{\text{ctrl}})} \left[\frac{\tilde{d}_{\text{err}}(f_{\text{ctrl}})}{\tilde{x}_{\text{ctrl}}(f_{\text{ctrl}})} \left(\frac{\tilde{d}_{\text{err}}(f_1)}{\tilde{x}_{\text{pc}}(f_1)} \right)^{-1} \cdot \frac{\tilde{R}^{\text{model}}(f_{\text{ctrl}})}{\tilde{R}^{\text{model}}(f_1)} \right. \\ \left. + \kappa_{\text{T}} e^{i\omega_{\text{T}} \tau_{\text{T}}} \tilde{A}_{\text{T}}(f_{\text{ctrl}}) \right], \quad (5.2.10)$$

where the frequency f_{ctrl} was necessarily chosen to be within ~ 1 Hz of f_1 .

5.2.3 Computing the optical gain and coupled cavity pole frequency

Using the previously computed solutions for the time dependence of the actuation function, we can now estimate the time-dependent parameters of the sensing function, starting with the optical gain κ_C and coupled cavity pole frequency f_{cc} . To do this, we demodulate d_{err} and x_{pc} at the Pcal line frequency f_2 and estimate the factor

$$S_c(f_2) \approx \frac{1}{\tilde{C}_{\text{res}}} \left(\frac{\tilde{x}_{\text{pc}}}{\tilde{d}_{\text{err}}} - \tilde{D} \left[\kappa_{\text{T}} e^{i\omega_{\text{T}} \tau_{\text{T}}} \tilde{A}_{\text{T}} + \kappa_{\text{P}} e^{i\omega_{\text{P}} \tau_{\text{P}}} \tilde{A}_{\text{P}} + \kappa_{\text{U}} e^{i\omega_{\text{U}} \tau_{\text{U}}} \tilde{A}_{\text{U}} \right] \right)^{-1} \Bigg|_{f_2}. \quad (5.2.11)$$

Note that we neglected the detuning of the SRC by setting $S_s(f_2) = 1$. As long as $f_s \ll f_2$, the error introduced by this approximation is negligibly small. κ_C and f_{cc} can then be computed using

$$\kappa_C = \frac{|S_c(f_2)|^2}{\Re[S(f_2)]}, \quad (5.2.12)$$

$$f_{\text{cc}} = - \frac{\Re[S_c(f_2)]}{\Im[S(f_2)]} f_2. \quad (5.2.13)$$

It is important that κ_C and f_{cc} are computed before f_s and Q , as temporal variations in the optical gain have a significant impact on the calculation of f_s and Q .

5.2.4 Computing the detuning of the signal recycling cavity

The algorithms used in the `gstlal` calibration pipeline to compute f_s and Q were not developed until O2 was in progress, as the detuning of the SRC was not known to have significant time dependence at H1 until the run had started. Typical values at H1 during O2 for the optical antispring frequency were 4 - 9 Hz, while values at L1 were estimated to be closer to 3 Hz, making the impact of SRC detuning less significant there. In the months leading up to O3, the L1 detector has shown some evidence of an optical spring rather than an antispring during quantum squeezing of input laser light (described in [31]). The algorithm in the `gstlal` calibration pipeline has therefore been generalized to compensate for either an antispring or a spring by allowing $f_s^2 < 0$.

By demodulating d_{err} and x_{pc} at the lowest Pcal line at f_4 , we find from Eq. 5.2.6 that

$$S_s(f_4) = \left[S_c \tilde{C}_{\text{res}} \left(\frac{\tilde{x}_{\text{pc}}}{\tilde{d}_{\text{err}}} - (\kappa_T e^{i\omega\tau_T} \tilde{A}_T + \kappa_P e^{i\omega\tau_P} \tilde{A}_P + \kappa_U e^{i\omega\tau_U} \tilde{A}_U) \tilde{D} \right) \right]^{-1} \Big|_{f_4}. \quad (5.2.14)$$

Then, the solutions for f_s and Q are

$$f_s = f_4 \sqrt{\Re[S_s^{-1}(f_4) - 1]}, \quad (5.2.15)$$

$$Q = -\frac{\sqrt{\Re[S_s^{-1}(f_4) - 1]}}{\Im[S_s^{-1}(f_4) - 1]}. \quad (5.2.16)$$

During O2, the values of f_s and Q estimated using the Pcal line at f_4 were subject to both excessive noisy fluctuations as well as systematic errors [17]. Using the higher-frequency line at f_1 , primarily intended to measure the actuation function, was shown to produce results consistent with the reference model values. Although the impact of SRC detuning is greater at f_4 , the seismic noise at this frequency makes it difficult to achieve adequate SNR. This not only makes it difficult to inject a calibration line loud enough to attenuate noise with a reasonable integration time, it also means that the measurements of A and C that the reference model is based on may be subject to greater systematic error at such a low frequency. Fig. 15 shows time series plots of f_s and Q computed

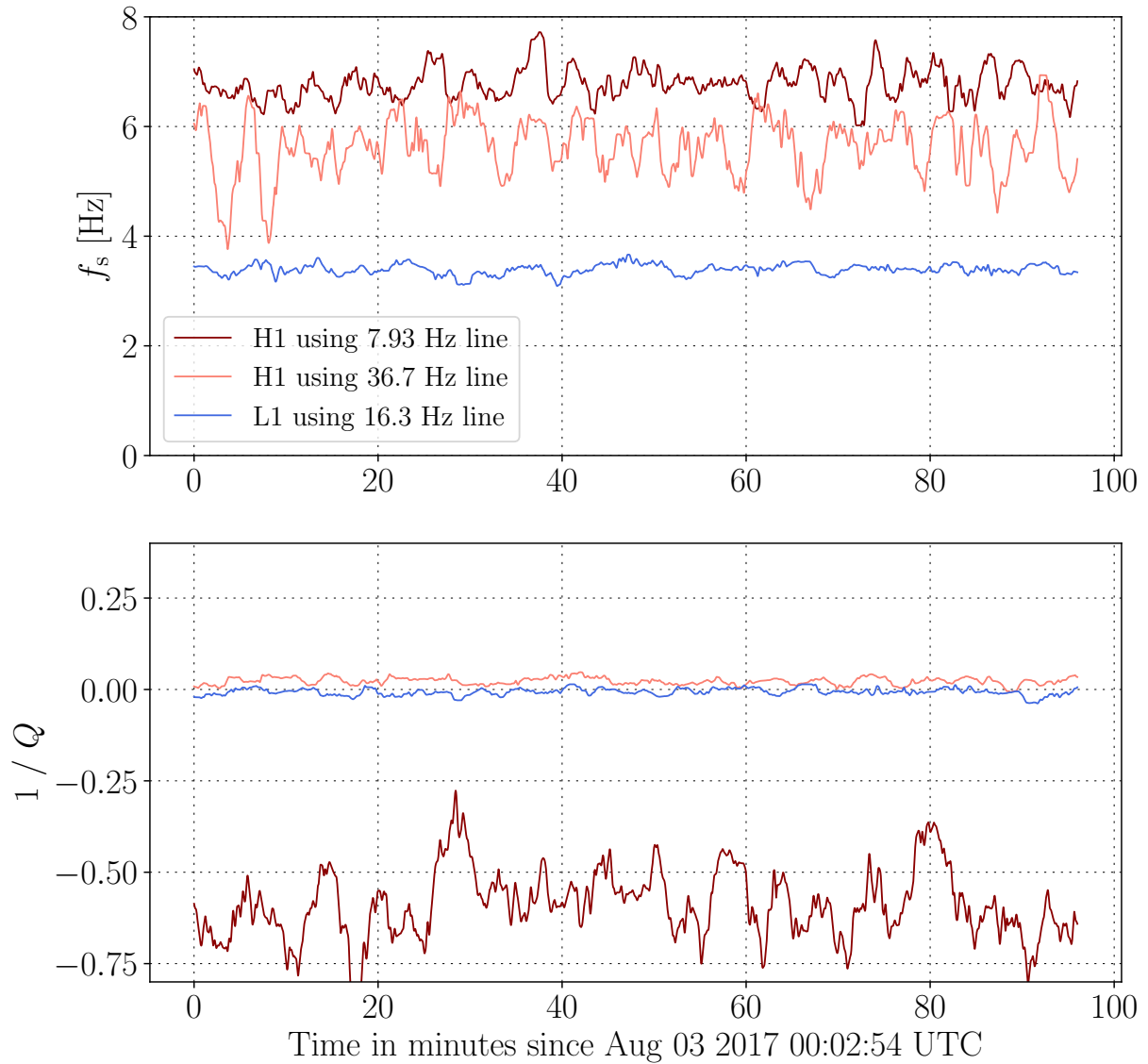


Figure 15 : Time series of f_s and Q computed by the `gstlal` calibration pipeline using the two Pcal lines at f_4 and f_1 at H1, and using the Pcal line at f_1 at L1. The negative computed value of Q at H1 using the lower line is evidence of a systematic error, whereas all values computed using the Pcal line at f_1 are consistent with expectations based on the reference models.

by the `gstlal` calibration pipeline using the Pcal line at f_4 and at f_1 . An additional advantage of using the line at f_1 is that SRC detuning can be measured at L1 using this line. Results from L1 using this line are also shown in the figure, consistent with reference model measurements made during O2. The repeated use of the Pcal line at f_1 to measure the actuation and SRC detuning has evoked concerns about covariance between the TDCFs. However, using the Pcal lines at f_1 and f_2 in addition to the three actuator

lines at f_j still provides magnitude and phase information at 5 frequencies, enough to solve for 10 real unknowns, which is the number of TDCFs in the current model.

5.2.5 Drawbacks of approximations in the calculation of the TDCFs

The approximations noted in Eq. 5.2.11 and especially in Eq. 5.2.9 are now known to cause systematic biases in the computed values of the TDCFs. Of particular interest is the impact of the approximation in Eq. 5.2.9 on the estimates of the τ_j , as changes in the slope of the time-dependent response function R caused by normal fluctuations in the TDCFs are known to cause apparent deviations from zero in τ_j . Although the

Table 3 : A simulation of time dependence showing unwanted covariance in the TDCFs

Simulated Value	Measured $\kappa_T e^{i\omega_T \tau_T}$	Measured $\kappa_{PU} e^{i\omega_{PU} \tau_{PU}}$	Meas. κ_C	Meas. f_{cc} (Hz)	Meas. f_s (Hz)	Meas. Q^{-1}
Nominal values	$0.9999 + 0.0000i$	$1.0000 + 0.0000i$	1.0000	360.01	6.917	-0.0572
$\kappa_T e^{i\omega_T \tau_T}$ = $1.1 + 0.0i$	$1.1022 - 0.0055i$	$0.9883 - 0.0100i$	1.0001	360.02	7.637	-0.1826
$\kappa_T e^{i\omega_T \tau_T}$ = $1.0 - 0.05i$	$0.9974 - 0.0533i$	$0.9925 + 0.0055i$	1.0001	359.99	7.390	-0.1169
$\kappa_{PU} e^{i\omega_{PU} \tau_{PU}}$ = $1.1 + 0.0i$	$0.9956 + 0.0027i$	$1.1037 + 0.0124i$	1.0000	360.00	6.658	-0.0042
$\kappa_{PU} e^{i\omega_{PU} \tau_{PU}}$ = $1.0 + 0.05i$	$0.9996 - 0.0021i$	$0.9944 + 0.0492i$	1.0000	360.02	7.273	-0.1139
κ_C = 1.1	$0.9990 - 0.0025i$	$0.9931 + 0.0005i$	1.1001	360.02	7.397	-0.1389
f_{cc} = 340 Hz	$0.9997 + 0.0001i$	$0.9999 + 0.0008i$	1.0000	340.01	6.920	-0.0565
f_s = 10 Hz	$1.0011 - 0.0002i$	$1.0003 - 0.0029i$	0.9991	360.33	9.966	-0.0289
Q^{-1} = 0.5	$1.0009 - 0.0016i$	$0.9967 - 0.0035i$	0.9914	366.92	7.064	0.3390

sudden changes in τ_j seen during O2 are clearly not caused by this, it could contribute significantly to their values, leading to systematic errors in the corrected calibration. It may even be possible that in some instances, compensating for time dependence in τ_j could be detrimental to calibration accuracy. To assess the overall impact of all approximations made in the calculations of the TDCFs on their estimated values, the impact of variations in the TDCFs was simulated using real H1 data from O2. Since d_{err} is used to measure

the TDCFs, d_{err} was filtered using

$$\tilde{d}_{\text{err}}^{\text{sim}}(f) = \frac{\tilde{R}(f)}{\tilde{R}^{\text{sim}}(f)} \tilde{d}_{\text{err}}, \quad (5.2.17)$$

where $\tilde{R}(f)$ is the true time-dependent response function and $\tilde{R}^{\text{sim}}(f)$ is the response function being simulated in $d_{\text{err}}^{\text{sim}}$. After this manipulation of d_{err} , the TDCFs were measured and computed as they are in the `gstlal` calibration pipeline. The first step in this investigation is to find the true response function $\tilde{R}(f)$. Since we are attempting to measure systematic errors in TDCFs, we cannot simply use a response function corrected using the computed values of the TDCFs. Instead, the above operation was done repeatedly using $\tilde{R}^{\text{sim}}(f) = \tilde{R}^{\text{model}}(f)$, and adjusting the TDFCs used in $\tilde{R}(f)$ until the TDFCs computed in the pipeline were exactly equal to their nominal values in the reference model. Then, each TDCF was individually varied to assess the impact on all other TDCFs.

The results of this simulation are shown in Table 3. 30 minutes of H1 data were averaged, starting at 12:00 UTC on April 26, 2017. The nominal values of the TDFCs in the reference model used for this study were $\kappa_j e^{i\omega_j \tau_j} = 1.0$, $\kappa_C = 1.0$, $f_{cc} = 360.0$ Hz, $f_s = 6.91$ Hz, and $Q = 21.739$. Note that it was impossible to achieve a measured value of Q that agreed with the reference model, which is not surprising given the fact that this study was done using the Pcal line at f_4 to compute f_s and Q . The results show significant covariance between κ_T , κ_{PU} , τ_T , and τ_{PU} , and in some cases typical variations lead to $\sim 1\%$ errors in other TDCFs. Additionally, estimates of f_s and Q are significantly impacted by every previously-computed TDCF other than f_{cc} . One solution to this problem is to frequently update the reference model with a new set of measurements, to prevent the TDCFs from straying too far from their nominal values. However, this is somewhat impractical, especially since κ_C is known to change on timescales of minutes.

5.2.6 Computing the TDCFs using an exact solution

In order to avoid the approximations currently used in computing the TDCFs, we shall now derive a full algebraic solution for all the TDCFs using the three actuator lines and

two Pcal lines, the only approximating assumption being that the time delays τ_j are small. Evaluating Eq. 5.2.6 at the calibration line frequencies, we have

$$\tilde{d}_{\text{err}}(f_j) = \tilde{R}^{-1}(f_j) \kappa_j e^{i\omega_j \tau_j} \tilde{A}_{j,0}(f_j) \tilde{x}_j(f_j) \quad (5.2.18)$$

$$\tilde{d}_{\text{err}}(f_\ell) = \tilde{R}^{-1}(f_\ell) \tilde{x}_{\text{pc}}(f_\ell). \quad (5.2.19)$$

Let us then define

$$X^j \equiv \frac{\tilde{x}_j(f_j)}{\tilde{d}_{\text{err}}(f_j)} = \frac{\tilde{R}(f_j)}{\kappa_j e^{i\omega_j \tau_j} \tilde{A}_{j,0}(f_j)}, \quad (5.2.20)$$

$$X^\ell \equiv \frac{\tilde{x}_{\text{pc}}(f_\ell)}{\tilde{d}_{\text{err}}(f_\ell)} = \tilde{R}(f_\ell). \quad (5.2.21)$$

Expanding these yields 5 complex equations with 10 real unknowns:

$$X^j = \frac{1}{\kappa_j e^{i\omega_j \tau_j} \tilde{A}_{j,0}^j} \left[\left(\frac{1 + i f_j / f_{\text{cc}}}{\kappa_{\text{C}} \tilde{C}_{\text{res}}^j} \right) \left(\frac{f_j^2 + f_s^2 - i f_j f_s / Q}{f_j^2} \right) + \tilde{D}^j \left(\kappa_{\text{T}} e^{i\omega_j \tau_{\text{T}}} \tilde{A}_{\text{T}}^j + \kappa_{\text{P}} e^{i\omega_j \tau_{\text{P}}} \tilde{A}_{\text{P}}^j + \kappa_{\text{U}} e^{i\omega_j \tau_{\text{U}}} \tilde{A}_{\text{U}}^j \right) \right], \quad (5.2.22)$$

$$X^\ell = \left(\frac{1 + i f_\ell / f_{\text{cc}}}{\kappa_{\text{C}} \tilde{C}_{\text{res}}^\ell} \right) \left(\frac{f_\ell^2 + f_s^2 - i f_\ell f_s / Q}{f_\ell^2} \right) + \tilde{D}^\ell \left(\kappa_{\text{T}} e^{i\omega_\ell \tau_{\text{T}}} \tilde{A}_{\text{T}}^\ell + \kappa_{\text{P}} e^{i\omega_\ell \tau_{\text{P}}} \tilde{A}_{\text{P}}^\ell + \kappa_{\text{U}} e^{i\omega_\ell \tau_{\text{U}}} \tilde{A}_{\text{U}}^\ell \right), \quad (5.2.23)$$

where we have used the shorthand notation $\tilde{F}^j = \tilde{F}(f_j)$ and $\tilde{F}^\ell = \tilde{F}(f_\ell)$ for any function of frequency $\tilde{F}(f)$. Breaking these into real and imaginary parts and rearranging produces 10 equations to be solved for the 10 unknowns:

$$\kappa_{\text{C}} \Re(\tilde{Z}^j) = 1 + \frac{f_s^2}{f_j^2} + \frac{f_s}{f_{\text{cc}} Q} + \Re(\tilde{G}_{\text{res}}^j), \quad (5.2.24)$$

$$\kappa_{\text{C}} \Im(\tilde{Z}^j) = \frac{f_j}{f_{\text{cc}}} + \frac{f_s^2}{f_j f_{\text{cc}}} - \frac{f_s}{f_j Q} + \Im(\tilde{G}_{\text{res}}^j), \quad (5.2.25)$$

$$\kappa_{\text{C}} \Re(\tilde{Y}^\ell) = 1 + \frac{f_s^2}{f_\ell^2} + \frac{f_s}{f_{\text{cc}} Q} + \Re(\tilde{G}_{\text{res}}^\ell), \quad (5.2.26)$$

$$\kappa_{\text{C}} \Im(\tilde{Y}^\ell) = \frac{f_\ell}{f_{\text{cc}}} + \frac{f_s^2}{f_\ell f_{\text{cc}}} - \frac{f_s}{f_\ell Q} + \Im(\tilde{G}_{\text{res}}^\ell). \quad (5.2.27)$$

For convenience, we have defined the parameters

$$\tilde{Z}^j = \kappa_j \tilde{C}_{\text{res}}^j \tilde{A}_{j,0}^j X^j e^{i\omega_j \tau_j}, \quad (5.2.28)$$

$$\tilde{Y}^\ell = \tilde{C}_{\text{res}}^\ell X^\ell, \quad (5.2.29)$$

$$\tilde{G}_{\text{res}}^n = \sum_j \left(\kappa_j \tilde{C}_{\text{res}}^n \tilde{D}^n \tilde{A}_j^n e^{i\omega_n \tau_j} \right). \quad (5.2.30)$$

Note that \tilde{Z}^j and \tilde{G}^n contain unknowns, but only the time dependence of the actuation, while \tilde{Y}^ℓ contains no unknowns. The solution method adopted here is to solve all 10 equations for one unknown. Then, we will have 10 expressions that are all equal to each other, for a total of 45 equations. However, only 9 of these will be linearly independent, and a wise choice can make the rest of the solution easier. To be somewhat consistent with the method currently used, we solve for Q first:

$$Q^{-1} = \frac{f_{\text{cc}}}{f_s} \left(\kappa_C \Re(\tilde{Z}^j) - 1 - \frac{f_s^2}{f_j^2} - \kappa_C \Re(\tilde{G}_{\text{res}}^j) \right) \quad (5.2.31)$$

$$= \frac{-f_j}{f_s} \left(\kappa_C \Im(\tilde{Z}^j) - \frac{f_j}{f_{\text{cc}}} - \frac{f_s^2}{f_j f_{\text{cc}}} - \kappa_C \Im(\tilde{G}_{\text{res}}^j) \right) \quad (5.2.32)$$

$$= \frac{f_{\text{cc}}}{f_s} \left(\kappa_C \Re(\tilde{Y}^\ell) - 1 - \frac{f_s^2}{f_\ell^2} - \kappa_C \Re(\tilde{G}_{\text{res}}^\ell) \right) \quad (5.2.33)$$

$$= \frac{-f_\ell}{f_s} \left(\kappa_C \Im(\tilde{Y}^\ell) - \frac{f_\ell}{f_{\text{cc}}} - \frac{f_s^2}{f_\ell f_{\text{cc}}} - \kappa_C \Im(\tilde{G}_{\text{res}}^\ell) \right). \quad (5.2.34)$$

Setting the expressions 5.2.33 and 5.2.34 equal,

$$f_\ell f_{\text{cc}} \left[\kappa_C \Re(\tilde{Y}^\ell) - 1 - \frac{f_s^2}{f_\ell^2} - \kappa_C \Re(\tilde{G}_{\text{res}}^\ell) \right] + \kappa_C f_\ell^2 \Im(\tilde{Y}^\ell) - \frac{f_\ell^3}{f_{\text{cc}}} - \frac{f_\ell f_s^2}{f_{\text{cc}}} - \kappa_C f_\ell^2 \Im(\tilde{G}_{\text{res}}^\ell) = 0. \quad (5.2.35)$$

Setting expressions 5.2.33 equal to each other for f_1 and f_2 ,

$$\kappa_C \Re(\tilde{Y}^1) - \frac{f_s^2}{f_1^2} - \kappa_C \Re(\tilde{G}_{\text{res}}^1) = \kappa_C \Re(\tilde{Y}^2) - \frac{f_s^2}{f_2^2} - \kappa_C \Re(\tilde{G}_{\text{res}}^2). \quad (5.2.36)$$

Setting expression 5.2.33 equal to the expressions 5.2.31 gives the three equations

$$\kappa_C \Re(\tilde{Y}^\ell) - \frac{f_s^2}{f_\ell^2} - \kappa_C \Re(\tilde{G}_{\text{res}}^\ell) = \kappa_C \Re(\tilde{Z}^j) - \frac{f_s^2}{f_j^2} - \kappa_C \Re(\tilde{G}_{\text{res}}^j). \quad (5.2.37)$$

Setting expressions 5.2.34 equal to each other for f_1 and f_2 ,

$$f_1 \left[\kappa_C \Im(\tilde{Y}^1) - \frac{f_1}{f_{\text{cc}}} - \kappa_C \Im(\tilde{G}_{\text{res}}^1) \right] = f_2 \left[\kappa_C \Im(\tilde{Y}^2) - \frac{f_2}{f_{\text{cc}}} - \kappa_C \Im(\tilde{G}_{\text{res}}^2) \right]. \quad (5.2.38)$$

Setting expression 5.2.34 equal to the expressions 5.2.32 gives the three equations

$$f_\ell \left[\kappa_C \mathfrak{S}(\tilde{Y}^\ell) - \frac{f_\ell}{f_{cc}} - \kappa_C \mathfrak{S}(\tilde{G}_{\text{res}}^\ell) \right] = f_j \left[\kappa_C \mathfrak{S}(\tilde{Z}^j) - \frac{f_j}{f_{cc}} - \kappa_C \mathfrak{S}(\tilde{G}_{\text{res}}^j) \right]. \quad (5.2.39)$$

The solutions for f_s are then

$$f_s^2 = \left(\frac{f_{cc}}{f_\ell} + \frac{f_\ell}{f_{cc}} \right)^{-1} \left[f_\ell f_{cc} \left(\kappa_C \mathfrak{R}(\tilde{Y}^\ell) - 1 - \kappa_C \mathfrak{R}(\tilde{G}_{\text{res}}^\ell) \right) + \kappa_C f_\ell^2 \mathfrak{S}(\tilde{Y}^\ell) - \frac{f_\ell^3}{f_{cc}} - \kappa_C f_\ell^2 \mathfrak{S}(\tilde{G}_{\text{res}}^\ell) \right] \quad (5.2.40)$$

$$= \kappa_C \left(\frac{1}{f_2^2} - \frac{1}{f_1^2} \right)^{-1} \left[\mathfrak{R}(\tilde{Y}^2) - \mathfrak{R}(\tilde{G}_{\text{res}}^2) - \mathfrak{R}(\tilde{Y}^1) + \mathfrak{R}(\tilde{G}_{\text{res}}^1) \right] \quad (5.2.41)$$

$$= \kappa_C \left(\frac{1}{f_j^2} - \frac{1}{f_\ell^2} \right)^{-1} \left[\mathfrak{R}(\tilde{Z}^j) - \mathfrak{R}(\tilde{G}_{\text{res}}^j) - \mathfrak{R}(\tilde{Y}^\ell) + \mathfrak{R}(\tilde{G}_{\text{res}}^\ell) \right]. \quad (5.2.42)$$

Note that Eqs. 5.2.38 and 5.2.39 have no dependence on f_s , and therefore can be used in the next set of equations. Additionally, setting the expressions 5.2.40 and 5.2.41 equal,

$$\begin{aligned} & \left(\frac{f_{cc}}{f_\ell} + \frac{f_\ell}{f_{cc}} \right)^{-1} \left[f_\ell f_{cc} \left(\kappa_C \mathfrak{R}(\tilde{Y}^\ell) - 1 - \kappa_C \mathfrak{R}(\tilde{G}_{\text{res}}^\ell) \right) + \kappa_C f_\ell^2 \mathfrak{S}(\tilde{Y}^\ell) - \frac{f_\ell^3}{f_{cc}} - \kappa_C f_\ell^2 \mathfrak{S}(\tilde{G}_{\text{res}}^\ell) \right] \\ &= \kappa_C \left(\frac{1}{f_2^2} - \frac{1}{f_1^2} \right)^{-1} \left[\mathfrak{R}(\tilde{Y}^2) - \mathfrak{R}(\tilde{G}_{\text{res}}^2) - \mathfrak{R}(\tilde{Y}^1) + \mathfrak{R}(\tilde{G}_{\text{res}}^1) \right]. \end{aligned} \quad (5.2.43)$$

Then let us set the expressions 5.2.41 and 5.2.42 equal, noting that either choice of value for ℓ leads to the same simplified result

$$\begin{aligned} & \left(\frac{1}{f_j^2} - \frac{1}{f_2^2} \right) \left(\mathfrak{R}(\tilde{G}_{\text{res}}^1) - \mathfrak{R}(\tilde{Y}^1) \right) - \left(\frac{1}{f_j^2} - \frac{1}{f_1^2} \right) \left(\mathfrak{R}(\tilde{G}_{\text{res}}^2) - \mathfrak{R}(\tilde{Y}^2) \right) \\ &= \left(\frac{1}{f_1^2} - \frac{1}{f_2^2} \right) \left(\mathfrak{R}(\tilde{G}_{\text{res}}^j) - \mathfrak{R}(\tilde{Z}^j) \right). \end{aligned} \quad (5.2.44)$$

Next, we solve for f_{cc} , noting that only Eqs. 5.2.38, 5.2.39, and 5.2.43 have dependence on f_{cc} . Starting with Eqs. 5.2.38 and 5.2.39,

$$f_{cc} = \frac{f_2^2 - f_1^2}{\kappa_C \left[f_1 \mathfrak{S}(\tilde{G}_{\text{res}}^1) - f_1 \mathfrak{S}(\tilde{Y}^1) - f_2 \mathfrak{S}(\tilde{G}_{\text{res}}^2) + f_2 \mathfrak{S}(\tilde{Y}^2) \right]} \quad (5.2.45)$$

$$= \frac{f_j^2 - f_\ell^2}{\kappa_C \left[f_\ell \mathfrak{S}(\tilde{G}_{\text{res}}^\ell) - f_\ell \mathfrak{S}(\tilde{Y}^\ell) - f_j \mathfrak{S}(\tilde{G}_{\text{res}}^j) + f_j \mathfrak{S}(\tilde{Z}^j) \right]}. \quad (5.2.46)$$

Eq. 5.2.43 is a quadratic equation with the solution

$$f_{cc} = f_\ell \frac{\kappa_C \tilde{I}^\ell + \sqrt{\kappa_C^2 (\tilde{I}^\ell)^2 - 4(\kappa_C \xi + f_\ell^2) \left[\kappa_C (\tilde{H}^\ell + \xi) + f_\ell^2 \right]}}{-2 \left[\kappa_C (\tilde{H}^\ell + \xi) + f_\ell^2 \right]} \quad (5.2.47)$$

where we have defined

$$\tilde{H}^\ell = f_\ell^2 \left(\Re(\tilde{G}_{\text{res}}^\ell) - \Re(\tilde{Y}^\ell) \right) \quad (5.2.48)$$

$$\tilde{I}^\ell = f_\ell^2 \left(\Im(\tilde{G}_{\text{res}}^\ell) - \Im(\tilde{Y}^\ell) \right) \quad (5.2.49)$$

$$\xi = \frac{f_2^2 \tilde{H}^1 - f_1^2 \tilde{H}^2}{f_1^2 - f_2^2}. \quad (5.2.50)$$

It can be shown that this is the desired solution to the quadratic equation by substituting model values back into the defined parameters and showing that this result is equal to f_{cc} . We now have 7 unknowns remaining, and the first 3 equations are given by Eq. 5.2.44. We obtain three more equations by setting the expressions 5.2.45 and 5.2.46 equal, noting that either choice of value for ℓ leads to the same simplified result

$$\begin{aligned} f_1 (f_j^2 - f_2^2) \left(\Im(\tilde{G}_{\text{res}}^1) - \Im(\tilde{Y}^1) \right) - f_2 (f_j^2 - f_1^2) \left(\Im(\tilde{G}_{\text{res}}^2) - \Im(\tilde{Y}^2) \right) \\ = f_j (f_1^2 - f_2^2) \left(\Im(\tilde{G}_{\text{res}}^j) - \Im(\tilde{Z}^j) \right). \end{aligned} \quad (5.2.51)$$

Note that Eqs. 5.2.44 and 5.2.51 have no dependence on κ_C , which is the next unknown to solve for. They will therefore be used later. One more equation is obtained by setting the expressions 5.2.45 and 5.2.47 equal. This leads to the quartic equation

$$a\kappa_C^4 + b\kappa_C^3 + c\kappa_C^2 + d\kappa_C + e = 0 \quad (5.2.52)$$

with coefficients

$$a = f_2^2 \xi (\tilde{H}^2 + \xi) \zeta^2 \quad (5.2.53)$$

$$b = f_2 (f_2^2 - f_1^2) (\tilde{H}^2 + \xi) \zeta \tilde{I}^2 + f_2^4 (\tilde{H}^2 + 2\xi) \zeta^2 \quad (5.2.54)$$

$$c = f_2^3 (f_2^2 - f_1^2) \zeta \tilde{I}^2 + (f_2^2 - f_1^2)^2 (\tilde{H}^2 + \xi)^2 + f_2^6 \zeta^2 \quad (5.2.55)$$

$$d = 2f_2^2 (f_2^2 - f_1^2)^2 (\tilde{H}^2 + \xi) \quad (5.2.56)$$

$$e = f_2^4 (f_2^2 - f_1^2)^2, \quad (5.2.57)$$

where

$$\zeta = \frac{\tilde{I}^1}{f_1} - \frac{\tilde{I}^2}{f_2}. \quad (5.2.58)$$

To construct a solution, we first define several parameters:

$$\Delta_0 = c^2 - 3bd + 12ae \quad (5.2.59)$$

$$\Delta_1 = 2c^3 - 9bcd + 27b^2e + 27ad^2 - 72ace \quad (5.2.60)$$

$$p = \frac{8ac - 3b^2}{8a^2} \quad (5.2.61)$$

$$q = \frac{b^3 - 4abc + 8a^2d}{8a^3} \quad (5.2.62)$$

$$Q_0 = \sqrt[3]{\frac{\Delta_1 + \sqrt{\Delta_1^2 - 4\Delta_0^3}}{2}} \quad (5.2.63)$$

$$S_0 = \frac{1}{2} \sqrt{-\frac{2}{3}p + \frac{1}{3a} \left(Q_0 + \frac{\Delta_0}{Q_0} \right)}. \quad (5.2.64)$$

The solutions are

$$\kappa_{C,1,2} = -\frac{b}{4a} - S_0 \pm \frac{1}{2} \sqrt{-4S_0^2 - 2p + \frac{q}{S_0}} \quad (5.2.65a)$$

$$\kappa_{C,3,4} = -\frac{b}{4a} + S_0 \pm \frac{1}{2} \sqrt{-4S_0^2 - 2p - \frac{q}{S_0}}. \quad (5.2.65b)$$

Using both reference-model values for A , C , and D from L1 measurements taken on 2019-01-17, as well as real L1 data from 2019-02-02, it was shown using Wolfram Mathematica that the desired solution depends on input values at the time. Therefore, further investigation is needed to find a method to determine how to choose which of the solutions to use at each point in time.

What remains is to solve for the time dependence of the actuation using the remaining 6 equations from 5.2.44 and 5.2.51. At this point, we will make the simplifying approximations that

$$\sin \omega_n \tau_j \approx \omega_n \tau_j \quad (5.2.66)$$

$$\cos \omega_n \tau_j \approx 1. \quad (5.2.67)$$

To justify this approximation, consider the impact at the highest calibration line used to measure the TDCFs, $f_2 \sim 400$ Hz, when the τ_j are the largest they were in O2, $\sim 100 \mu\text{s}$. Even in this most extreme case, errors are $\sim 3\%$, and only at the highest calibration line, where the actuation has a relatively small impact. Moreover, one of the motivating factors for finding this solution is the concern that other time dependence is causing the

computed values of τ_j to deviate from zero, when in reality, they may not deviate much from zero. This method should ensure that the computed τ_j do not stray from zero unless their true values do.

Since the τ_j appear only in the form $e^{i\omega_n\tau_j}$ in Eqs. 5.2.44 and 5.2.51, this will make the remaining 6 equations linear in all unknowns. It is therefore possible to solve for the remaining time dependence computationally in the `gstlal` calibration pipeline using matrix manipulations. The `gstlal-calibration` software package [26] already has an element that can solve such systems. Thus, we wish to find the elements of the matrix \mathbf{M} and the vector \mathbf{V} such that

$$\begin{bmatrix} M_{11} & M_{12} & \dots & \dots & \dots & M_{16} \\ M_{21} & M_{22} & \dots & \dots & \dots & M_{26} \\ \vdots & \vdots & \ddots & & & \vdots \\ \vdots & \vdots & & \ddots & & \vdots \\ \vdots & \vdots & & & \ddots & \vdots \\ M_{61} & M_{62} & \dots & \dots & \dots & M_{66} \end{bmatrix} \begin{bmatrix} \kappa_T \\ \kappa_P \\ \kappa_U \\ \kappa_{T\mathcal{T}T} \\ \kappa_{P\mathcal{T}P} \\ \kappa_{U\mathcal{T}U} \end{bmatrix} = \begin{bmatrix} V_1 \\ V_2 \\ V_3 \\ V_4 \\ V_5 \\ V_6 \end{bmatrix} \quad (5.2.68)$$

In order to have a one-to-one mapping between the indices of the κ_j and τ_j and the indices of \mathbf{M} and \mathbf{V} , we adopt the notation $T \rightarrow 1$, $P \rightarrow 2$, and $U \rightarrow 3$. After some algebraic and trigonometric manipulations, we find that the matrix elements are

$$\begin{aligned} M_{jj} &= \left(\frac{1}{f_1^2} - \frac{1}{f_j^2} \right) \Re(\tilde{G}_{\text{res},j}^2) \\ &+ \left(\frac{1}{f_j^2} - \frac{1}{f_2^2} \right) \Re(\tilde{G}_{\text{res},j}^1) - \left(\frac{1}{f_1^2} - \frac{1}{f_2^2} \right) \left(\Re(\tilde{G}_{\text{res},j}^j) - \Re(\tilde{C}_{\text{res}}^j \tilde{A}_{j,0}^j X^j) \right) \end{aligned} \quad (5.2.69)$$

$$\begin{aligned} M_{jk} &= \left(\frac{1}{f_1^2} - \frac{1}{f_j^2} \right) \Re(\tilde{G}_{\text{res},k}^2) \\ &+ \left(\frac{1}{f_j^2} - \frac{1}{f_2^2} \right) \Re(\tilde{G}_{\text{res},k}^1) - \left(\frac{1}{f_1^2} - \frac{1}{f_2^2} \right) \Re(\tilde{G}_{\text{res},k}^j) \end{aligned} \quad (5.2.70)$$

$$\begin{aligned}
M_{j,j+3} &= -2\pi f_2 \left(\frac{1}{f_1^2} - \frac{1}{f_j^2} \right) \Im(\tilde{G}_{\text{res},j}^2) & (5.2.71) \\
&\quad - 2\pi f_1 \left(\frac{1}{f_j^2} - \frac{1}{f_2^2} \right) \Im(\tilde{G}_{\text{res},j}^1) + 2\pi f_j \left(\frac{1}{f_1^2} - \frac{1}{f_2^2} \right) \left(\Im(\tilde{G}_{\text{res},j}^j) - \Im(\tilde{C}_{\text{res}}^j \tilde{A}_{j,0}^j X^j) \right)
\end{aligned}$$

$$\begin{aligned}
M_{j,k+3} &= -2\pi f_2 \left(\frac{1}{f_1^2} - \frac{1}{f_j^2} \right) \Im(\tilde{G}_{\text{res},k}^2) & (5.2.72) \\
&\quad - 2\pi f_1 \left(\frac{1}{f_j^2} - \frac{1}{f_2^2} \right) \Im(\tilde{G}_{\text{res},k}^1) + 2\pi f_j \left(\frac{1}{f_1^2} - \frac{1}{f_2^2} \right) \Im(\tilde{G}_{\text{res},k}^j)
\end{aligned}$$

$$\begin{aligned}
M_{j+3,j} &= f_2 (f_1^2 - f_j^2) \Im(\tilde{G}_{\text{res},j}^2) & (5.2.73) \\
&\quad + f_1 (f_j^2 - f_2^2) \Im(\tilde{G}_{\text{res},j}^1) + f_j (f_2^2 - f_1^2) \left(\Im(\tilde{G}_{\text{res},j}^j) - \Im(\tilde{C}_{\text{res}}^j \tilde{A}_{j,0}^j X^j) \right)
\end{aligned}$$

$$\begin{aligned}
M_{j+3,k} &= f_2 (f_1^2 - f_j^2) \Im(\tilde{G}_{\text{res},k}^2) & (5.2.74) \\
&\quad + f_1 (f_j^2 - f_2^2) \Im(\tilde{G}_{\text{res},k}^1) + f_j (f_2^2 - f_1^2) \Im(\tilde{G}_{\text{res},k}^j)
\end{aligned}$$

$$\begin{aligned}
M_{j+3,j+3} &= 2\pi f_2^2 (f_1^2 - f_j^2) \Re(\tilde{G}_{\text{res},j}^2) & (5.2.75) \\
&\quad + 2\pi f_1^2 (f_j^2 - f_2^2) \Re(\tilde{G}_{\text{res},j}^1) + 2\pi f_j^2 (f_2^2 - f_1^2) \left(\Re(\tilde{G}_{\text{res},j}^j) - \Re(\tilde{C}_{\text{res}}^j \tilde{A}_{j,0}^j X^j) \right)
\end{aligned}$$

$$\begin{aligned}
M_{j+3,k+3} &= 2\pi f_2^2 (f_1^2 - f_j^2) \Re(\tilde{G}_{\text{res},k}^2) & (5.2.76) \\
&\quad + 2\pi f_1^2 (f_j^2 - f_2^2) \Re(\tilde{G}_{\text{res},k}^1) + 2\pi f_j^2 (f_2^2 - f_1^2) \Re(\tilde{G}_{\text{res},k}^j),
\end{aligned}$$

where $\tilde{G}_{\text{res},j}^n = \tilde{C}_{\text{res}}^n \tilde{D}^n \tilde{A}_j^n$. The components of the vector \mathbf{V} are

$$V_j = \left(\frac{1}{f_1^2} - \frac{1}{f_j^2} \right) \Re(\tilde{Y}^2) + \left(\frac{1}{f_j^2} - \frac{1}{f_2^2} \right) \Re(\tilde{Y}^1) \quad (5.2.77)$$

$$V_{j+3} = (f_1^2 - f_j^2) \Im(\tilde{Y}^2) + f_1 (f_j - f_2) \Im(\tilde{Y}^1). \quad (5.2.78)$$

This solution has not yet been implemented in the `gstlal` calibration pipeline, but it is likely that it will be tested using O3 data. If shown to be effective, it may be implemented at some point during the run. In addition to improvement in accuracy, another advantage

of using this method is increased flexibility of calibration line placement. In particular, this method does not require the lines at f_1 and f_j to be in a ~ 1 Hz frequency band as the method currently implemented does.

5.2.7 Attenuating noise in the computed TDCFs

The TDCFs are computed continuously in the calibration pipelines, whether the detectors are in a nominal low-noise configuration or not. When the detectors are not in a low-noise state, the computed values of the TDCFs are unreliable. It is therefore necessary to implement a method that distinguishes between reliable and unreliable measurements and chooses the most reasonable values of the TDCFs at times when they cannot be computed. In order to distinguish between acceptable and unacceptable measurements, the coherence between the injection channels x_i and error signal d_{err} is measured at each of the calibration lines in the front-end calibration pipeline. After demodulating at a frequency f using a local oscillator, the coherence between two signals $x(t)$ and $y(t)$ is computed using

$$\gamma_{xy}^2(f) = \frac{|\langle \tilde{x}^*(f)\tilde{y}(f) \rangle|^2}{\langle |\tilde{x}(f)|^2 \rangle \langle |\tilde{y}(f)|^2 \rangle}, \quad (5.2.79)$$

where the superscript asterisk denotes complex conjugation and the angled brackets denote averages, which are estimated using a low-pass filter. Coherences are computed using 10-second segments of input data, and $n_d = 13$ independent, consecutive values are then averaged, so that each averaged coherence is based on 130 seconds of input data. The average coherence is used to compute the normalized random error in the magnitude of the transfer function \hat{H}_{xy} at each calibration line frequency:

$$\epsilon \left[\left| \hat{H}_{xy} \right| \right] \approx \sqrt{\frac{1 - \gamma_{xy}^2}{2n_d \gamma_{xy}^2}}, \quad (5.2.80)$$

as derived in [32]. The `gst1al` calibration pipeline reads in this uncertainty from the front end in order to determine whether the TDCFs currently computed are acceptable. Then each computed TDCF is “gated” using the uncertainty at each calibration line used to compute it.

Even when the coherence at the calibration line frequencies is considered acceptable, the noise in the computed time series is enough to contribute significant uncertainty to $h(t)$. This is especially true during the occasional large glitches that corrupt the calculations of the TDCF's. Since none of the TDCF's are observed to change on timescales shorter than a few minutes, a 128-second running median is used to attenuate noise in the time series. A running median reduces the uncertainty of a normally-distributed time series by a factor of only $\sqrt{\pi/2n}$, while a running mean reduces this by a factor $1/\sqrt{n}$. However, a running median is much less sensitive to occasional outliers caused by glitches that would corrupt a running mean. In order to remove the effect of these glitches in the time series, the running median must be long compared to the low-pass filter used for demodulation of the calibration lines, which is 20 s in length. If the coherence of the calibration lines is considered unacceptable, the computed TDCF's entering the running median are replaced with the previously-computed median, so that the output time series stabilizes when the detector exits low-noise state. A 10-second running mean is used after the running median to remove a small amount of high-frequency content left by the running median.

Note that the gating, as well as the running median and mean occur after the TDCF's are computed. This process could be done immediately after the ratios $\tilde{d}_{\text{err}}(f_n)/\tilde{x}_n(f_n)$ are computed at each calibration line. Since lack of coherence in one calibration line does not imply that all of the calibration lines are incoherent, this alternative order of operations would offer the benefit that it does not stop computing the TDCF's just because a single line is incoherent. Additionally, the time series $\tilde{d}_{\text{err}}(f_n)/\tilde{x}_n(f_n)$ is more likely to be normally-distributed than the computed TDCF's. This is particularly true of f_s and Q , whose non-normal distributions are known to lead to systematic errors if not handled with care.² The primary reason that this is done after the TDCF's are computed is because the expected values (based on the static reference model) of the TDCF's are known, while the expected values of $\tilde{d}_{\text{err}}(f_n)/\tilde{x}_n(f_n)$ would need to be computed. The

²For this reason, the gating, running median, and running average are now applied to the parameter $(S_s^{-1}(f_4) - 1)$ before f_s and Q are computed.

expected values are used to produce calibrated data at times when no reliable values of the TDCFs have yet been computed.

When running the `gst1a1` calibration pipeline in low latency, it is important that this method does not add latency, as the length of the running median is much longer than the current calibration latency. Therefore, in low latency, the timestamps of samples exiting the smoothing process are equal to the timestamps of the most recent data entering the smoothing process. Since the TDCFs do not change on such short timescales, this “shift” in timestamps has negligible impact on calibration accuracy. In high latency, since jobs are run in parallel in 4096-second segments, it is advantageous to do the opposite, that is, to assign timestamps to samples exiting the smoothing process equal to the timestamps of the earliest samples in the input array. Otherwise, each time the detector enters a low-noise configuration, the calculation of the TDCFs is delayed, adding an unnecessary few minutes of delay before $h(t)$ is ready for analysis.

This method was used during O2 to attenuate noise in the TDCFs and was shown to be consistently effective. There are therefore no plans to change this for O3.

5.3 Compensating for time dependence in the calibration models

Here, we outline the methods used in the `gst1a1` calibration pipeline to compensate for the parameterized time-dependence in the calibration models. Since O1, it has been possible to compensate for changes in the magnitudes of the sensing and actuation functions. Since O2, new methods have been developed that allow compensation for all known time dependence using adaptive filtering techniques.

5.3.1 Applying scalar corrections to the components of ΔL_{free}

The highest-latency calibration in O1, as well as the low- and high-latency calibration in O2 included compensation for the time dependence of the parameters κ_T , κ_{PU} , and κ_C . Since the calibration pipeline applies separate filters to d_{err} and d_{ctrl} representing the

functions C^{-1} , A_T , A_P , and A_U , compensating for these factors requires only a simple time-domain multiplication:

$$h(t) = \frac{1}{L} \left(\frac{1}{\kappa_C(t)} C^{-1, \text{model}} * d_{\text{err}}(t) + \kappa_T(t) A_T^{\text{model}} * d_{\text{ctrl}}(t) + \kappa_P(t) A_P^{\text{model}} * d_{\text{ctrl}}(t) + \kappa_U(t) A_U^{\text{model}} * d_{\text{ctrl}}(t) \right). \quad (5.3.1)$$

The impact on calibration accuracy of compensating for the scalar factors κ_T , κ_{PU} , and κ_C is shown in [21] and [16].

5.3.2 Compensating for frequency-dependent temporal variations

The content of this section closely follows the discussion in [17].

The highest-latency calibration produced after O2 additionally included compensation for the coupled cavity pole f_{cc} . This was accomplished by applying and periodically updating a short FIR filter to d_{err} that modeled one zero and one pole before the inverse sensing filter was applied:

$$\Delta L_{\text{res}}(t) = \frac{1}{\kappa_C(t)} C^{-1} * \left(\frac{1 + if/f_{cc}(t)}{1 + if/f_{cc}^{\text{model}}} \right) * d_{\text{err}}(t). \quad (5.3.2)$$

Since O2, a more generalized algorithm has been developed that allows the application of an arbitrary number of time-dependent zeros and poles, as well as a time-dependent gain factor and time delay, in the form of an adaptive FIR filter. The adaptive filter therefore has the general form

$$\tilde{\mathcal{F}}_{\text{corr}}(f) = \frac{\prod_m (1 + if/z_m)}{\prod_n (1 + if/p_n)} K e^{2\pi if\tau}, \quad (5.3.3)$$

where z_m and p_n are the frequencies of variable zeros and poles, respectively, K is a variable gain factor, and τ is a variable time advance. All of these components can be read in as a time series computed previously in the pipeline. The zeros and poles can also be read in as constants, which is necessary when dividing out poles or zeros in the model that need to be corrected. It is additionally possible to read in a static filter and convolve it with the time-dependent correction filter, so that the resulting filter is $\mathcal{F} = \mathcal{F}_{\text{corr}} * \mathcal{F}_{\text{static}}$. This became necessary when correcting for the time dependence of f_s

and Q using a short correction filter produced inadequate results, requiring a replacement of the reference-model filter, which is passed to the algorithm as $\mathcal{F}_{\text{static}}$.

This new algorithm makes it possible to additionally include the time-dependence of f_s and Q in the inverse sensing filter. The procedure used to compensate for all the time dependence of the inverse sensing filter is as follows:

1. Take a mean of the computed values of $\kappa_C(t)$, $f_{cc}(t)$, $f_s(t)$, and $Q(t)$ for a time set by the user. Currently, the averaging of these values in the `gstlal` calibration pipeline prior to updating the filter is sufficient, and no additional averaging is necessary.
2. In the frequency domain, compute the correction filter

$$\tilde{C}_{\text{corr}}^{-1}(f; t) = \frac{1}{\kappa_C(t)} \frac{1 + if/f_{cc}(t)}{1 + if/f_{cc}^{\text{model}}} \times \frac{f^2 + f_s^2(t) - if f_s(t)/Q(t)}{f^2 + (f_s^{\text{model}})^2 - if f_s^{\text{model}}/Q^{\text{model}}}. \quad (5.3.4)$$

In the frequency domain, the length of the correction filter is one more than half the length of the static time-domain filter $C^{-1, \text{model}}$.

3. Add a delay to the filter of half the length of the filter to ensure that the resulting time-domain filter is centered in time. This is done by negating every other value in the frequency-domain filter, starting after the DC component and ending before the Nyquist component. This is equivalent to multiplying each frequency-domain value by $e^{-\pi i f \tau_{\text{filt}}}$, where τ_{filt} is the temporal duration of the time-domain filter.
4. Take the inverse Fourier transform of the frequency-domain filter to produce a time-domain filter equal in length to the static filter $C^{-1, \text{model}}$.
5. Convolve the correction filter with the static filter to produce the updated inverse sensing filter

$$C^{-1} = C^{-1, \text{corr}} * C^{-1, \text{model}}. \quad (5.3.5)$$

The resulting filter has a length one sample less than twice the length of the static reference-model filter. In order to preserve manageable calibration latency and computational cost, the additional coefficients at the beginning and end of the filter are removed.

6. Apply a Tukey window to the time-domain FIR filter so that it falls off smoothly at the edges. (It may be beneficial to use a Kaiser window instead, for the reasons noted in Section 4.2.1.)
7. Pass the updated filter to an algorithm that applies FIR filters and smoothly handles filter updates by using half of a Hann window to taper out the old filter and bring in the new filter [33]. During a transition of duration t_{trans} beginning at t_0 , the output is therefore

$$\Delta L_{\text{res}}(t) = \cos^2\left(\frac{\pi}{2} \cdot \frac{t - t_0}{t_{\text{trans}}}\right) C_{\text{old}}^{-1} * d_{\text{err}}(t) + \sin^2\left(\frac{\pi}{2} \cdot \frac{t - t_0}{t_{\text{trans}}}\right) C_{\text{new}}^{-1} * d_{\text{err}}(t). \quad (5.3.6)$$

A drawback of this method is that it degrades the quality of the high-pass filter included in the inverse sensing filter by removing filter coefficients at the edges of the convolved filter and applying another window. The impact of this is reduced by the use of the additional high-pass filter in the inverse sensing path (see Fig. 12). In principle, a filter with only 4 coefficients can be used to compensate for all known time dependence in the inverse sensing function, which consists of only a time-dependent gain and three time-dependent zeros (f_{cc} and two zeros for SRC detuning). Such a method would require using a static inverse sensing filter with dependence on the three zeros removed so that they could be handled separately. Such a method is currently being developed for use later during O3, the primary challenge being due to small errors in phase that will need to be corrected. This method would not only improve high-pass filtering, it would also significantly reduce computational cost, since the adaptive inverse sensing filter is the most computationally expensive process in the `gstlal` calibration pipeline.

A similar procedure is used to compensate for all known time dependence in each component of actuation function. However, since the high-pass filters in the actuation path are combined with the model filters to minimize latency, it is necessary to correct for time dependence using short correction filters that are separate. Otherwise, the corruption of the high-pass filters contained in each actuation path would lead to an unacceptable increase in low-frequency noise. Since the only time-dependent parameters in the A_j are a variable gain and a variable time delay, the time-dependent actuation

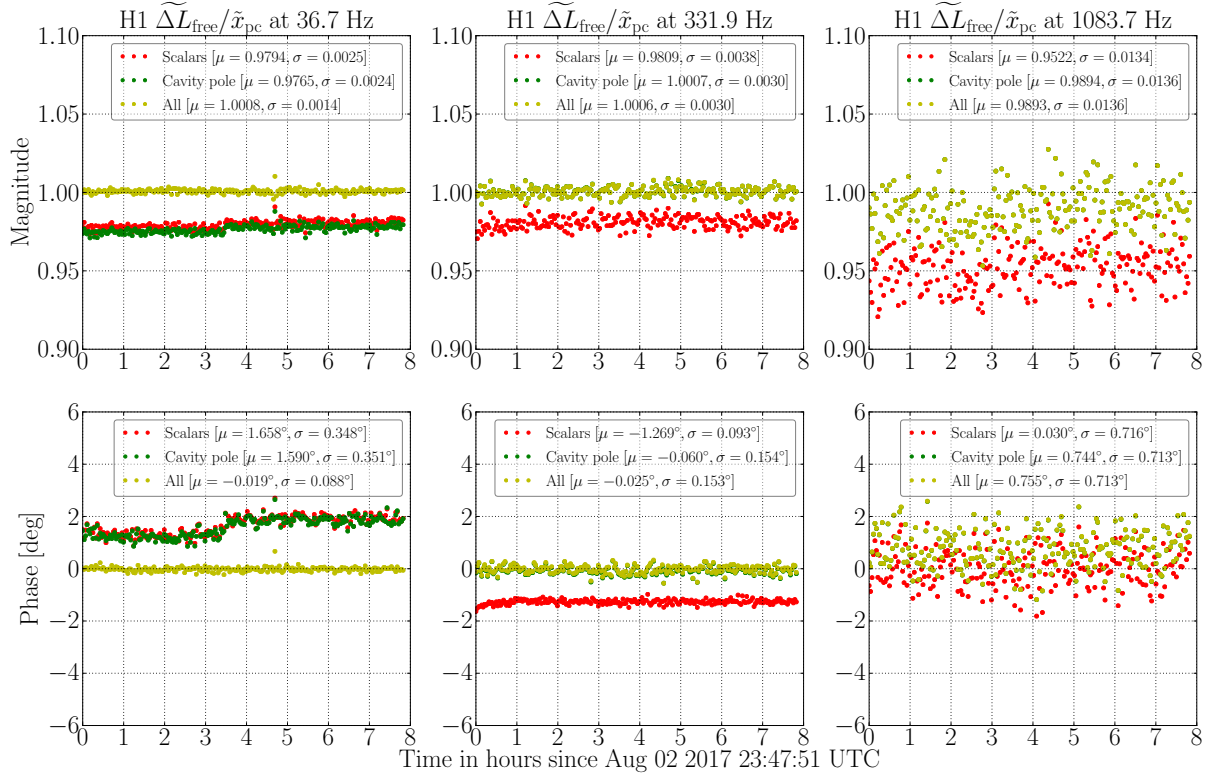


Figure 16 : The ratio $\widetilde{\Delta L}_{\text{free}}(f)/\tilde{x}_{\text{pc}}(f)$ at three Pcal line frequencies for three versions of calibrated data for H1. 128 seconds of ΔL_{free} data and x_{pc} data were demodulated before taking the ratio to produce each point. The red points (labeled “Scalars”) represent calibrated data that was corrected for the time dependence of κ_{T} , κ_{PU} , and κ_{C} , requiring no filter updates. The green points (labeled “Cavity pole”) show improved accuracy resulting from additionally compensating for time-dependence in f_{cc} . The yellow points (labeled “All”) show the most accurate calibration, produced by compensating for all known time-dependence.

corrections $\kappa_j e^{-2\pi i f \tau_j}$ are modeled using linear-phase FIR filters (see Fig. 8 and Fig. 9).

5.3.3 Impact of compensating for time dependence on calibration accuracy

We now wish to assess the impact on calibration accuracy of compensating for temporal variations in the TDCF’s, especially frequency-dependent variations that require periodic updates to the calibration filters. Since the Pcal is used as the reference for fundamental displacement calibration, the success of the methods used to compensate for time dependence is best evaluated by comparison of $h(t)$ to the Pcal. The Pcal lines injected through x_{pc} provide a way to continuously monitor the accuracy of the calibration at the Pcal line frequencies. Fig. 16 shows the ratio $\widetilde{\Delta L}_{\text{free}}(f)/\tilde{x}_{\text{pc}}(f)$ for H1 data during O2

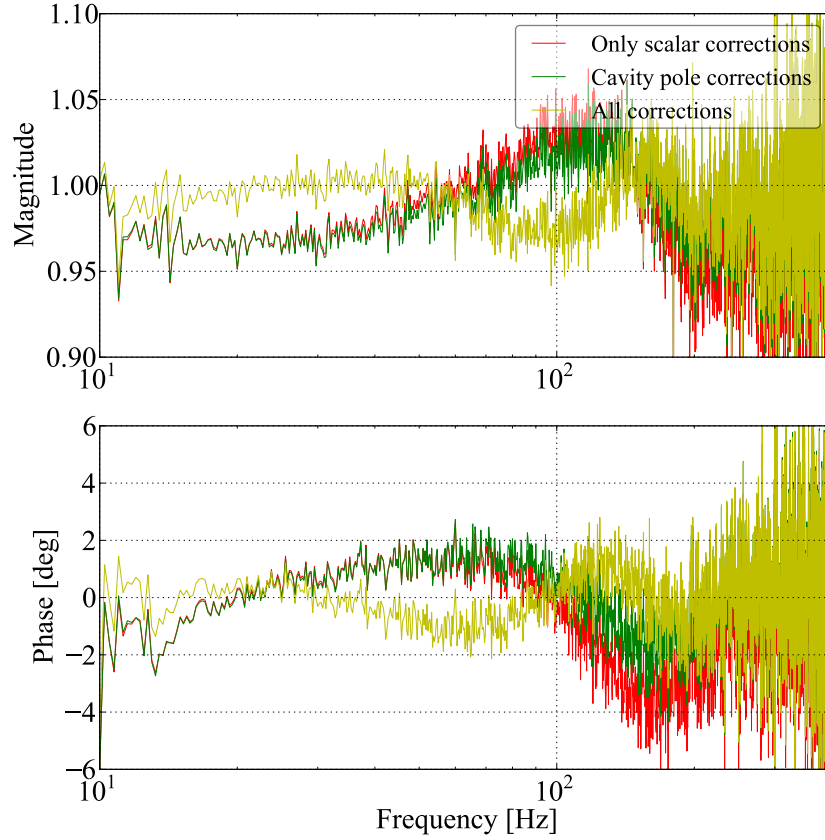


Figure 17 : The transfer function $\widetilde{\Delta L}_{\text{free}}(f)/\widetilde{x}_{\text{pc}}(f)$ computed for three versions of calibrated data for H1. Each transfer function was produced from 250 seconds of data during a Pcal broadband injection on 2017-08-16. The red trace (labeled “Only scalar corrections”) represent calibration that was corrected for time-dependence in κ_T , κ_{PU} , and κ_C . The green trace (labeled “Cavity pole corrections”) is from a calibration that additionally compensated for time-dependence in f_{cc} . The yellow trace (labeled “All corrections”) is from a calibration that compensates for all known time-dependence.

at three calibration line frequencies in the detection band. For calibrated data that is accurate relative to the Pcal, this ratio is expected to have a magnitude close to unity and a phase close to zero. 128 seconds of data were used to compute each point, in order to avoid correlation between points caused by the 128 s running median that is applied to the TDCFs. Systematic errors of a few percent in magnitude and a few degrees in phase are seen at all three frequencies in the calibrated data that is only corrected for the time dependence of the scalar factors κ_T , κ_{PU} , and κ_C . As expected, additionally compensating for the time dependence of the coupled cavity pole f_{cc} improves calibration accuracy at the two higher frequencies, leaving negligible error at $f_2 = 331.9$ Hz and errors of only $\sim 1\%$ and 1° at $f_3 = 1083.7$ Hz. The remaining $\sim 2\%$ and 2° of systematic

error at $f_1 = 36.7$ Hz can be removed by compensating for the time dependence of the τ_j , f_s , and Q . Note the sudden shift in the phase of $\widetilde{\Delta L}_{\text{free}}(f_1)/\tilde{x}_{\text{pc}}(f_1)$ present in the first two versions of calibration. This was coincident with sudden changes in the values of the τ_j , and compensating for the time dependence of τ_j is shown to remove this unwanted shift.

In addition to monitoring the calibration at the Pcal line frequencies over long periods of time, it is possible to measure calibration accuracy across a range of frequencies below 1kHz using broadband injections made using the Pcal. Pcal broadband injections are made on an occasional basis during observing runs in order to check the accuracy of the calibration model across the detection band. Unfortunately, it is not possible to measure the TDCF's during a broadband injection due to the fact that the Pcal lines must be turned off during broadband injections. Fig. 17 shows the transfer function $\widetilde{\Delta L}_{\text{free}}(f)/\tilde{x}_{\text{pc}}(f)$ computed during a Pcal broadband injection lasting 250 seconds, comparing the same three versions of calibrated data. Noise increases with frequency due to the difficulty of injecting DARM motion at higher frequencies. It is therefore difficult to assess the impact of compensating for the time dependence of f_{cc} using a broadband injection. The impact of compensating for time dependence in τ_j , f_s , and Q can be seen to result in an improvement below ~ 50 Hz. Due to the lack of ability to compute the TDCF's during and just before the injection, the applied values of the TDCF's were estimated based on data from about 2 hours earlier (the following low-noise data occurred more than 2 hours later). There is therefore a possibility that the true values of the TDCF's deviated slightly from the applied values. This is especially true of κ_C , which was observed to be varying that day by $\sim 5\%$ on timescales of a few hours.

Chapter 6

Subtraction of excess noise from the calibrated signal

The goal of computing the strain signal in the Advanced LIGO detectors is to calibrate GW signals. However, the majority of the content of the calibrated $h(t)$ signal does not come from GWs, but from various sources of noise. Some of these noise sources, such as the shot noise that dominates at high frequencies, cannot be distinguished from GWs due to the fact that they are only measured in DARM. Other sources of noise can be measured by other witness sensors that are not sensitive to GWs. Such witness sensors have been successfully used to subtract excess noise from $h(t)$ in high latency, significantly increasing detector sensitivity [3, 34, 35]. After O2, an offline noise subtraction pipeline written in Python was used to subtract spectral lines and broadband noise over the entirety of the run [3]. This had an especially significant impact at H1, where excess motion in the laser beam contributed significant measureable noise to the $h(t)$ spectrum. Removal of this noise was shown at many times to increase H1's total detectable volume for binary neutron star inspirals by a factor of 2.

Since O2, a method for subtraction of persistent spectral lines and broadband noise has been developed in the `gstlal` calibration pipeline. Perhaps the most significant benefit of including broadband noise subtraction in the `gstlal` calibration pipeline is the resulting ability to provide noise-subtracted $h(t)$ data in very low latency. A second benefit is that

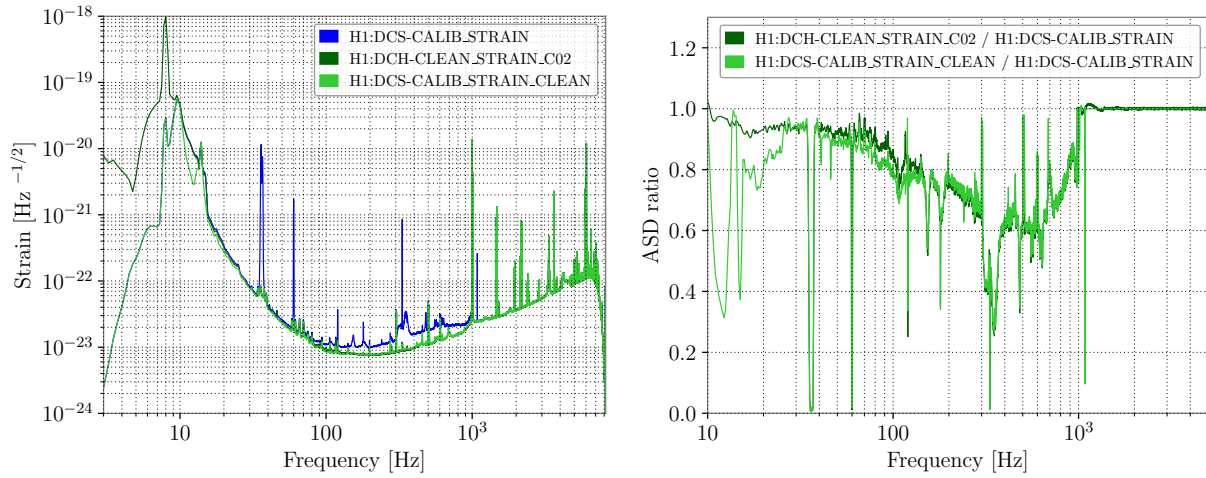


Figure 18 : Comparison of the three amplitude spectral densities computed from 8192 s of data around the time of the event GW170817. The channel DCS-CALIB_STRAIN contains $h(t)$ data produced in high latency. DCH-CLEAN_STRAIN_C02 was produced in high latency after O2 by subtracting spectral lines and broadband noise. Similar subtraction methods have since been developed in the `gstlal` calibration pipeline to produce the channel DCS-CALIB_STRAIN_CLEAN.

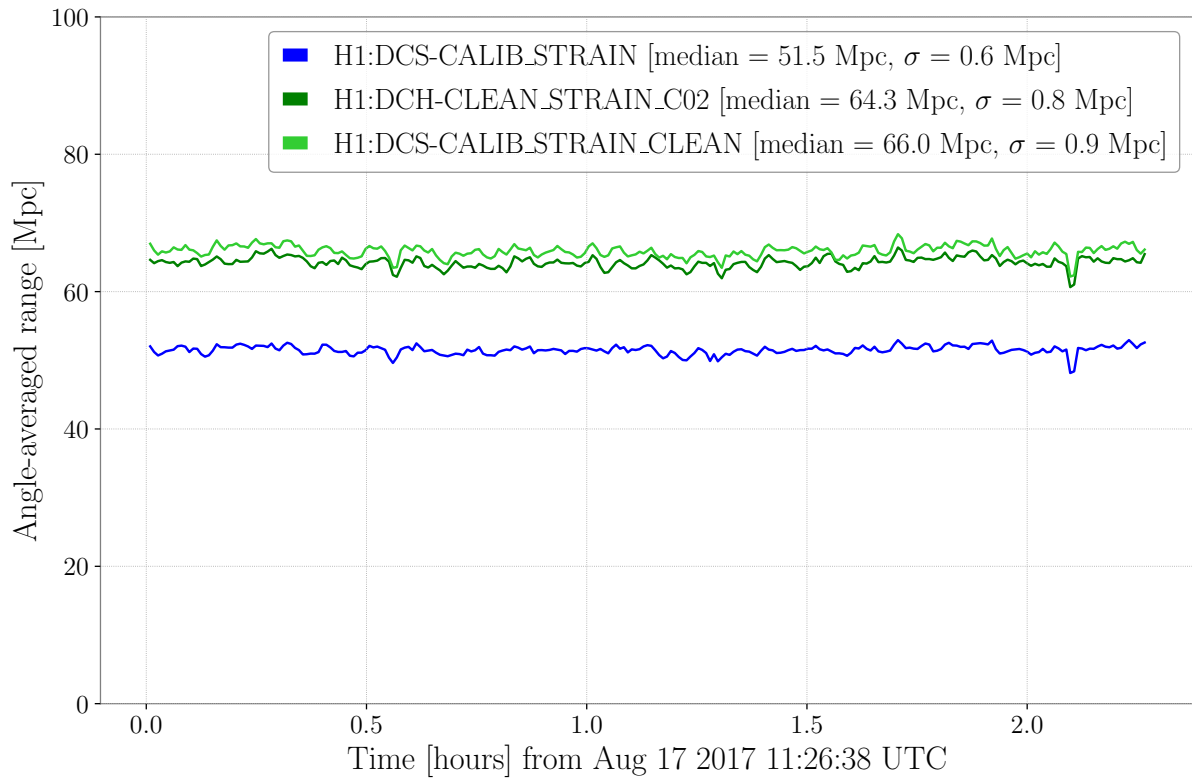


Figure 19 : Angle-averaged binary neutron star inspiral range computed from 8192 s of data around the time of the event GW170817, comparing three data sets. The noise subtraction in the `gstlal` calibration pipeline (DCS-CALIB_STRAIN_CLEAN) accounts for a 210% increase in total detectable volume.

this method does not require the production of a new set of GW frame files; the cleaned $h(t)$ data is included in the GW frame files as they are produced. Preliminary results show that this subtraction pipeline can provide cleaned data similar to that produced in high latency after O2, with negligible impact on latency. Fig. 18 shows a comparison of the calibrated $h(t)$ data without subtraction, the cleaned $h(t)$ data produced after O2, and the noise subtraction done in the `gstlal` calibration pipeline, around the time of the binary neutron star merger GW170817. Noise reduction in `gstlal` cleaned data is similar to that produced after O2 above ~ 100 Hz, with improved reduction below ~ 100 Hz. This is primarily due to the fact that the O2 noise subtraction team elected not to use angular and length sensing control witness channels that couple to low-frequency noise, due to the fact that these did not have a large impact throughout the run. Also note that the high-pass filtering shown here has improved since O2, which may impact noise subtraction at low frequencies. The impact of the noise subtraction on the inspiral range (the average distance at which a binary neutron star system with each mass equal to $1.4 M_{\odot}$ can be computed with a signal-to-noise ratio of 8, as computed by `GWpy` [36]) during the same time is shown in Fig. 19, where the subtraction in the `gstlal` calibration pipeline accounts for a 210% increase in total detectable volume at H1. Preliminary results shortly prior to O3 indicate a smaller impact, contributing an increase in detectable volume for the H1 detector of $\sim 5\%$.

6.1 Subtraction of calibration lines

Removal of loud spectral lines is not only useful for downstream data analysis such as searches for continuous waves and the GW stochastic background, it is also beneficial for the subtraction of broadband noise to follow. Loud lines that are present in the $h(t)$ signal but not in the broadband noise witness sensors corrupt the calculation of transfer functions between witness channels and $h(t)$ at their frequencies, leading to the injection of noise around those lines.

To subtract calibration lines injected using the `Pcal` and the actuators at each stage,

the `gst1a1` calibration pipeline measures the amplitude and phase of the calibration lines in the injections channels x_{pc} , x_T , x_P , and x_U , and it then computes the corresponding sinusoidal excitation expected to occur in $h(t)$. The Pcal lines are therefore subtracted under the assumption that the computed $h(t)$ is accurate relative to the Pcal. The steps used to subtract Pcal lines are:

1. Demodulate the Pcal channel x_{pc} at the frequency of the calibration line being subtracted. Letting $x_{pc}(t) = a \cos(\omega t - \phi) + n(t)$, where ω , a , and ϕ are the angular frequency, amplitude, and phase of the calibration line, respectively, and $n(t)$ is noise, the result of the demodulation is the factor $(a/2)e^{-i\phi}$.
2. Convert this factor from counts in \tilde{x}_{pc} to meters in $\Delta\tilde{L}_{free}$. Note that the first two steps are often already done to compute the TDCFs, in which case it is possible to save computational cost by using the previous result.
3. Reconstruct a sinusoid to be subtracted from $h(t)$:

$$\Re\left(2e^{i\omega t} \times \frac{a}{2}e^{-i\phi}\right) = a \cos(\omega t - \phi). \quad (6.1.1)$$

4. Subtract from $h(t)$.

Pcal lines could also be subtracted by applying an FIR filter to x_{pc} to convert it from counts to meters at all frequencies and then subtracting all the lines at once. The reason for using the method is to save computational cost, especially in light of the fact that two of the three lines that are normally subtracted are already demodulated to compute the TDCFs.

The method used to subtract actuator lines from $h(t)$ is the same except that the conversion from counts to meters is time-dependent, due to fluctuations in the actuation strength. A demodulated factor $(a_j/2)e^{-i\phi_j}$, where $j \in \{T, P, U\}$, and a_j and ϕ_j are the amplitude and phase as measured in the injection channel x_j , is converted from counts to meters using

$$\frac{a}{2}e^{-i\phi} = \kappa_j e^{-i\omega_j \tau_j} a_j \times \frac{a_j}{2}e^{-i\phi_j} \quad (6.1.2)$$

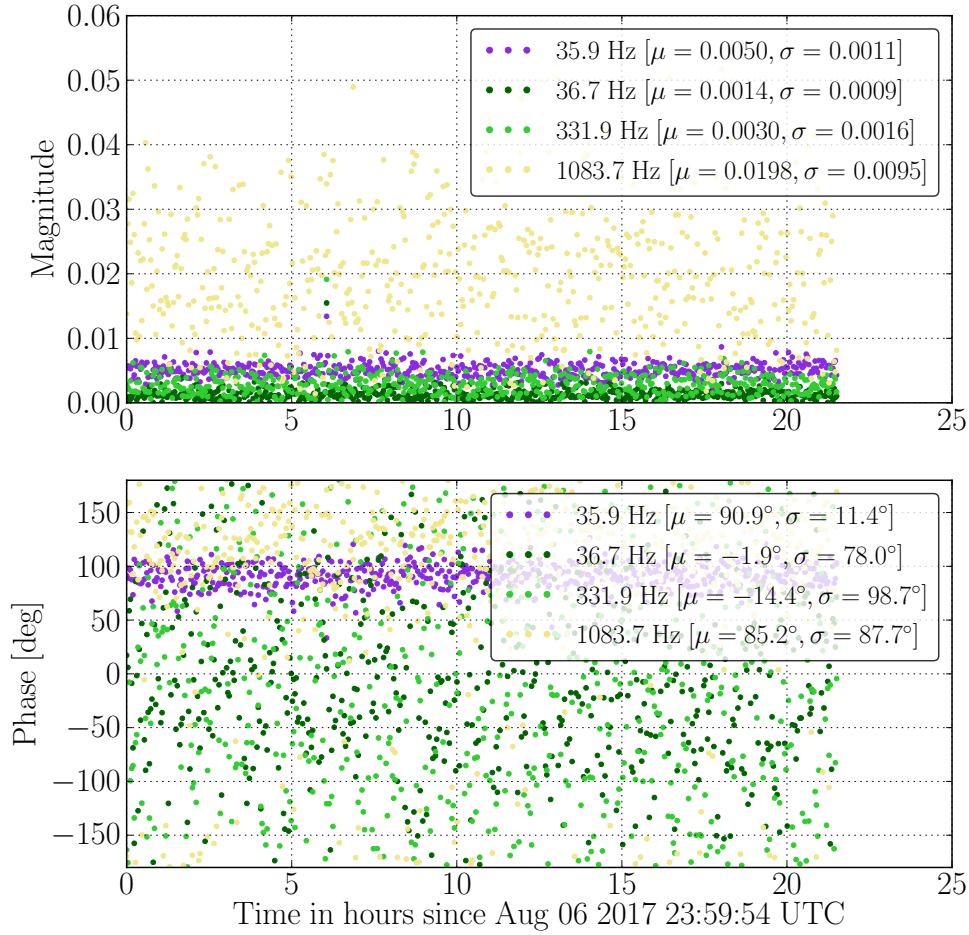


Figure 20 : A time series of the ratio $\tilde{h}_{\text{clean}}(f)/\tilde{h}(f)$ at the calibration line frequencies at H1 during O2. $h(t)$ and $h_{\text{clean}}(t)$ were demodulated using a 10-second low-pass filter, and the ratios were averaged for 128 seconds to produce each point. Three pcal lines are shown at frequencies $f_1 = 36.7$ Hz, $f_2 = 331.9$ Hz, and $f_3 = 1083.7$ Hz. The electrostatic drive actuator line at $f_T = 35.9$ Hz is also shown. These were all the visible calibration lines in the detection band during O2.

Note that the time-dependent calibration model is used to construct the actuator injections to be subtracted from $h(t)$. In addition to saving computational cost using the fact that these lines have already been demodulated to compute the TDCFs, this can offer the benefit of applying the same time-dependent compensations to the line subtraction that is applied to correct $h(t)$. Since much effort has been dedicated to compensating for time dependence in the calibration, and since the TDCFs computed by the `gstlal` calibration pipeline were shown to be stable and well-behaved throughout O2, we suggest that this method is a stable and safe way to subtract calibration lines, with very little risk of impacting GWs in the $h(t)$ signal.

For both Pcal lines and actuator lines, this method relies on the accuracy of the time-dependent calibration model. It therefore can provide a continuous check of calibration accuracy at the calibration lines; in other words, systematic errors in the calibration will reduce the effectiveness of the subtraction.

The performance of the calibration line subtraction is shown over ~ 22 hours of H1 data during O2 in Fig. 20. The ratio $\tilde{h}_{\text{clean}}(f)/\tilde{h}(f)$ is shown at each of the calibration line frequencies. The lower reduction of the line height of the Pcal line at f_3 is likely due in part to the fact that this line has a lower signal-to-noise ratio than the others, but lower calibration accuracy may also contribute. The clustering of the phase of $\tilde{h}_{\text{clean}}(f_T)/\tilde{h}(f_T)$ around 90° is evidence of a small systematic error in the calibration, possibly originating from the computed value of κ_T or τ_T .

At times when the calibration model is believed to be unreliable, the calibration lines can be subtracted using the same method that is used to subtract additional spectral lines, described in the next section.

6.2 Subtraction of additional spectral lines

In addition to calibration lines, the $h(t)$ spectrum also contains other spectral lines, such as 60-Hz power mains lines and harmonics, whose amplitude and phase can be estimated from correlated noise in witness sensors. Unlike the case for the calibration lines, the transfer functions between these witness sensors and $h(t)$ are not thoroughly studied to produce an accurate time-dependent calibration model. Moreover, such lines are generally much less stable than calibration lines, with frequent fluctuations in amplitude and frequency.

The general method used in the `gstlal` calibration pipeline to subtract spectral lines allows the use of multiple witness channels, in order to subtract as much noise as possible.¹ The steps in the process are described below:

1. Demodulate $h(t)$ and each witness channel w_n at the expected frequency of the line

¹So far, the best results have been obtained using only one witness channel, but the general method is described for completeness.

to be subtracted. If there are multiple line frequencies (e.g., harmonics) in a single witness channel to be subtracted, w_n is demodulated at each frequency separately, and steps 1-4 are done for each frequency.

2. Take the ratios $\tilde{h}(f)/\tilde{w}_n(f)$ and \tilde{w}_m/\tilde{w}_n .
3. Take a running median and a running average of the above ratios. Currently, only a 128-second running median is used.
4. Due to the fact that different witness sensors may detect the same noise, care must be taken to avoid subtracting the same signal from $h(t)$ multiple times. To accomplish this, we find “optimized” transfer functions T_n by solving the matrix equation

$$\begin{bmatrix} 1 & \frac{\tilde{w}_2}{\tilde{w}_1} & \dots & \frac{\tilde{w}_N}{\tilde{w}_1} \\ \frac{\tilde{w}_1}{\tilde{w}_2} & 1 & \dots & \frac{\tilde{w}_N}{\tilde{w}_2} \\ \vdots & \vdots & \ddots & \vdots \\ \frac{\tilde{w}_1}{\tilde{w}_N} & \frac{\tilde{w}_2}{\tilde{w}_N} & \dots & 1 \end{bmatrix} \begin{bmatrix} T_1 \\ T_2 \\ \vdots \\ T_N \end{bmatrix} = \begin{bmatrix} \frac{\tilde{h}}{\tilde{w}_1} \\ \frac{\tilde{h}}{\tilde{w}_2} \\ \vdots \\ \frac{\tilde{h}}{\tilde{w}_N} \end{bmatrix} \quad (6.2.1)$$

at the frequencies of the spectral lines. In order to prevent large errors in these transfer functions, the values of the transfer functions are updated only when the detector is in a nominal low-noise configuration.

5. As shown in Fig. 21, fluctuations of about ± 0.03 Hz are observed in the fundamental frequency of the power mains. In general, the low-pass filter used in demodulating $h(t)$ and the witness channels is not centered in time (this is necessary in low latency, for instance). Deviations in the true frequency of the line being subtracted from the expected frequency would therefore cause a phase error in the sinusoid that is constructed in the next step if this were not compensated for. To correct this in the power mains subtraction, the fundamental frequency of the power mains, expected to be ~ 60 Hz, is tracked continuously. The algorithm that tracks the frequency does so by measuring the temporal separation between times when the witness-channel signal crosses zero, measured using linear interpolation. The number of half-cycles to use for each measurement is set by the user, and the output is averaged to remove

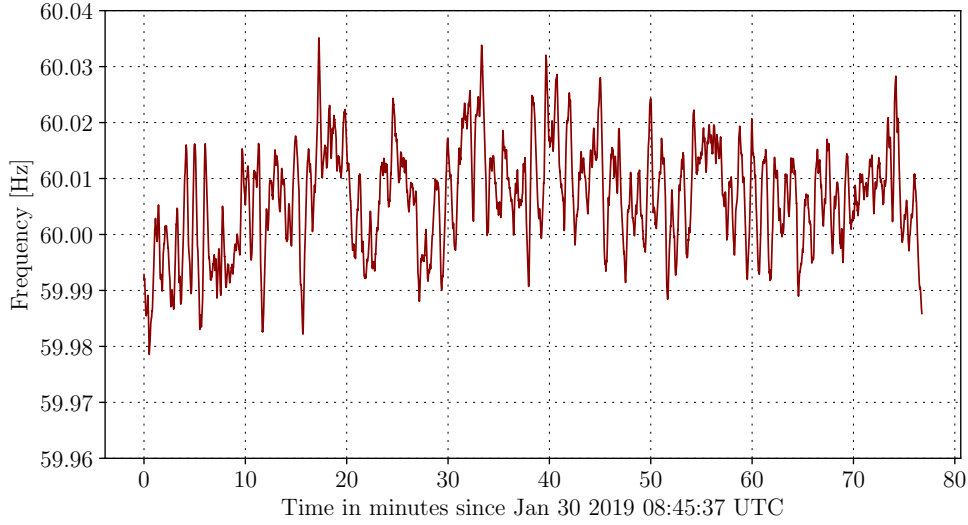


Figure 21 : A time series of the power mains fundamental frequency over time, as measured by the `gstlal` calibration pipeline.

any “kinks” from the resulting time series. This provides a computationally cheap and accurate measure of frequency with a very fast response to changes over time. It assumes, however, that the line being measured in the signal is loud compared to all other components of the signal. If this is not the case, a short band-pass filter can be used before measurement. The deviation of the measured frequency from the expected frequency is then used to produce corrective phase factors ϕ_{corr} to be applied to the transfer functions T_n . For the case of power mains lines, the measured fundamental frequency is used to compute a corrective phase factor for each harmonic.

6. The spectral lines are then reconstructed and subtracted from $h(t)$ using

$$h_{\text{clean}}(t) = h(t) - \sum_j \sum_n \Re(e^{i\omega_j t} \times \phi_{\text{corr},j} T_n(f_j) \tilde{w}_n(f_j)) , \quad (6.2.2)$$

where the f_j are the expected frequencies of the lines being subtracted using a set of witness channels w_n .

In general, this can be done using multiple sets of witness channels that detect different spectral lines.

The performance of the power mains line subtraction is shown in Fig. 22 using the

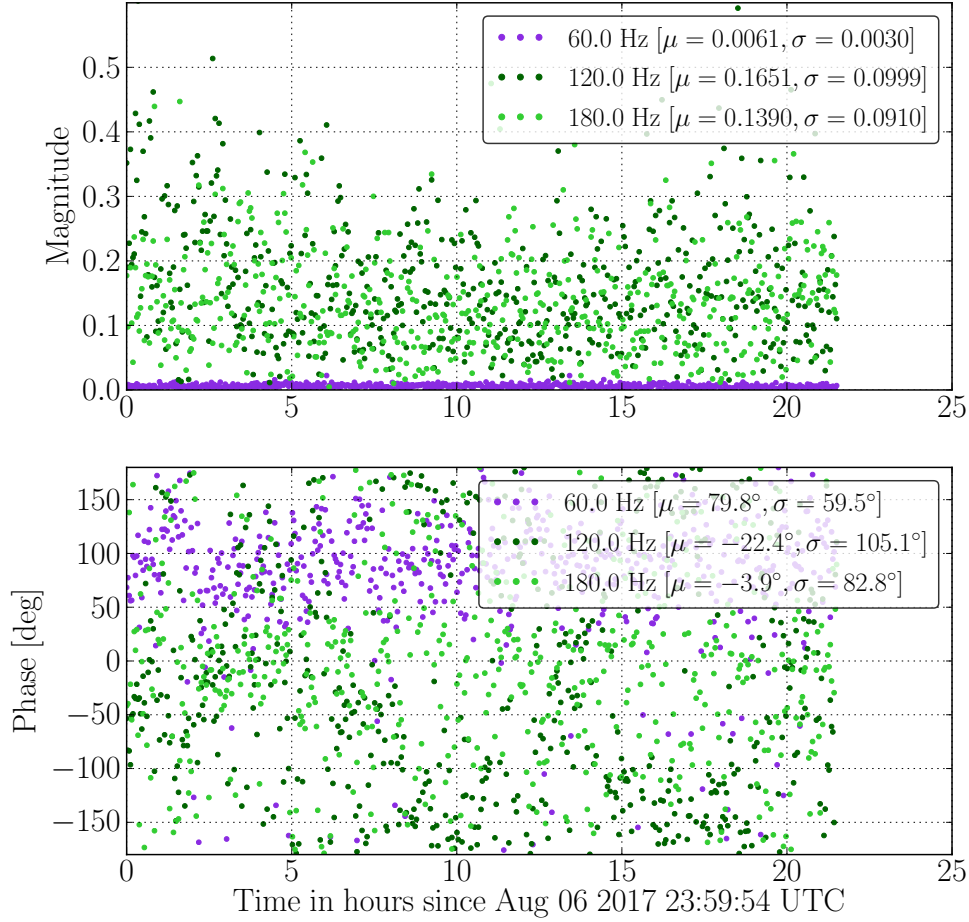


Figure 22 : A time series of the ratio $\tilde{h}_{\text{clean}}(f)/\tilde{h}(f)$ at 60 Hz and harmonics, showing the performance of the power mains line subtraction over time. $h(t)$ and $h_{\text{clean}}(t)$ were demodulated using a 10-second low-pass filter, and the ratios were averaged for 128 seconds to produce each point.

same H1 data as was used in Fig. 20. The ratio $\tilde{h}_{\text{clean}}(f)/\tilde{h}(f)$ is shown at the first 3 harmonics of the fundamental frequency $f_1 = 60$ Hz. The next 2 harmonics are also subtracted in the `gstlal` calibration pipeline, but the impact is increasingly smaller with each harmonic due to the fact that the higher harmonics are not as loud in the $h(t)$ spectrum.

6.3 Subtraction of broadband noise in the `gstlal` calibration pipeline

Witness sensors and other auxiliary channels can also be used to subtract broadband noise from the $h(t)$ signal, if they contain correlated noise and are insensitive to GWs. During

O2 at H1, jitter in the laser beam contributed significant noise from 100 Hz to 1kHz. To measure this noise, a set of three split photodiodes was installed to measure beam motion and fluctuations in beam size [35]. Each photodetector has a center photodiode, and three photodiodes of equal size arranged in a ring around the center photodiode. Control of the length of the cavities and angular motion of the mirrors also contributed noise at frequencies below a few tens of Hz. The digital control signals sent to the actuators are used to subtract this noise.

The methods developed in the `gstlal` calibration pipeline to subtract broadband noise in $h(t)$ assume that the noise in the witness channels is linearly coupled to $h(t)$ and that it is stationary on the tens-of-minutes timescales typically used to compute transfer functions between these witness sensors and $h(t)$.

6.3.1 Computing transfer functions

The first step necessary to subtract noise contributions from the chosen witnesses from the $h(t)$ signal is to estimate transfer functions that minimize the RMS of the signal

$$\tilde{h}_{\text{clean}}(f) = \tilde{h}(f) - \sum_n T_n(f) \tilde{w}_n(f). \quad (6.3.1)$$

We begin by applying short Hann windows to time-domain $h(t)$ data and witness channel data and taking Fourier transforms to compute $\tilde{h}(f)$ and $\tilde{w}_n(f)$ for each segment of data. Each window is overlapped with the previous window by half the length of the window so as to weight each moment in time equally while still avoiding edge effects. Any frequency bands that are known beforehand to have loud spectral lines in $h(t)$ that are not present in the witness channels are then smoothed over by replacing the Fourier transforms with straight lines in those bands. If this is not done, the transfer functions computed later may have errors around the frequencies of loud lines due to the large amount of noise in the transfer functions at those frequencies. The ratios $\tilde{h}(f)/\tilde{w}_n(f)$ and $\tilde{w}_m(f)/\tilde{w}_n(f)$ are then taken from the DC component to the Nyquist frequency of the witness channels for each windowed segment of data separately. Median values of these ratios are taken at all frequencies, in order to reduce noise in the transfer functions.

In order to achieve the desired temporal duration for the FIR filters produced later, these ratios are then resampled using a windowed sinc table. This allows the flexibility of being able to average over noise in the time domain using a median or in the frequency domain. The use of a median instead of a mean in the time domain is important, as it renders the result insensitive to occasional outliers due to, e.g., large short-duration glitches in the $h(t)$ data. The ability to smooth the transfer functions in the frequency domain also has benefits, especially for cases in which witness channels are highly correlated. In this case, the matrix in Eq. 6.3.2 is ill-conditioned, and the solutions for the transfer functions can have large noisy fluctuations over frequency.

In the current configuration used in the low-latency `gstlal` calibration pipeline, 1000 4-second Fourier transforms are taken over a total time of 2002 seconds used to compute the median values of each ratio. The length of the FIR filters is 1 second, meaning that the ratios $\tilde{h}(f)/\tilde{w}_n(f)$ and $\tilde{w}_m(f)/\tilde{w}_n(f)$ are downsampled by a factor of 4.

Similar to the case for the subtraction of spectral lines discussed in Section 6.2, witness channels used in broadband noise subtraction often are correlated to one another, and it is therefore necessary to find optimized transfer functions T_n by solving

$$\begin{bmatrix} 1 & \frac{\tilde{w}_2}{\tilde{w}_1} & \dots & \frac{\tilde{w}_N}{\tilde{w}_1} \\ \frac{\tilde{w}_1}{\tilde{w}_2} & 1 & \dots & \frac{\tilde{w}_N}{\tilde{w}_2} \\ \vdots & \vdots & \ddots & \vdots \\ \frac{\tilde{w}_1}{\tilde{w}_N} & \frac{\tilde{w}_2}{\tilde{w}_N} & \dots & 1 \end{bmatrix} \begin{bmatrix} T_1 \\ T_2 \\ \vdots \\ T_N \end{bmatrix} = \begin{bmatrix} \frac{\tilde{h}}{\tilde{w}_1} \\ \frac{\tilde{h}}{\tilde{w}_2} \\ \vdots \\ \frac{\tilde{h}}{\tilde{w}_N} \end{bmatrix}, \quad (6.3.2)$$

this time at each frequency in the transfer functions. To insure accuracy in each estimate of the optimized transfer functions, new Fourier transforms are computed only when the detector is in a nominal low-noise configuration.

6.3.2 Producing and updating FIR filters for witness channels

The optimized transfer functions T_n can be applied to the witness channels w_n to subtract their noise contributions from $h(t)$ as described by Eq. 6.3.1. In order to do this in the `gstlal` calibration pipeline, they must be used to produce FIR filters to be applied to the witness channels. To do this, we first apply any high- or low-pass filters by rolling the T_n

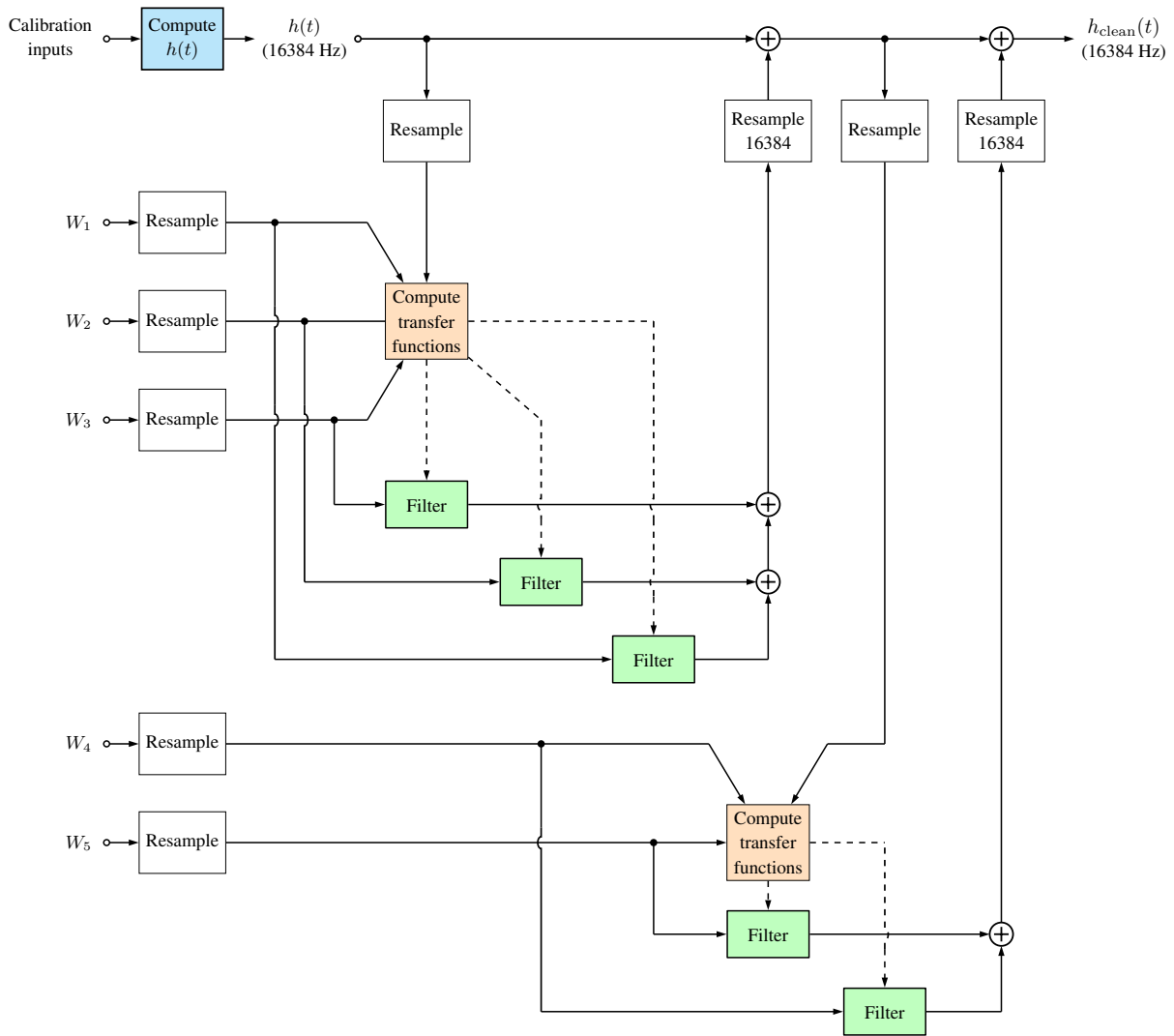


Figure 23 : An example showing the workflow of broadband noise subtraction in the `gstlal` calibration pipeline. Solid lines represent the flow of time series data, while dashed lines represent the periodic passing of FIR filters from elements that compute them to elements that apply them. In this example, two iterations of noise subtraction are done, the first processing three witness channels in parallel, and the second processing two witness channels in parallel. The block labeled “Compute $h(t)$ ” represents the primary component of the `gstlal` calibration pipeline described in Ch. 3 and in Figs. 8 and 9.

off in the frequency domain. Currently, a high-pass filter with a 10-Hz corner frequency is applied to prevent the addition of any noise in $h(t)$ below 10 Hz. A delay of half the length of the filter is then added in order to center the filter in time, making it non-causal. Then an inverse Fourier transform is taken to produce a time-domain FIR filter. The edges of the filter are smoothed off using a Tukey window in the time domain. These filters are sent to a filtering algorithm that smoothly handles filter updates by windowing

out the output of the previous filter using half of a Hann window while windowing in the output of the new filter over some transition time set by the user. These filters are updated each time a new set of transfer functions is computed from a new data set.

If desired, multiple iterations of noise subtraction can be done, i.e., after subtracting noise from $h(t)$ using one set of witness channels, another set of witness channels can be used to do additional cleaning. It is important to note that, in order to avoid subtracting the same signal multiple times, transfer functions produced for later iterations of noise subtraction must be computed using cleaned $h(t)$ data from previous iterations of subtraction. Results from the noise subtraction in the `gstlal` calibration pipeline have shown benefits from processing witness channels together using Eq. 6.3.2 primarily when those witness channels measure noise in the same frequency band. For sets of witness channels that do not measure noise in the same frequency band, results were improved by subtracting noise computed from those witness channels using separate iterations of the noise subtraction in series, thus reducing the size of the matrix of Eq. 6.3.2 in each iteration. The subtraction done using H1 data from O2 shown in this section used two iterations of cleaning, starting with 7 witness sensors used to detect beam jitter from ~ 100 Hz to 1kHz, followed by 7 control signals for angular motion and length control, contributing noise below ~ 100 Hz. Fig. 23 shows an example of the noise subtraction in the `gstlal` calibration pipeline in the form of a block diagram.

6.3.3 Low-latency and high-latency noise subtraction

Several key differences exist between the methods used in low latency versus those used in high latency. In the low-latency `gstlal` calibration pipeline, the noise subtraction is configured so as to not add any latency to the $h(t)$ data stream. The FIR filters being applied to witness channels are therefore computed using previous data, leading to possible concerns about the time-dependence of the transfer functions. Results seen so far indicate that temporal variations are slow enough that updating the transfer functions about once per hour is sufficient to achieve effective subtraction.

In low latency, transfer functions are computed as soon as possible once the detector

enters a low-noise state, if it has been a sufficiently long time (as determined by the user) since the last low-noise state. Additionally, two previous transfer functions are stored at all times: one based on the most recent data, and one based on the beginning of the current or most recent low-noise stretch. The reasoning behind this is that we expect the transfer functions at the beginning of a low-noise state to be more similar to ones computed at the beginning of the previous low-noise state than they are to the most recently computed transfer functions.

Unlike low-latency noise subtraction, high-latency noise subtraction can be done using FIR filters computed from a given segment of data to subtract noise from the same segment of data. This constitutes a slight improvement over the low-latency noise subtraction, since the transfer functions are known to drift with time. The high-latency noise subtraction needs to be done using many 4096-second jobs run in parallel, and it is therefore important that the end of each 4096-second chunk of cleaned strain data is continuous with the beginning of the next 4096-second chunk of cleaned strain data. In order to accomplish this, it is necessary to compute the same transfer functions at the end of a job as those computed at the beginning of the next job. As an example of how this can be done, consider the case of using 1024 s of data to compute each set of transfer functions. During a 4096-second job, 5 sets of these transfer functions need to be produced, requiring an extra 512 s of raw data before the beginning and after the end of the 4096-second job, plus any additional time needed to produce the uncleaned strain data. To ensure that the transfer functions computed from a segment of data are independent of start time, transfer functions are computed from predetermined time intervals set by the user and separated by 1024 s. If the full 1024 s is not available during the job, the transfer functions will not be computed for that cycle. Only data during low-noise states will be used, regardless of how much or how little low-noise data is available during the predetermined 1024-second time window.

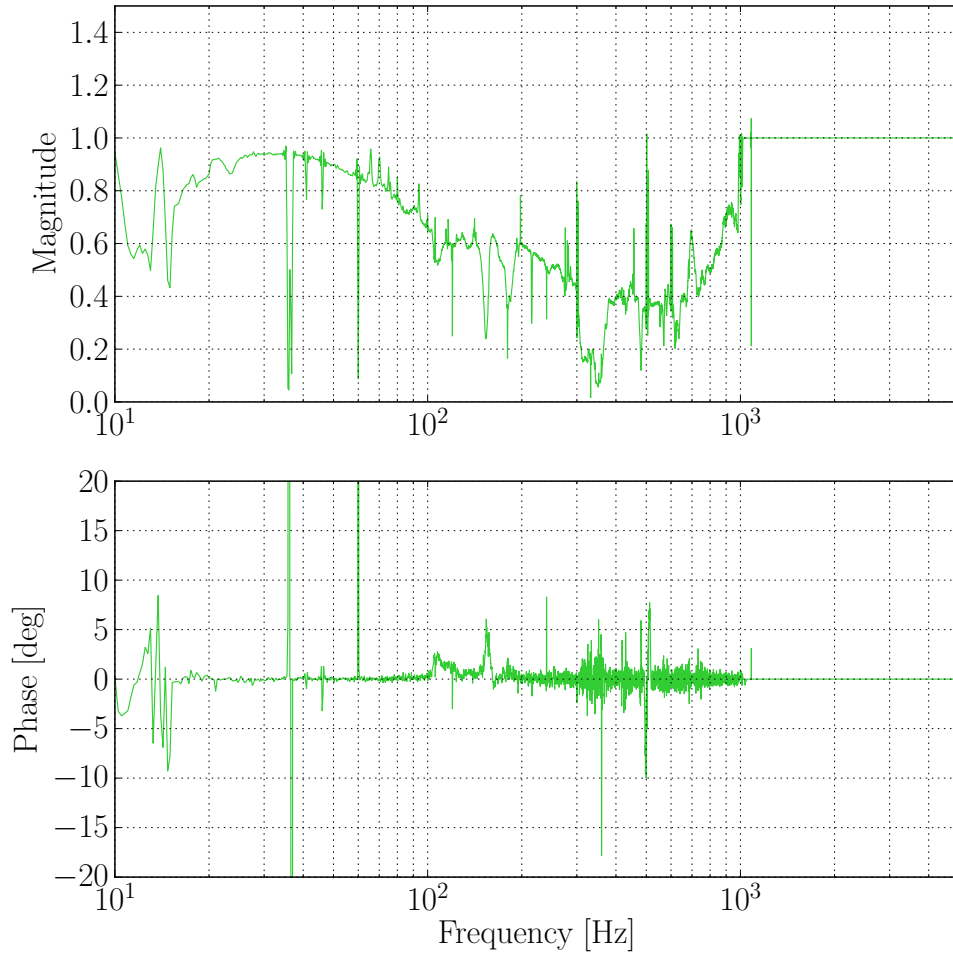


Figure 24 : The transfer function $\tilde{h}_{\text{clean}}(f)/\tilde{h}(f)$ computed using ~ 22 hours of H1 data on August 7, 2017. Fourier transforms of 16-second chunks of overlapped Hann-windowed data were used to compute the ratio $\tilde{h}_{\text{clean}}(f)/\tilde{h}(f)$, and the median of this ratio was taken over 22 hours. Slight deviations of the phase of this transfer function from 0° indicate drifts in the phase of the linear transfer functions between witness channels and $h(t)$ that are not captured by the `gst1a1` calibration pipeline.

6.3.4 Stability over time

As mentioned previously, the transfer functions relating the witness channel data to $h(t)$ are known to vary over time. This can be shown by making numerous plots of each transfer function at different times, but here we wish to use a diagnostic based on final results and requiring only one plot. Fig. 24 shows the transfer function $\tilde{h}_{\text{clean}}(f)/\tilde{h}(f)$ computed from ~ 22 hours of H1 data during O2. Assuming consistently effective broadband noise subtraction, we expect that the magnitude of the transfer function plotted to be less than one and the phase to be consistent with zero. At times when the phases of the transfer

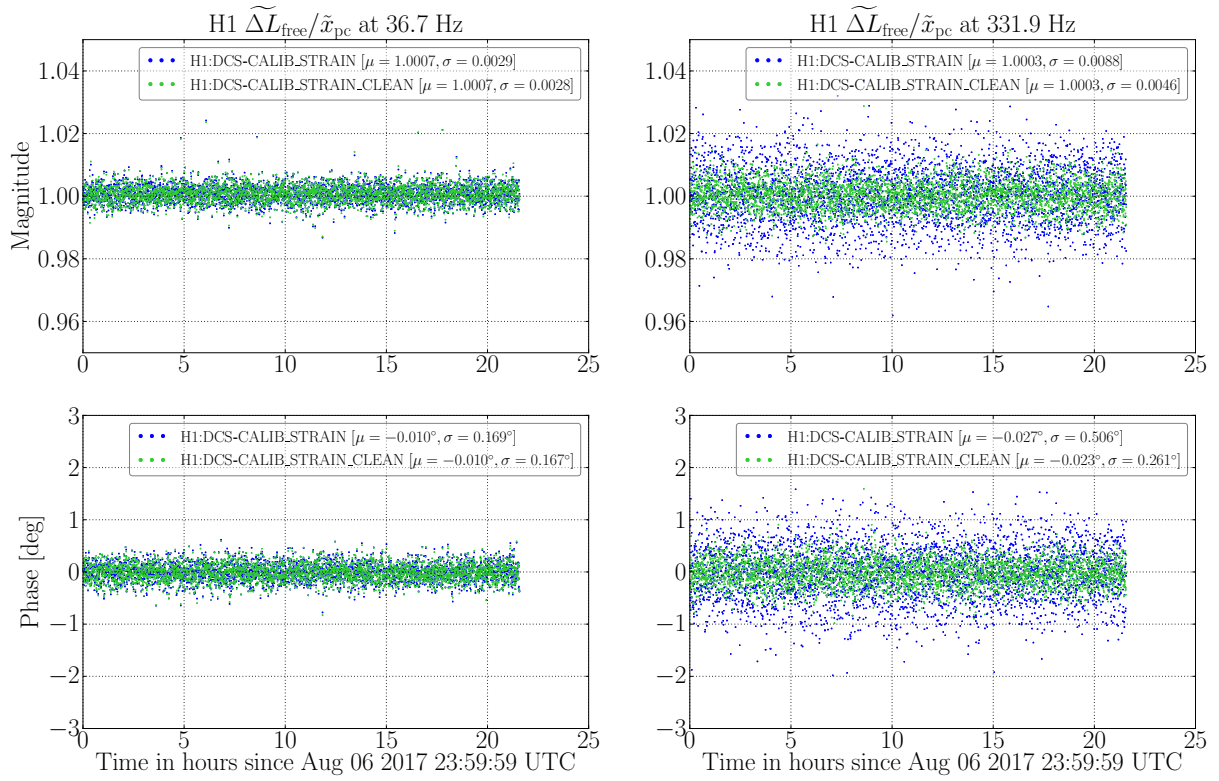


Figure 25 : A time series over 22 hours of H1 data during O2 of the ratio $\widetilde{\Delta L}(f)/\tilde{x}_{pc}(f)$ at the two Pcal lines in the frequency band impacted by broadband noise subtraction. Each ratio was taken using 20 s of demodulated data. The average values of the ratios are unaffected, but noisy fluctuations are reduced, especially in the Pcal line at $f_2 = 331.9$ Hz.

functions between w_n and $h(t)$ drift, the phase of the plotted transfer function deviates from zero. This effect is seen to a small degree below ~ 15 Hz, indicating that the transfer functions are changing at low frequencies. However, the variations are not significant enough to cause the noise subtraction to add noise to $h(t)$.

6.3.5 Impact on calibration accuracy and uncertainty

Although noise subtraction impacts the calibration of the noise we attempt to remove, it is not expected to impact the accuracy of the calibration of GW signals, since the witness sensors used are insensitive to GWs. To test the impact of broadband noise subtraction on calibration accuracy, the Pcal lines can be left unperturbed in the $h(t)$ spectrum while broadband noise is subtracted. Then the Pcal lines, like GWs, are insensitive to the subtraction. Fig. 25 shows time series of the ratio $\widetilde{\Delta L}(f)/\tilde{x}_{pc}(f)$ at the two Pcal line

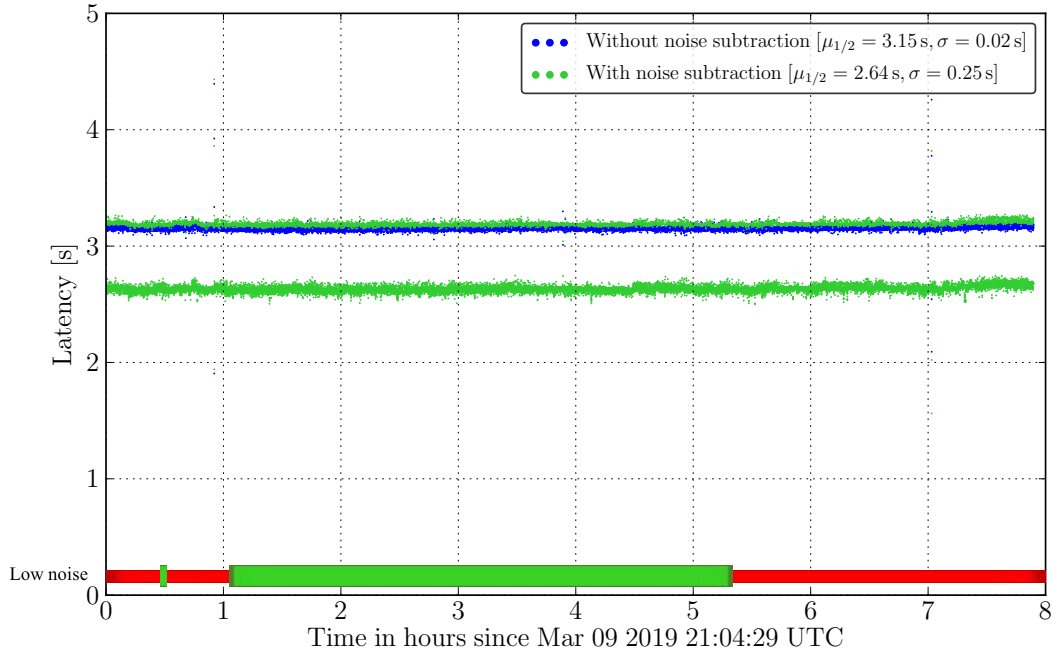


Figure 26 : A time series over 8 hours of H1 data showing the latency of the calibration pipeline with and without noise subtraction. The latencies were computed by measuring the difference in the time that calibrated data exited the pipeline and the time that raw data with the same timestamp entered the pipeline. The median latency $\mu_{1/2}$ and standard deviation σ are shown for each data set in the legend. An anomalous bimodal distribution of latencies and an associated decrease in the median latency is seen when using the noise subtraction. The bar at the bottom indicates times when the detector was in a nominal low-noise state (green) and when it was not (red).

frequencies at which the noise subtraction has an impact. ~ 22 hours of uncleaned and cleaned H1 strain data were used. Each ratio was taken using 20 s of demodulated data. This integration time is short enough to ensure that the contribution of detector noise is large compared to that of the noise in the time-dependent calibration model, which is correlated over the 128-second length of the running median used for the TDCF's. As expected, the data shows no significant change in the average values of the demodulated ratios caused by the noise subtraction. However, noisy fluctuations in the ratio decreases significantly in the Pcal line at $f_2 = 331.9$ Hz, where the noise subtraction has a large impact.

6.3.6 Impact on calibration latency

Since the noise subtraction in the `gstlal` calibration pipeline is done in parallel to the calibration of $h(t)$ data and the filters used for noise subtraction are shorter than the calibration filters, adding noise subtraction to the calibration pipeline's procedure is not expected to significantly increase calibration latency. Moreover, the noise subtraction uses numerous threads when running, allowing the computational cost to be divided between many CPUs, reducing any risk of a buildup of latency due to computational cost. Fig. 26 shows a time series comparison of calibration latency with and without noise subtraction. The latencies were computed by measuring the difference in the time that calibrated data exited the pipeline and the time that raw data with the same timestamp entered the pipeline. The Hanford computing cluster was used for this test, since such tests could interfere with $h(t)$ production if done on the DMT machines. Recent latencies seen in the production pipelines on the DMTs are consistent with these results. An anomalous bimodal distribution of latency and an associated decrease in median latency is seen when using the noise subtraction. The cause of this is unknown, but the median latency of the cleaned strain data is more consistent with what is expected based on the length of the calibration filters.

Chapter 7

Impact of calibration accuracy and noise subtraction on astrophysical analyses

Estimation of source parameters of GW events associated with compact binary coalescences is impacted by both systematic errors in the calibration and noise in the detectors. To assess the impact on parameter estimation caused by the improvements in calibration accuracy discussed in Chapter 5 and the subtraction of spectral lines and broadband noise discussed in Chapter 6, a brief study was done using two GW events from O2 data: the binary black hole merger GW170814 and the binary neutron star merger GW170817.

7.1 Methods of the study

For the study, 8192 s of data was calibrated around the time of each event. Four different sets of calibrated strain data were produced, with:

1. No compensation for any time dependence. This calibration simply relies on the static reference model, produced months earlier.
2. Compensation for the time dependence of the scalar correction factors κ_T , κ_{PU} , and κ_C . The low-latency calibration during O2 was produced with these corrections.

3. Compensation for the time dependence of the scalar correction factors and the coupled cavity pole f_{cc} . A high-latency calibrated strain data set was produced shortly after O2 similar to this, called the C02 calibration.
4. Compensation for all known time dependence, as discussed in Chapter 5. This is the first production of such an accurate calibration for either of the events.

Each of these calibrated data sets contains both strain data without noise subtracted and strain data with noise subtracted. These four data sets were compared to the noise-subtracted high-latency strain data set produced shortly after O2, the “cleaned C02” data. The cleaned C02 data was produced by compensating for time dependence in the scalar correction factors and the coupled cavity pole f_{cc} , similar to the third data set in the above list. A high-latency noise subtraction was done after the production of the high latency $h(t)$ data to produce the cleaned C02 data. Each of these strain data sets was analyzed using a nested sampling algorithm provided by LAL [28] to estimate parameters based on the strain data from the two Advanced LIGO detectors. Data from the Virgo detector was not used for this study. For the binary neutron star event GW170817, the sky localization was fixed at the location of the electromagnetic counterpart.

7.2 Time dependence and parameter estimation

In general, the results presented here show that compensating for time dependence in the calibration has a small impact on the estimation of source parameters of a single event.

7.2.1 GW170814

Fig. 27 shows four skymaps with the estimated locations of GW170814 for each of the four calibration configurations produced in this study. Differences between each are distinguishable by eye. Probability distributions and cumulative distributions of the luminosity distance d_L are shown in Fig. 28, additionally including the cleaned C02 data. Interestingly, the calibration produced that includes compensation for all time dependence is in

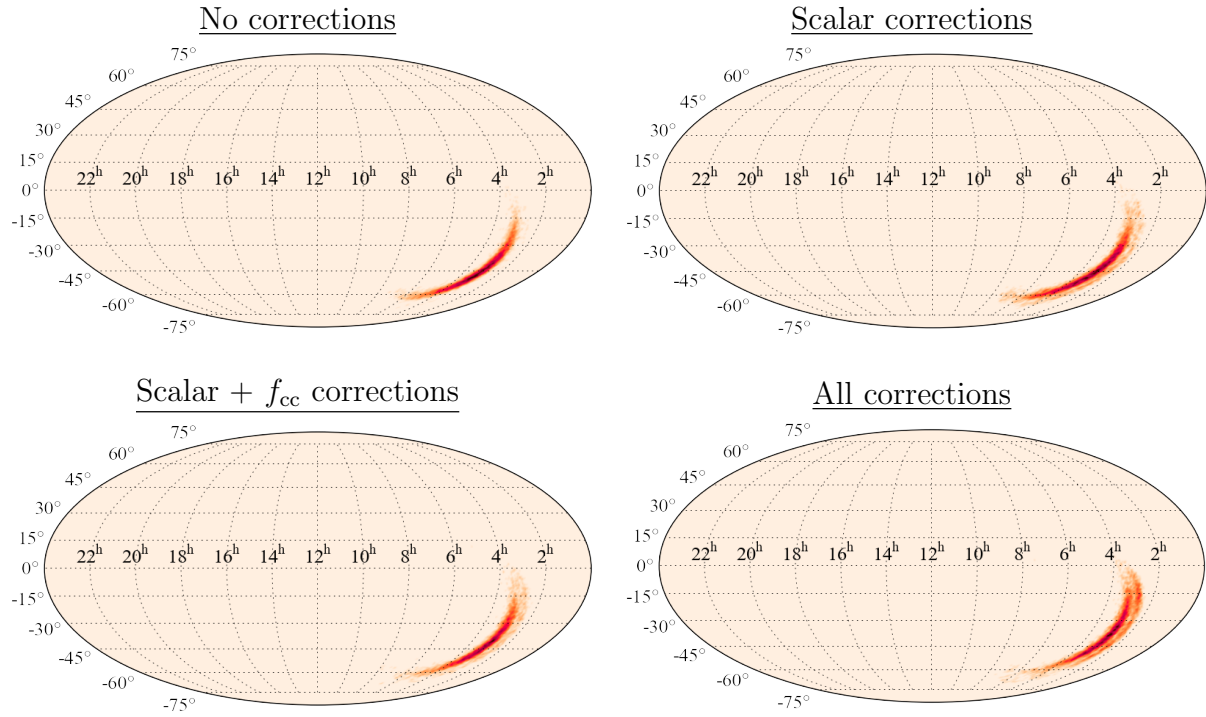


Figure 27 : Skymaps produced by LAL parameter estimation software showing the estimated location of the binary black hole merger GW170814, comparing four different calibration configurations. The upper left plot was produced without compensating for any time dependence. The upper right plot was produced by compensating for the scalar factors κ_T , κ_{PU} , and κ_C . The lower left plot was produced by additionally compensating for the time dependence of the coupled cavity pole f_{cc} . The lower right plot was produced by compensating for all known time dependence. Spectral lines and broadband noise were subtracted from all $h(t)$ data, in order to better resolve differences.

closer agreement with the cleaned C02 data than that which compensated for time dependence in scalar factors and f_{cc} as was done to produce the C02 data. This may be due to small differences in the subtraction of broadband noise, as is seen in Fig. 18. Fig. 29 shows probability distributions and cumulative distributions of the chirp mass \mathcal{M} of the system in the detector frame. Chirp mass is defined by

$$\mathcal{M} = \frac{(m_1 m_2)^{3/5}}{(m_1 + m_2)^{1/5}}, \quad (7.2.1)$$

where m_1 and m_2 are the component masses of each object in a binary system. The significance of chirp mass is that it is the only combination of masses that appears in both the amplitude and phase of the lowest order term in the post-Newtonian expansion of a gravitational waveform produced by a compact binary system. It is therefore possible to estimate it with better accuracy than either of the component masses. Again, small differences are seen between different calibration configurations, but none of these

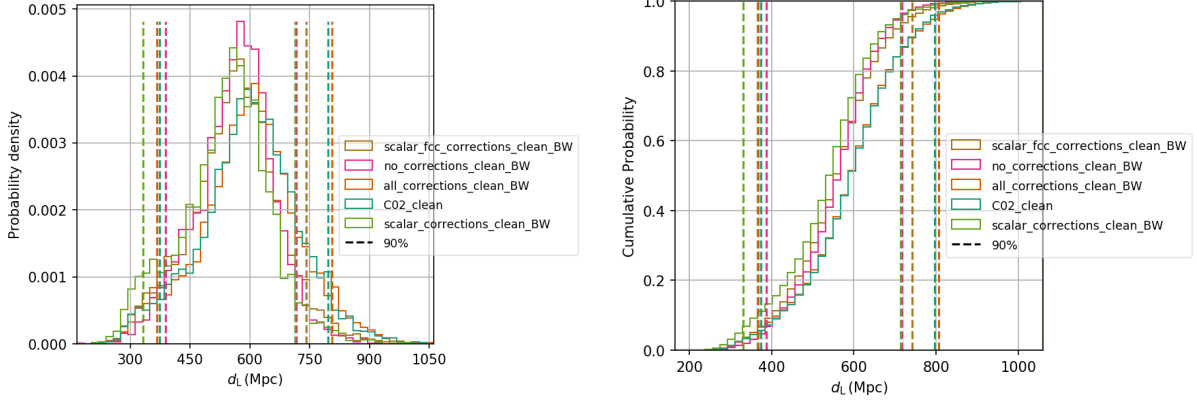


Figure 28 : Probability distributions and cumulative distributions of luminosity distance d_L for GW170814, comparing 5 versions of calibration with: no compensation for time dependence; corrections for scalar factors; corrections for scalar factors and f_{cc} ; compensation for all known time dependence; high-latency calibration produced just after O2 (C02). Spectral lines and broadband noise were subtracted from all data sets.

differences are large compared to the uncertainty in the measurement of chirp mass.

Fig. 30 shows similar plots for the symmetric mass ratio η , which is defined by

$$\eta = \frac{m_1 m_2}{(m_1 + m_2)^2}. \quad (7.2.2)$$

Since the symmetric mass ratio does not appear in the lowest order term in the waveform, it is more difficult to measure than the chirp mass, but accurate measurements of both η and \mathcal{M} would allow for accurate estimates of the component masses. η can take on values from 0 to 1/4, with 1/4 corresponding to equal-mass binary systems, and values near 0 corresponding to an extreme mass ratio. Fig. 31 is a related plot showing the 90% confidence region in m_1 - m_2 parameter space in the detector frame. Results are shown for average values of matched filter signal-to-noise ratio (SNR) and the log-likelihood $\ln \mathcal{L}$ (natural logarithm of the likelihood that the observed signal is an artifact of noise), and average values and standard deviations of \mathcal{M} (detector frame), η , and d_L in Table 4. Subtraction of spectral lines and broadband noise was used for all data sets except for one, labeled “All_noclean.”

7.2.2 GW170817

The L1 calibrated data from the binary neutron star inspiral GW170817 required additional processing due to a loud glitch present in the data about a second before the time

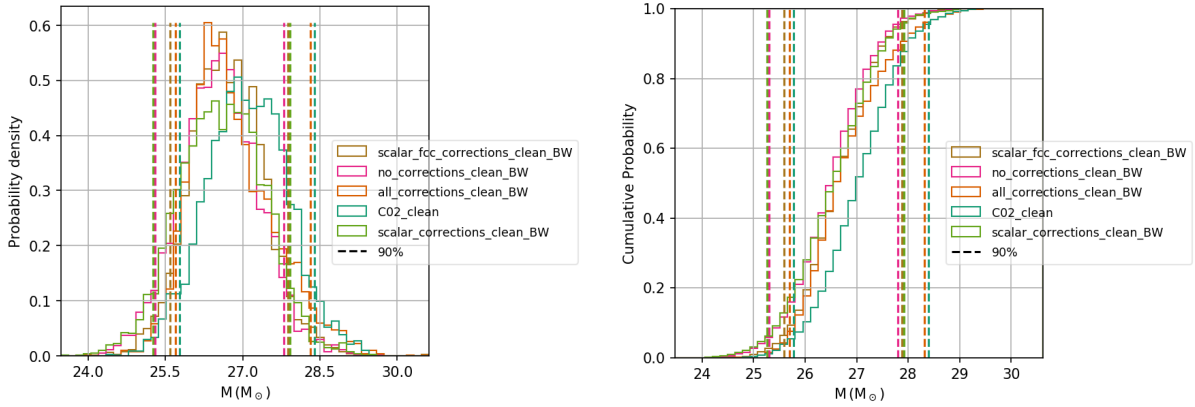


Figure 29 : Probability distributions and cumulative distributions of chirp mass \mathcal{M} for GW170814 in the detector frame, comparing 5 versions of calibration with: no compensation for time dependence; corrections for scalar factors; corrections for scalar factors and f_{cc} ; compensation for all known time dependence; high-latency calibration produced just after O2 (C02). Spectral lines and broadband noise were subtracted from all data sets.

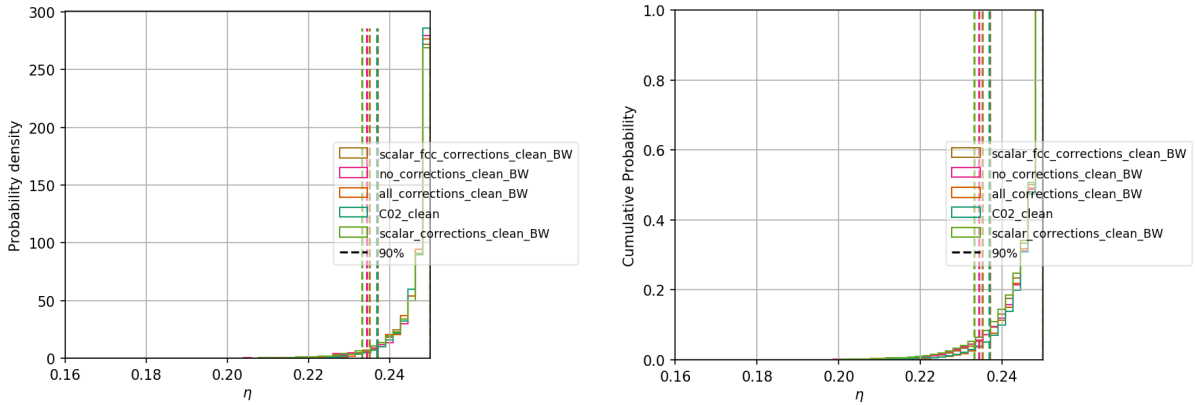


Figure 30 : Probability distributions and cumulative distributions of symmetric mass ratio η for GW170814, comparing 5 versions of calibration with: no compensation for time dependence; corrections for scalar factors; corrections for scalar factors and f_{cc} ; compensation for all known time dependence; high-latency calibration produced just after O2 (C02). Spectral lines and broadband noise were subtracted from all data sets.

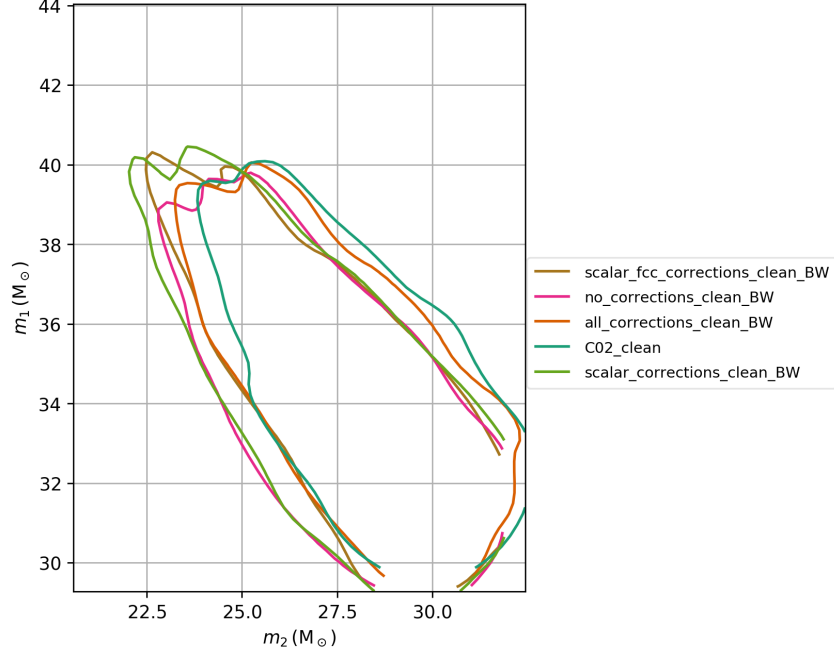


Figure 31 : 90% confidence regions in m_1 - m_2 parameter space (detector frame) for GW170814, comparing 5 versions of calibration with: no compensation for time dependence; corrections for scalar factors; corrections for scalar factors and f_{cc} ; compensation for all known time dependence; high-latency calibration produced just after O2 (C02). Spectral lines and broadband noise were subtracted from all data sets.

Table 4 : Estimated source parameters for GW170814 for several different calibration configurations

Corrections	SNR	$\ln \mathcal{L}$	\mathcal{M} (M_\odot)	$\sigma_{\mathcal{M}}$ (M_\odot)	η	σ_η	d_L (Mpc)	σ_{dL}
None	17.4921	-7993.21	26.5579	0.7670	0.246079	0.005978	562.231	98.967
Scalars	17.6186	-7735.51	26.5976	0.8240	0.245715	0.006348	538.781	113.180
Scalars + f_{cc}	17.4422	-7987.60	26.7048	0.7124	0.245989	0.005739	561.622	112.137
All	17.4129	-7997.77	26.8131	0.8091	0.246412	0.004917	596.102	126.149
All_noclean	15.5780	-7985.56	26.9420	0.9493	0.244196	0.008258	705.301	154.781
C02_clean	17.2492	-7983.27	27.0883	0.7894	0.246523	0.004982	597.148	124.125

of coalescence (see [37]). Left unaddressed, this glitch would significantly corrupt the parameter estimation. To remove the glitch, the calibrated data was multiplied by an inverted Planck-taper window to taper the $h(t)$ data to zero for the duration of the glitch (~ 0.25 s). The duration of the taper used for the window was 0.25 s. This differs from what was done to produce the cleaned C02 data, which is included in the following plots

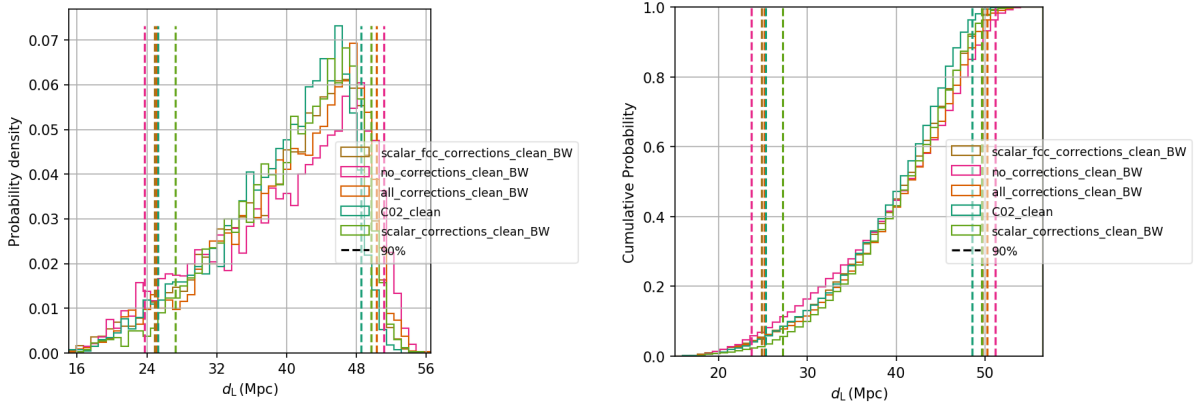


Figure 32 : Probability distributions and cumulative distributions of luminosity distance d_L for GW170817, comparing 5 versions of calibration with: no compensation for time dependence; corrections for scalar factors; corrections for scalar factors and f_{cc} ; compensation for all known time dependence; high-latency calibration produced just after O2 (C02). Spectral lines and broadband noise were subtracted from all data sets.

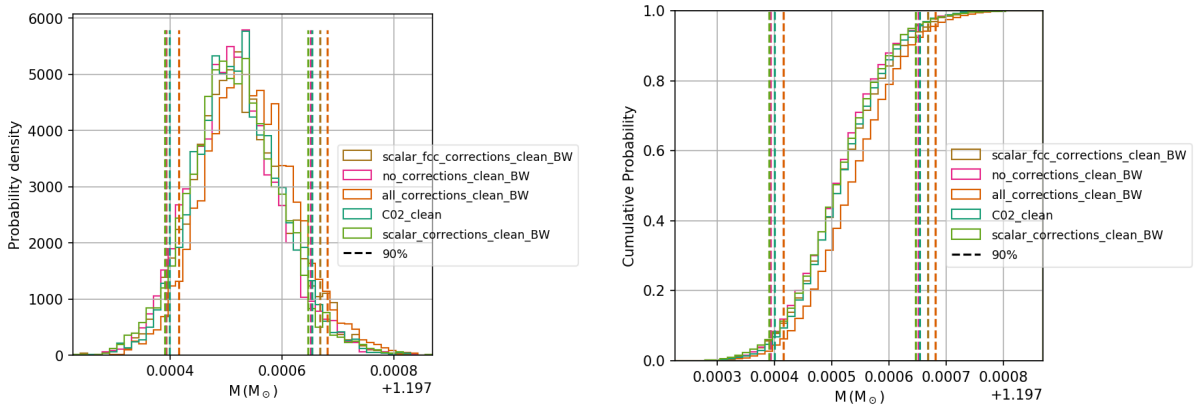


Figure 33 : Probability distributions and cumulative distributions of chirp mass \mathcal{M} for GW170817 in the detector frame, comparing 5 versions of calibration with: no compensation for time dependence; corrections for scalar factors; corrections for scalar factors and f_{cc} ; compensation for all known time dependence; high-latency calibration produced just after O2 (C02). Spectral lines and broadband noise were subtracted from all data sets.

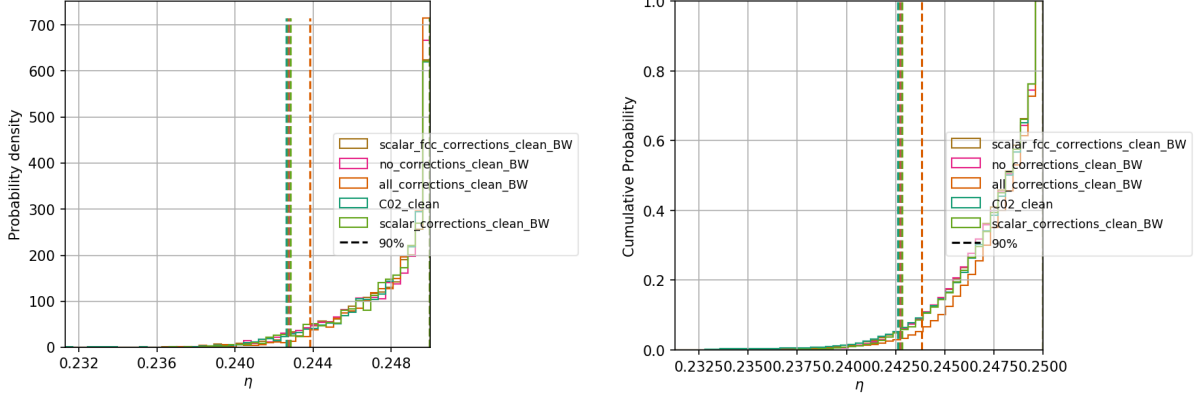


Figure 34 : Probability distributions and cumulative distributions of symmetric mass ratio η for GW170817, comparing 5 versions of calibration with: no compensation for time dependence; corrections for scalar factors; corrections for scalar factors and f_{cc} ; compensation for all known time dependence; high-latency calibration produced just after O2 (C02). Spectral lines and broadband noise were subtracted from all data sets.

for comparison. The cleaned C02 data was produced by subtracting a model of the glitch based on wavelet reconstruction from the $h(t)$ data, according to the methods described in [38].

Probability distributions and cumulative distributions of the luminosity distance d_L are seen in Fig. 32, showing only small differences between calibration configurations. Fig. 33 shows probability distributions and cumulative distributions of the chirp mass \mathcal{M} of the system in the detector frame, and Fig. 34 shows similar plots for the symmetric mass ratio η . Fig. 35 shows the 90% confidence region in m_1 - m_2 parameter space in the detector frame. Results are shown for average values of matched filter SNR and the log-likelihood $\ln \mathcal{L}$, and average values and standard deviations of \mathcal{M} (detector frame), η , and d_L in Table 5. Subtraction of spectral lines and broadband noise was used for all data sets except for one, labeled “All_noclean.”

In general, the impact of compensating for the time dependence of the TDCFs was relatively small for both events compared to the uncertainty in the parameters. The impact would likely become larger in signals with higher SNR, or in results that will eventually be based on large numbers of measurements from numerous observing runs, such as the neutron star equation of state [39], estimates of rates and populations [40], and measurements of the Hubble constant H_0 [41].

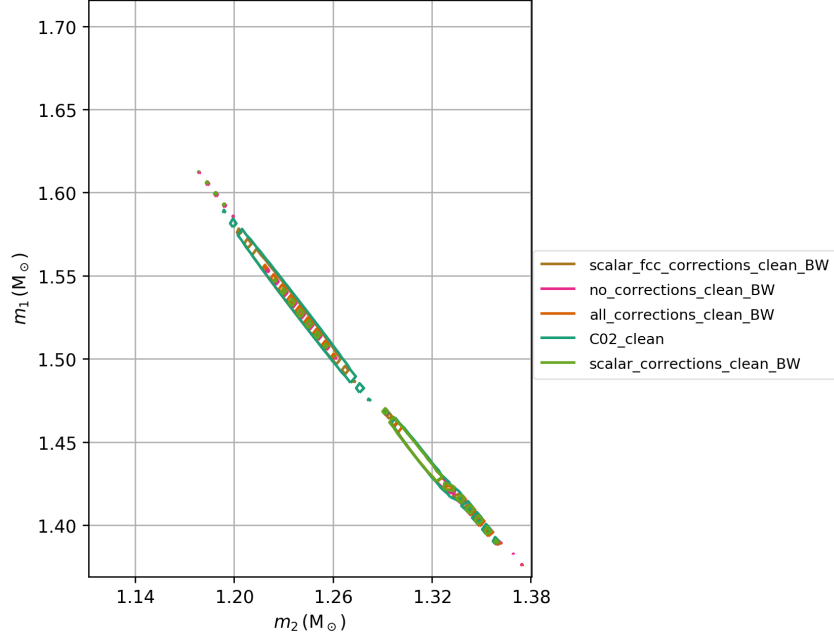


Figure 35 : 90% confidence regions in m_1 - m_2 parameter space (detector frame) for GW170817, comparing 5 versions of calibration with: no compensation for time dependence; corrections for scalar factors; corrections for scalar factors and f_{cc} ; compensation for all known time dependence; high-latency calibration produced just after O2 (C02). Spectral lines and broadband noise were subtracted from all data sets.

Table 5 : Estimated source parameters for GW170817 for several different calibration configurations

Corrections	SNR	$\ln \mathcal{L}$	\mathcal{M} (M_\odot)	$\sigma_{\mathcal{M}}$ (M_\odot)	η	σ_η	d_L (Mpc)	σ_{dL}
None	32.0659	-435150	1.19752	0.00008	0.247647	0.002387	40.1608	8.5824
Scalars	31.9267	-435096	1.19752	0.00008	0.247676	0.002343	40.5240	7.0810
Scalars + f_{cc}	31.8898	-435183	1.19752	0.00008	0.247594	0.002445	39.9722	7.7153
All	31.5160	-434784	1.19754	0.00008	0.247977	0.002161	40.5781	7.73101
All_noclean	29.7538	-436495	1.19757	0.00009	0.247963	0.002263	40.6685	6.9811
C02_clean	32.3551	-435432	1.19752	0.00008	0.247626	0.002558	39.5273	7.2086

7.3 Noise subtraction and parameter estimation

The impact of the subtraction of spectral lines and broadband noise is quite significant in the results of this study. Fig. 36 shows the impact of the noise subtraction on the skymap computed for GW170814. A systematic shift in position is clearly visible, and the the 1- σ confidence region is reduced in size from 462 square degrees to 310 square degrees. The

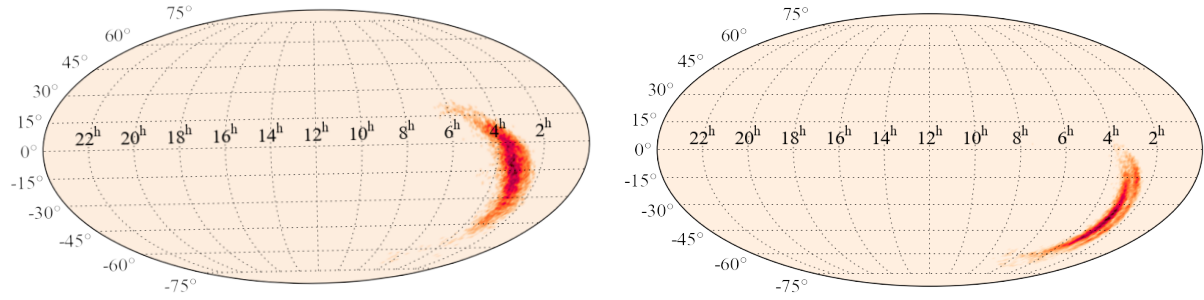


Figure 36 : Skymaps produced by LAL parameter estimation software showing the estimated location of the binary black hole merger GW170814, with and without subtraction of spectral lines and broadband noise. The cleaned data is on the right. Due to noise subtraction, the $1-\sigma$ confidence region is reduced in size from 462 square degrees to 310 square degrees. All known time dependence was compensated for in both plots.

strain data used for this comparison was compensated for all known time dependence. A comparison of the same two data sets is also shown in Table 4. The rows labeled “All” and “All_noclean” are the cleaned and uncleaned data, respectively. The results show an 11% increase in matched filter SNR due to the noise subtraction. Additionally, the $1-\sigma$ uncertainties of all parameters in the data set are significantly reduced. Most surprising is the systematic change in luminosity distance d_L due to noise subtraction. The majority of this impact comes from the removal of broadband noise caused by laser beam jitter in the H1 detector. A similar comparison is shown for GW170817 in Table 5, where the SNR increases by 6% due to noise subtraction.

Chapter 8

Conclusion

Since the beginning of O2, significant improvements have been made to the low- and high-latency calibration procedures in the `gstlal` calibration pipeline. These include improvements in calibration accuracy, reduction in intrinsic calibration latency, and the inclusion of a method to subtract spectral lines and independently-measurable broadband noise from the $h(t)$ spectrum.

A significant reduction in systematic error in the calibrated strain data was accomplished through the development of a calibration procedure that compensates for all parameterized time dependence in the calibration model. Previously, it was only possible to apply scalar magnitude corrections to the calibrated components of ΔL_{free} . A method has now been developed and implemented in the `gstlal` calibration pipeline that allows periodic updates to FIR filters, using a generic filter model with an arbitrary number of time-varying zeros and poles, a variable gain, and a variable time delay. Analysis of O2 data indicates that this method can reduce systematic errors in the calibrated $h(t)$ data to the level of $\sim 1\%$ in magnitude and $\sim 1^\circ$ in phase from 20 Hz to 1 kHz. This is a significant improvement over the systematic errors in $h(t)$ of up to 5% in magnitude and 3° in phase reported during O2. Additionally, the flexibility of this generic filter model makes it adaptable to many different time-dependent models that could be discovered in future observing runs.

A new analytical solution useful for computing the TDCFs is also presented, which

does not rely on the approximations employed by the method currently used. This is not implemented in the `gstlal` calibration yet, simply because it is a very recent development. This new solution has two main advantages. The primary motivating factor in finding this solution is to remove unwanted covariance in the computed values of the TDFCs and thus remove the systematic errors induced by the breakdown of the approximations currently used, occurring at times when the true response function deviates significantly from that of the static reference model. A second benefit is increased flexibility of the placement of calibration lines. The approximations used in the currently-implemented method require that 4 of the calibration lines be placed in a narrow frequency band, within ~ 1 Hz of one another. Under this newly-developed method, calibration accuracy will be optimized simply by choosing calibration line frequencies in bands where each TDFC is expected to have a significant impact.

Although the current impact of systematic errors at the level of 5% on most astrophysical analyses is fairly small, it is anticipated that as detector sensitivity increases and large numbers of detections of binary black hole mergers, binary neutron star mergers, and other exotic astrophysical systems are made, calibration accuracy will become increasingly important, especially for estimation of populations and rates [40], the neutron star equation of state [39], and the Hubble constant [41].

A significant reduction in calibration latency was also achieved due to this work. Since the beginning of O2, latency intrinsic to the `gstlal` calibration pipeline has been reduced from ~ 12 s to its current value of ~ 3 s. Although calibration latency is currently only a small contributor to the total latency between acquiring a GW signal and sending automated alerts to astronomers, a coordinated effort to reduce latency from other sources during O3 will make calibration latency a significant limiting factor. Early-warning searches for events like the binary neutron star merger GW170817 will benefit greatly from the reduction of total latency to a few seconds, as the temporal separation of such mergers and the resulting gamma-ray bursts is now known to occur on this timescale [37]. Further improvements to calibration latency are necessary for this purpose, with the goal of achieving intrinsic calibration pipeline latency of ~ 1 s.

A recent improvement related to calibration latency is the improvement in the high-pass filtering of $h(t)$ data, accomplished primarily through the use a better window function in the production of the FIR filters. This is expected to benefit downstream data analysis as well.

Finally, a new feature has been developed in the `gst1a1` calibration pipeline that allows for the subtraction of spectral lines including calibration lines and power mains lines, as well as broadband noise with correlated noise in any witness sensors that are insensitive to GWs. This is accomplished through the calculation and periodic revision of optimized transfer functions and FIR filters used to produce estimates of excess noise in $h(t)$ to be subtracted from the signal. Offline noise subtraction done following O2 increased detectable volume in H1 calibrated data by about a factor of 2. Results from the line and noise subtraction implemented in the `gst1a1` calibration pipeline using the same data show a similar improvement, with an associated increase in signal-to-noise ratio and significant improvement in the estimation of source parameters in compact binary sources of GWs. Results show that this method is stable over time and has no detrimental impact on calibration accuracy. Moreover, the inclusion of noise subtraction in the calibration procedure can make this data product available in low latency for the first time, and is seen to have a negligible impact on calibration latency.

Bibliography

- [1] LIGO Scientific Collaboration and Virgo Collaboration, B. P. Abbott *et al.*, arXiv:1811.12907 (2018).
- [2] C. Cahillane *et al.*, Phys. Rev. D **96**, 102001 (2017).
- [3] D. Davis *et al.*, Class. Quant. Grav. **36**, 055011 (2019), 1809.05348.
- [4] I. Newton, *Philosophiæ naturalis principia mathematica*, 1687.
- [5] A. Einstein, Annalen der Physik **322**, 891 (1905),
<https://onlinelibrary.wiley.com/doi/pdf/10.1002/andp.19053221004>.
- [6] A. Einstein, Sitzungsberichte der Königlich Preußischen Akademie der Wissenschaften (Berlin), Seite 844-847. (1915).
- [7] J. D. E. Creighton and W. G. Anderson, *Gravitational-wave physics and astronomy* (Wiley-VCH Verlag GmbH & Co. KGaA, 2011).
- [8] J. B. Hartle, *Gravity: an introduction to Einstein's general relativity* (Addison-Wesley, 2003).
- [9] R. M. Wald, *General relativity* (University of Chicago Press, 1984).
- [10] A. Einstein, Sitzungsber. Preuss. Akad. Wiss. Berlin (Math. Phys.) **1916**, 688 (1916).
- [11] LIGO Scientific Collaboration and Virgo Collaboration, B. P. Abbott *et al.*, Phys. Rev. Lett. **116**, 061102 (2016).
- [12] J. M. Weisberg, J. H. Taylor, and L. A. Fowler, Scientific American **245**, 74 (1981).

- [13] J. T. Whelan, Visualization of Antenna Pattern Factors via Projected Detector Tensors.
- [14] A. Buonanno and Y.-b. Chen, Phys. Rev. **D64**, 042006 (2001), gr-qc/0102012.
- [15] X. Siemens *et al.*, Class. Quant. Grav. **21**, S1723 (2004).
- [16] A. D. Viets *et al.*, Class. Quant. Grav. **35**, 095015 (2018).
- [17] M. Wade *et al.*, Improving ligo calibration accuracy using adaptive filtering techniques, <https://dcc.ligo.org/LIGO-P1800313>.
- [18] S. Karki *et al.*, Rev. Sci. Instrum. **87**, 114503 (2016).
- [19] A. Sottile, Characterization of the photon calibrator data from ligo's sixth science run, <https://dcc.ligo.org/LIGO-P1100013/public>.
- [20] LIGO Scientific Collaboration, B. P. Abbott *et al.*, Phys. Rev. D **95**, 062003 (2017).
- [21] D. Tuyenbayev *et al.*, Classical Quant. Grav. **34**, 015002 (2016).
- [22] GStreamer, <https://gstreamer.freedesktop.org>.
- [23] GNU, <https://www.gnu.org/>.
- [24] GObject, <https://developer.gnome.org/gobject/stable/>.
- [25] GLib, <https://developer.gnome.org/glib/stable/glib.html>.
- [26] gstlal-calibration,
<https://git.ligo.org/lscsoft/gstlal/tree/gstlal-calibration-1.2.9-v1/gstlal-calibration>.
- [27] gstlal, <https://wiki.ligo.org/DASWG/GstLAL>.
- [28] LAL, <https://wiki.ligo.org/DASWG/LALSuite>.
- [29] J. Graef Rollins, arXiv preprint arXiv:1604.01456 (2016).
- [30] LIGO data grid, <https://www.lsc-group.phys.uwm.edu/lscdatagrid/>.

- [31] E. Oelker, L. Barsotti, S. Dwyer, D. Sigg, and N. Mavalvala, *Opt. Express* **22**, 21106 (2014).
- [32] J. S. Bendat and A. G. Piersol, *Random data: analysis and measurement procedures* Vol. 729 (John Wiley & Sons, 2011).
- [33] L. Tsukada *et al.*, *Phys. Rev. D* **97**, 103009 (2018).
- [34] B. Allen, W. Hua, and A. C. Ottewill, (1999), gr-qc/9909083.
- [35] LIGO Scientific, J. C. Driggers *et al.*, *Phys. Rev.* **D99**, 042001 (2019), 1806.00532.
- [36] **GWpy**, <https://gwpy.github.io/docs/stable/>.
- [37] LIGO Scientific Collaboration and Virgo Collaboration, B. P. Abbott *et al.*, *Phys. Rev. Lett.* **119**, 161101 (2017).
- [38] N. J. Cornish and T. B. Littenberg, *Classical and Quantum Gravity* **32**, 135012 (2015).
- [39] M. F. Carney, L. E. Wade, and B. S. Irwin, *Phys. Rev.* **D98**, 063004 (2018), 1805.11217.
- [40] S. M. Gaebel, J. Veitch, T. Dent, and W. M. Farr, *MNRAS* **484**, 4008 (2019), 1809.03815.
- [41] DES, LIGO Scientific, Virgo, M. Soares-Santos *et al.*, Submitted to: *Astrophys. J.* (2019), 1901.01540.

CURRICULUM VITAE

Aaron D. Viets

Place of birth: Excelsior Springs, MO

EDUCATION

- 8/2014–5/2019 **Doctor of Philosophy in Physics**
University of Wisconsin – Milwaukee, Milwaukee, WI
Advisor: Dr. Jolien Creighton
- 8/2008–5/2012 **Bachelor of Science in Physics**
Missouri University of Science and Technology, Rolla, MO

RESEARCH EXPERIENCE

- 9/2015 - Present Member of Laser Interferometer Gravitational-wave Observatory (LIGO)
Time-domain calibration in Advanced LIGO
Using post-Newtonian waveform models to probe the mass gap
- 6/2015–7/2017 **Graduate Research Assistant**
University of Wisconsin – Milwaukee, Milwaukee, WI
Advisor: Dr. Jolien Creighton
- 8/2013–12/2013 **Graduate Research Assistant**
Missouri University of Science and Technology, Rolla, MO
Advisor: Dr. Alexey Yamilov
Studied light propagation through random correlated structures

TEACHING EXPERIENCE

- 8/2017–Present **Assistant Professor of Physics**
Concordia University Wisconsin, Mequon, WI
Teaching introductory physics lectures and labs
- 8/2014–5/2015 **Graduate Teaching Assistant**
University of Wisconsin – Milwaukee, Milwaukee, WI
Discussion section leader for introductory physics courses
Lab instructor for introductory astronomy courses
- 1/2014–5/2014 **Graduate Teaching Assistant**
Missouri University of Science and Technology, Rolla, MO
Recitation instructor for Physics for Engineers

FELLOWSHIPS AND AWARDS

- 2018-2020 NSF Sub-award: Scalable CyberInfrastructure for
Early Warning Gravitational-wave Detections
- 2018 Summer Research Award UW – Milwaukee
- 2017 David Lichtman Research Fellowship UW – Milwaukee
- 2016 Summer Research Award UW – Milwaukee
- 2015 Summer Research Award UW – Milwaukee
- 2014/2015 Chancellor's Graduate Student Award UW – Milwaukee
- 2013/2014 Chancellor's Fellowship Missouri S&T
- 2012/2013 Chancellor's Fellowship Missouri S&T

CONFERENCES AND PRESENTATIONS

Faculty Scholarship Summit, November 2017

Concordia University Wisconsin, Mequon, WI

“Calibrating History’s First Detected Gravitational Waves”

CGCA Seminar, October 2017

University of Wisconsin – Milwaukee, Milwaukee, WI

“Calibrating Advanced LIGO Data: Methods and Development”

LIGO-Virgo Spring Meeting, March 2017

Pasadena, CA

“Probing the Mass Gap Using pN Corrections to CBC Waveform Amplitudes”

LIGO-Virgo Meeting, March 2016

Pasadena, CA

PUBLICATIONS

A. D. Viets *et al.*, “Reconstructing the calibrated strain signal in the Advanced LIGO detectors.” *Classical and Quantum Gravity* **35**, 095015 (2018)

Barbara Hale, Gerald Wilemski and **Aaron Viets**. “Monte Carlo Simulations of Growth/Decay Rate Constant Ratios for Small Methanol Clusters: Application to Nucleation Data Analysis.” *AIP Conference Proceedings* **1527**, 27 (2013)

M. Wade, **A. D. Viets**, T. Chmiel, M. Stover. “Improving LIGO calibration accuracy using adaptive filtering techniques.” (in prep.)